RMIT UNIVERSITY

Synthesis, structural transformation and surface properties of two dimensional metal oxides and their compounds

A thesis submitted in fulfilment of the requirements for the degree of Doctor of Philosophy

Robi Shankar Datta

Bachelor of Electrical and Electronic Engineering (with Honours), BRAC University, Bangladesh

Master of Engineering Science (Research), University of Malaya, Malaysia

School of Engineering

College of Science, Engineering and Health

RMIT University

July, 2019

Abstract of Thesis

This PhD project explores the synthesis and fundamental properties of two dimensional (2D) metal oxides, and investigates their feasibilities in applications such as catalysis and electronics. The field of 2D materials research is mostly focused on layered crystals, out of which ultra-thin planes (few monolayers) can be readily extracted. The high surface area of 2D nanosheets allows for efficient interaction with the molecular entities in the vicinity of the oxide, which can be bound to or electrostatically adsorb onto the basal surface. In the first part of this PhD, layered α-MoO$_3$ is exfoliated into 2D nanosheets forming defect-rich 2D α-MoO$_{3-x}$. The synthesized compound is found to display superior activity for the electrocatalytic hydrogen evolution reaction (HER) with a low overpotential and fast electron transfer for hydrogen production. The combination of oxygen deficient structure and large surface area of the 2D nanosheets with structural defects and steps played as key factors to achieve high HER activity.

Thus far, the field of 2D materials research is predominantly focused on naturally stratified or layered materials due to the ease of their exfoliation. However, there are many important types of metal oxide compounds, which do not occur in the form of natural layered crystals, and hence cannot be readily transformed into 2D nanosheets. If these crystals are synthesized in 2D morphologies, they can offer the

required large surface-area for various catalytic reactions. In the second part of this PhD, a two-step synthesis approach is explored to synthesize 2D nanosheets of non-layered crystals. First, layered α-MoO$_3$ is exfoliated into 2D α-MoO$_{3-x}$. Subsequently, these defect rich 2D α-MoO$_{3-x}$ nanosheets are transformed into stable 2D PbMoO$_4$ nanosheets using a solution phase topotactic reaction. The transformed 2D PbMoO$_4$ nanosheets display trap states within their bandgap, enabling their efficient performance as a photocatalyst under visible light irradiation. The transformed 2D nanosheets act as an excellent photocatalyst to degrade the organic pollutants in water. The presented method in this work can be likely extended to establish a variety of highly stable defect rich 2D metal molybdates for potential applications in visible light based photocatalysis, which are otherwise challenging to synthesize.

Finally, synthesis of a non-layered transparent conductive oxide (TCOs) as 2D nanosheets is also explored using a liquid metal reaction approach. This highly scalable technique produces ultra-large 2D indium tin oxide (ITO) nanosheets, which can potentially be utilized in the future industrial production of TCOs. ITO is a widely used transparent conductor which finds application in every-day electronics such as touch screens and flat panel displays. One key limitation of ITO is the brittle nature of this ceramic, prohibiting its use in flexible electronics. Additionally, the commercial deposition of this material mostly relies on vacuum based techniques. Herein, the wafer scale printing synthesis of highly flexible 2D ITO nanosheets with a typical thickness of 1 nm is presented. A low temperature liquid metal printing approach is utilized to directly deposit 2D ITO onto a variety of substrates including polymers. The final nanosheets feature two orders of magnitude lower light absorption when compared with graphene, while maintaining suitable electrical

conductance for device fabrication. The developed technique will enable low cost, printable and flexible optoelectronics, while also providing an alternative to graphene with superior transparency for the creation of van der Waals heterostructures.

Declaration

I certify that except where due acknowledgement has been made, the work is that of the author alone; the work has not been submitted previously, in whole or in part, to qualify for any other academic award; the content of the thesis is the result of work which has been carried out since the official commencement date of the approved research program; any editorial work, paid or unpaid, carried out by a third party is acknowledged; and, ethics procedures and guidelines have been followed.

Robi Shankar Datta

July, 2019

Acknowledgements

First and foremost, I would like to thank the almighty to be the most gracious and merciful all through my life. I would like to convey my heartiest appreciation and sincere thanks to my honorable supervisors Dr. Torben Daeneke, Dr. Dorna Esrafilzadeh and Professor Kourosh Kalantar-zadeh for providing me with the opportunity to undertake this exciting work. Thank you for your invaluable initiatives and inputs to my work. Specially, my principle supervisor Dr Torben Daenek has been the real driving force throughout my PhD. I have been blessed to have your unconditional support and motivation to complete this thesis. My sincere thanks to Dr. JianZhen Ou for his expert advices during this journey.

This PhD thesis would not have been possible without the support of all the great people involved in my research. I would like to thank the RMIT University for the RMIT Research Stipend Scholarship and school of engineering at RMIT University for the top up scholarship award.

Many appreciations to the research facilities at RMIT University including the MicroNano Research Facilitiy (MNRF), the RMIT microscopy and Microanalysis Facilities (RMMF) and RMIT chemistry laboratories. My sincere thanks to the technical staffs Dr. Zeyad Nasa, Dr. Chenglong Xu, and Dr. Edwin Mayes. I would like to thank several of my fellow colleagues from centre for advance electronics and sensors (CADES) at RMIT University for their contribution to my work. You have made my PhD journey more productive and joyful, Nitu Syed, Md Mohiuddin, Ali Zavabeti, Farjana Haque, Nripen Dhar, Bao Yue Zhang, Azmira Jannat, Hareem Khan, and Kibret Messalea.

I would also like to express my deepest love and affection to my father Laxman Chandra Datta and my mother Anuva Datta and my lovely wife Dipa Roy for their unconditional love and support regardless of any situation. I would also like to thank my younger brother Sham Shankar Datta for taking care of my family while I am away from home. Lastly, I would also like to thank my school friends Ashik, Ovik and Asif who I badly missed throughout this journey. This is the only phase of my educational career, which I passed without having them around me.

Table of contents

List of Figures

the sample work up procedures described within the Methods section. (c) HRTEM image of the optimized 2D ITO nanosheet. The colour code highlights the crystal orientation based on the fast Fourier transform (FFT) image shown in the lower right inset. The upper left inset shows a magnified view of the lattice pattern and the upper right image shows a dark field image of the region of interest. (d) HRTEM image for an exfoliated 2D sheet containing excessive Sn, showing an amorphous structure with occasional crystalline sections. The upper right inset shows a dark field image of the region of interest, while the lower right inset shows the FFT image.

List of Tables

Abbreviations

2D	Two-dimensional
AFM	Atomic force microscopy
BET	Brunauer Emmett Teller
CVD	Chemical vapor deposition
DI	Distilled water
EDLC	Electrical double layer capacitor
EELS	Electron energy loss spectroscopy
HRTEM	High resolution transmission electron microscopy
ICP-MS	Inductively coupled plasma mass spectrometer
ITO	Indium tin oxide
PESA	Photoemission spectroscopy in air
PVD	Physical vapor deposition
RHE	Reversible hydrogen electrode
SAED	Selected area electron diffraction
STEM	Scanning transmission electron microscopy
TCO	Transparent conductive oxide
TEM	Transmission electron microscopy
TMO	Transition metal oxide
TGA	Thermal gravimetric analysis
UV-Vis	Ultraviolet visible
XPS	X-ray photoelectron spectroscopy
XRD	X-ray diffraction

Chapter 1

Introduction

1.1. Motivation

Inspired by the successful isolation of atomically thin layers of carbon (known as graphene) in 2004 by Geim and Novoselov, remarkable attention and efforts have been dedicated into the field of two dimensional (2D) materials research.[1] Materials with layered or stratified crystal structures are considered to be ideal to synthesize 2D nanosheets and therefore, special attention has been paid to the layered transitional metal oxides (TMOs) and transition metal chalcogenides due to their natural abundance and unique properties.[2]

2D semiconducting and conducting materials are an emerging class of compounds characterized by their ability to form stable nanosheets with the thickness of a few monolayers and lateral dimensions spanning several micrometres. Due to the high surface area to volume ratios and nanometer thin morphology, these nanosheets feature ample opportunities to tune their surface chemistry and acquire the abilities to display numerous interesting properties which cannot be realized in their bulk counterparts. In particular, quantum confinements across the planar boundaries of these 2D crystals leads to fascinating electronic and optical properties.[2] Such 2D morphologies, with the appearance of corners, steps and edges, are also ideal for applications that require highly active surfaces and therefore have been vastly utilized for catalysis.[3]

Layered materials of van der Waals nature are the traditional source for synthesizing 2D metal oxides due to their weakly attached layers which may be exfoliated with ease. A number of transition metal oxides (TMOs) display layered crystal features. A range of methods have been adopted to exfoliate such layered TMOs, however, liquid phase exfoliation techniques are the most widely explored methods for high throughput applications.[4] For example, layered crystal arrangement of orthorhombic molybdenum oxides (α-MoO_3) facilitates its exfoliation into 2D nanosheets, which in turn provides access to tune its surface properties, making this metal oxide compound suitable for various catalytic applications.[4] Molybdenum oxides can be found in various stoichiometries, ranging from full stoichiometric MoO_3, which features a wide bandgap (~3.2 eV),[5-7] to more conducting reduced oxides in the form of MoO_{3-x} ($2 < x < 3$) and eventually semi-metallic MoO_2 with a significantly reduced bandgap (~0.24 eV).[8-10] Upon inducing oxygen defects, Mo^{6+} ions can be reduced to Mo^{5+} and finally Mo^{4+} (MoO_2). Through this process, the oxide's optical appearance changes as a function of the degree of reduction due to generated gap states and its color transitions from transparent to yellow and eventually greyish/blue.[11, 12] These properties have provided the motivation to use these oxides in advanced optical and electrocatalytic systems. However, the electrocatalytic activities of full stoichiometric molybdenum oxides is limited by their poor reaction kinetics and thus require further tuning in their stoichiometries. Investigating the electrocatalytic properties of sub-stoichiometric molybdenum oxides in 2D form may overcome this limitation and this PhD research aims to explore this particular research gap.

1) The stoichiometric tuning of molybdenum oxides has been demonstrated and was explored for electronic and optical applications.[11, 12] However, the potential of reduced molybdenum oxides as an efficient electrocatalyst has not been investigated to date. Additionally, the utilization of 2D morphologies in electrochemical reactions

may hold additional promise due to the increased surface area and high surface activity that is associated with 2D structuring. As such, it is hypothesized that the combination of both oxygen deficient structure and 2D morphology can significantly activate the electrocatalytic hydrogen evolution reaction (HER) performance of molybdenum oxides to electrochemically produce H_2 gas.

Thus far, the field of 2D research is predominantly focused on stratified materials due to the ease of their exfoliation. However, there are many types of metal oxide compounds, which do not occur in the form of natural layered or stratified crystals, and hence cannot be readily formed into 2D nanosheets using conventional methods. For example, metal molybdates, with relatively large bivalent cations (Ba, Pb, Sr and Ca with ionic radius >0.99 Å) are non-layered crystals, which are typically found in scheelite-type structures of body centred tetragonal orientation.[13] These materials have presented promising performance in various catalytic applications. Different liquid and gas/vacuum phase synthesis methods have been used for establishing low dimensional metal molybdates such as $PbMoO_4$ crystals.[14, 15] However, none of these methods favour the growth of nanosheets with 2D morphologies, since $PbMoO_4$ is not a naturally stratified crystal. Therefore, many unique properties of this material are still undiscovered, leading to the following research gap:

2) Metal molybdates such as $PbMoO_4$ have been widely investigated in photocatalytic reactions due to their favourable band positions and photostability.[13, 16] However, the morphologies that have been employed to date are predominantly based on bulk materials and nanoparticles, which do not provide the large surface area associated with 2D materials. Additionally, the wide bandgap of $PbMoO_4$ has also restricted its photocatalytic application to the ultraviolet spectrum spectrum.[13] It would be interesting to design new synthesis methods that can produce 2D nanosheets of the conventionally 3D material $PbMoO_4$. If these crystals are synthesized with 2D

morphologies, they can offer the required large surface-area for various catalytic reactions. Topotactic reactions using 2D layered materials as precursors can potentially provide a route to synthesis 2D nanosheets of materials that feature non-stratified 3D bulk crystal structures. The introduction of defect states in 2D sheets may also facilitate operation within the visible spectrum.

Despite the extraordinary scientific importance of the 2D metal oxides, the large area synthesis of these materials is still a challenge. However, a very recent report by Zavabeti *et al.*[3] has demonstrated a highly scalable technique to produce ultra-large area 2D metal oxide nanosheets using liquid metal reaction media. This process shows that interfacial oxide layers grown on liquid metals or alloys can be isolated and transferred as 2D layers using a van der Waals transfer method onto desired substrates. By using this method, atomically thin nanosheets spanning several centimetres in lateral dimensions can be achieved. Interestingly, this method successfully produced large 2D nanosheets of a range of non-layered crystals, opening the door for many of the non-layered metal oxide compounds such as transparent conductive oxides (TCOs) to be obtained in 2D morphology.

3) TCOs are extensively used as transparent electrodes in commercial applications including displays and light emitting devices. The challenges that are associated with the existing methods for TCO production are high process costs and the lack of mechanical flexibility of the final deposited layers. The liquid metal synthesis method discussed above may enable the synthesis of 2D TCO sheets at wafer scales, which may overcome the issues associated with the low material flexibility and high process costs associated with these materials. A part of this PhD work aims to explore this hypothesis.

1.2. Objectives

1.2.1. Investigating two dimensional α-MoO$_{3-x}$ for electrocatalytic hydrogen evolution reaction

In the global endeavour to develop clean energy sources, the advancement of earth-abundant electrocatalysts for hydrogen evolution, with high activity and stability, has been of great interest for the past few decades.[17-19] The highly adaptive features of molybdenum oxides in terms of tuning their chemical and physical properties make them versatile for their incorporations in electrochemical and catalytic systems. This earth abundant material, due to its layered crystal arrangement in the orthorhombic α-MoO$_3$ phase, is suitable to be exfoliated into 2D nanosheets, resulting in large surface areas. Variations in the oxidation states of molybdenum allow for crystal structure, morphology and oxygen vacancy tuning, making these metal oxides an intriguing target for electrochemical applications.[4]

In the first study of this PhD research, the author will synthesise oxygen deficient 2D molybdenum oxide, using a liquid phase exfoliation method. Here, the 2D morphology, structural defects and oxygen vacancies in the planar construction of molybdenum oxide nanosheets are expected to increase the active sites of the catalyst, which may act as key factors to promote the HER performance. The author will perform a thorough investigation to evaluate the suitability of the synthesized sheet as HER electrocatalyst.

1.2.2. Synthesizing 2D nanosheets of naturally non-stratified PbMoO$_4$ and investigating its photocatalytic performance

Metal molybdates, such as lead molybdate (PbMoO$_4$), are wide bandgap materials that exhibit favourable photophysical and photocatalytic properties due to their stable crystal

structures, their band positions that provide sufficient driving force for chemical conversions, good light absorption properties and stable redox behaviours.[13] If these crystals are synthesized in 2D morphologies, they can offer the needed large surface-area for photo-reactions. However, this category of materials does not occur naturally as stratified crystals, and hence cannot be readily formed into 2D sheets using conventional methods.

In this PhD research, the author will engineer a synthetic route for creating the sought after 2D crystals of metal molybdates. In this regard, two phenomena can be exploited: (1) Pb containing salts in aqueous solutions are known to react with molybdenum oxides to produce $PbMoO_4$ crystals *via* a facile room-temperature reaction, and also (2) the facile exfoliation of layered α-MoO_3 into 2D nanosheets. By combining these two phenomena, it is hypothesized that if the exfoliated α-MoO_3 2D sheets can be exposed to the Pb containing solutions it can eventually form the 2D sheets of $PbMoO_4$ crystals. When using defect rich 2D molybdenum oxide sheets to form 2D $PbMoO_4$, it is also expected that the resultant 2D $PbMoO_4$ sheets may also be rich in trap states. This can reduce the effective bandgap of $PbMoO_4$ leading to enhanced catalytic activity under simulated sun light. Therefore, the author aims to investigate the photocatalytic dye degradation performance of the synthesized 2D $PbMoO_4$ nanosheets and investigate the electronic structure of the material in order to shed light on the origin of the observed photocatalytic activity.

1.2.3. *Printing large area two-dimensional indium tin oxide using liquid metal reaction environment*

Indium-tin oxide (ITO) is one of the most widely applied transparent conductive oxides and is of tremendous industrial importance due to its usage in every-day electronics such as touch screens and flat panel displays.[20] However, the brittle nature of this ceramic limits its use in

flexible electronics.[21] Additionally, the deposition of this material at commercial scale mostly relies on vacuum based techniques. The typical film thickness of the deposited ITO is in the range of 50 to 500 nm, which cannot subdue its brittle nature and also deteriorates its transparency.[20, 22-25]

In the final segment of this PhD research, the author aims to explore a scalable and low temperature printable synthesis method that allows creating ultrathin 2D ITO nanosheets with a thickness of only a few atoms at wafer scales. Post transition metals with low melting point such as Ga, In and Sn create self-limiting nanometre thin surface oxides due to Cabrera-Mott oxidation in air.[26] In the liquid state, adhesion of the surface oxide to the parent metal is relatively weak, and therefore, van der Waals transfer techniques can be applied to deposit the grown 2D oxide sheet onto desired substrates.[3, 13, 26, 27] This PhD aims to explore this method to synthesize 2D ITO sheets. The proposed method will explore the utilization of low melting indium-tin alloys that can be applied in a liquid metal printing process, depositing 2D ITO on wafer scales. Reducing the thickness of a ceramic material to only a few atoms is known to substantially increase the material's flexibility,[28] allowing to overcome one of the most limiting properties of ITO.

1.3. Thesis organization

This PhD thesis focuses on synthesis of atomically thin 2D metal oxides of layered and non-layered crystals and their applications in catalysis and electronics. Therefore, the main objectives of this PhD research are to (a) investigate the electrocatalytic properties of reduced 2D molybdenum oxides in hydrogen evolution reactions for hydrogen production (b) engineer the synthetic route to produce 2D metal molybdates such as 2D $PbMoO_4$ and investigate its photocatalytic properties under visible light irradiation and (c) explore the

large area synthesis of 2D ITO using the liquid metal reaction medium and investigate its morphology, structure, conductivity and transparency.

In Chapter 2, an in-depth review of recent literature in relevant areas will be presented. The aim is to highlight the areas which require fully developed concepts and present research gaps that will become the focus of this thesis.

The outcomes of the investigation for electrocatalytic properties of reduced molybdenum oxide will be demonstrated in Chapter 3. Here, 2D MoO_{3-x} nanosheets will be synthesized using the liquid phase exfoliation techniques. The surface defects of the synthesized material will be analyzed. The prospect of this material in electrocatalytic hydrogen evolution reactions will be investigated in alkaline media, where a three electrode electrochemical set-up will be employed

Chapter 4 will present the engineered synthetic route to produce 2D nanosheet of a non-layered crystal such a $PbMoO_4$. This material will be derived from the reaction between reduced 2D molybdenum oxide and Pb based salt. The electronic band structure will be elucidated from PESA, UV-Vis and XPS spectroscopies and the structural information will be obtained from the XRD, Raman and HRTEM analysis. Furthermore, the application of this transformed material will be investigated in photocatalytic degradation of organic pollutants under visible light irradiation.

In Chapter 5, the large area synthesis of 2D ITO using the liquid metal reaction environment will be explored. The employed process entails placing a small droplet of the indium-tin liquid alloy onto a desired substrate, followed by squeezing a second substrate from the top, spreading the droplet to cover the entire desired area. The conductivity, transparency, flexibility and touch screen application of the synthesized 2D sheets will be presented in this chapter.

Finally, Chapter 6 will present the overall conclusions of this PhD research and outline the possible future directions of the research.

1.4.   References

1.   Novoselov, K.S. et al. Electric Field Effect in Atomically Thin Carbon Films. *Science* **306**, 666 (2004).

2.   Balendhran, S. et al. Two-Dimensional Molybdenum Trioxide and Dichalcogenides. *Adv. Funct. Mater.* **23**, 3952-3970 (2013).

3.   Datta, R.S. et al. Highly active two dimensional α-MoO$_{3-x}$ for the electrocatalytic hydrogen evolution reaction. *J. Mater. Chem. A* **5**, 24223-24231 (2017).

4.   de Castro, I.A. et al. Molybdenum Oxides – From Fundamentals to Functionality. *Adv. Mater.* **29**, 1701619 (2017).

5.   Qu, Q., Zhang, W.-B., Huang, K. & Chen, H.-M. Electronic structure, optical properties and band edges of layered MoO$_3$: A first-principles investigation. *Comput. Mater. Sci.* **130**, 242-248 (2017).

6.   Jittiarporn, P., Sikong, L., Kooptarnond, K. & Taweepreda, W. Effects of precipitation temperature on the photochromic properties of h-MoO$_3$. *Ceram. Int.* **40**, 13487-13495 (2014).

7.   Scanlon, D.O. et al. Theoretical and Experimental Study of the Electronic Structures of MoO$_3$ and MoO$_2$. *J. Phys. Chem. C* **114**, 4636-4645 (2010).

8.   Inzani, K. et al. Electronic properties of reduced molybdenum oxides. *Phys. Chem. Chem. Phys.* **19**, 9232-9245 (2017).

9.   Dukštienė, N. & Sinkevičiūtė, D. Photoelectrochemical properties of MoO$_2$ thin films. *J Solid. State. Electr.* **17**, 1175-1184 (2013).

10.   Hu, Z., Liu, G., Chen, X., Shen, Z. & Yu, J.C. Enhancing Charge Separation in Metallic Photocatalysts: A Case Study of the Conducting Molybdenum Dioxide. *Adv. Funct. Mater.* **26**, 4445-4455 (2016).

11.   Alsaif, M.M.Y.A. et al. High-Performance Field Effect Transistors Using Electronic Inks of 2D Molybdenum Oxide Nanoflakes. *Adv. Funct. Mater.* **26**, 91-100 (2016).

12.   Greenblatt, M. Molybdenum oxide bronzes with quasi-low-dimensional properties. *Chem. Rev.* **88**, 31-53 (1988).

13.   Datta, R.S. et al. Two dimensional $PbMoO_4$: A photocatalytic material derived from a naturally non-layered crystal. *Nano Energy* **49**, 237-246 (2018).

14.   Sczancoski, J.C. et al. Morphology and Blue Photoluminescence Emission of $PbMoO_4$ Processed in Conventional Hydrothermal. *J. Phys. Chem. C* **113**, 5812-5822 (2009).

15.   Kunkel, K., Milke, E. & Binnewies, M. Formation of ternary lead-molybdenum oxides $PbMoO_4$, $PbMo_2O_7$, Pb_2MoO_5 and $PbMo_3O_{10}$ in the gas phase: A mass spectrometric and quantum chemical investigation. *Int. J. Mass Spectrom* **374**, 12-19 (2014).

16.   Hernández-Uresti, D.B., Martínez-de la Cruz, A. & Aguilar-Garib, J.A. Photocatalytic activity of $PbMoO_4$ molybdate synthesized by microwave method. *Catal. Today* **212**, 70-74 (2013).

17.   Xie, J. et al. Defect-Rich MoS_2 Ultrathin Nanosheets with Additional Active Edge Sites for Enhanced Electrocatalytic Hydrogen Evolution. *Adv. Mater.* **25**, 5807-5813 (2013).

18.   Thangasamy, P., Ilayaraja, N., Jeyakumar, D. & Sathish, M. Electrochemical cycling and beyond: unrevealed activation of MoO_3 for electrochemical hydrogen evolution reactions. *ChemComm* **53**, 2245-2248 (2017).

19.   Najafpour, M.M. et al. Transformation of $La_{0.65}Sr_{0.35}MnO_3$ in electrochemical water oxidation. *Int. J. Hydrog. Energy* **42**, 8560-8568 (2017).

20.   Zheng, Q. & Kim, J.-K. in Graphene for Transparent Conductors: Synthesis, Properties and Applications (eds. Zheng, Q. & Kim, J.-K.) 1-27 (Springer New York, New York, NY, 2015).

21.   Cairns, D.R. et al. Strain-dependent electrical resistance of tin-doped indium oxide on polymer substrates. *Appl. Phys. Lett.* **76**, 1425-1427 (2000).

22.   Ellmer, K. Past achievements and future challenges in the development of optically transparent electrodes. *Nat. Photonics* **6**, 809 (2012).

23.   Shigesato, Y., Takaki, S. & Haranou, T. Crystallinity and electrical properties of tin-doped indium oxide films deposited by DC magnetron sputtering. *Appl. Surf. Sci.* **48-49**, 269-275 (1991).

24.   Tahar, R.B.H., Ban, T., Ohya, Y. & Takahashi, Y. Tin doped indium oxide thin films: Electrical properties. *J. Appl. Phys.* **83**, 2631-2645 (1998).

25.   Wen, L., Sahu, B.B. & Han, J.G. Development and utility of a new 3-D magnetron source for high rate deposition of highly conductive ITO thin films near room temperature. *Phys. Chem. Chem. Phys.* **20**, 4818-4830 (2018).

26.   Daeneke, T. et al. Liquid metals: fundamentals and applications in chemistry. *Chem. Soc. Rev.* **47**, 4073-4111 (2018).

27.   Daeneke, T. et al. Wafer-Scale Synthesis of Semiconducting SnO Monolayers from Interfacial Oxide Layers of Metallic Liquid Tin. *ACS Nano* **11**, 10974-10983 (2017).

28.   Charalampos, A., Kaihao, Z., Matthew, R. & Sameh, T. Tailoring the mechanical properties of 2D materials and heterostructures. *2D Mater.* **5**, 032005 (2018).

Chapter 2

Literature Review

2.1. Introduction

The focus of this thesis is the exploration of two dimensional (2D) functional metal oxides. In particular, the synthesis, fundamental properties and potential in applications in fields such as catalysis and electronics will be investigated.

2D materials generally consist of one to few-atom-thick layers in one dimension, while the other two dimensions are outside of the nanometric range.[1] 2D morphology offers a high surface-to-volume ratio and facilitates the tuning of catalytic, electronic and optical properties of a material.[2] Since the discovery of graphene and other 2D materials such as layered transition metal oxides (TMOs) and chalcogenides, 2D material research has earned significant attention.[2] 2D TMOs are of particular interest due to their layered crystal structures, natural abundance and high stability in aerobic environments.[3] The unique properties of TMOs are mostly generated by the cationic species and their adaptability in altering oxidation states.[3]

Amongst the TMOs, molybdenum oxides are one of the most adaptable and functional classes of metal oxide compounds with intriguing physical and chemical properties as well as extraordinary prospects for a variety of applications.[4] In the first segment of this chapter, the

fundamental properties, synthesis and applications of molybdenum oxides and their compounds will be discussed.

Using certain simple chemical reactions, molybdenum oxides can be transformed to other metal oxide compounds that usually crystallize in non-layered crystal patterns.[5] This transformation is mainly observed in the synthesis of metal molybdates, which are highly photostable materials that find application in various photocatalytic applications.[6] The prospect will be discussed in the mid sections.

In the field of 2D metal oxide research, the synthesis of large area (i.e. wafer scale) samples is still a significant challenge.[7] A recent finding by Zavabeti *et al.* has introduced a highly scalable technique to produce ultra-large 2D metal oxide nanosheets using liquid metal reaction media.[8] This method may offer plenty of opportunities to synthesize various non-layered 2D metal oxides. One of the most commercially important classes of non-layered metal oxides are transparent conductive oxides (TCOs), which find application in modern display technologies.[9] The developed technique may enable the synthesis of 2D TCO sheets at wafer scales, which could allow overcoming issues associated with the brittle nature of these materials. These prospects will be discussed in the later sections of this chapter.

2.2.   2D TMOs

The most renowned 2D material, graphene, consists of a one-atom-thick layer, which is produced from repeating units of hexagonally bound carbon.[10] The isolation of graphene from graphite involves a simple mechanical exfoliation process, which utilizes scotch-tape to exfoliate 2D nanosheets with monolayer thickness.[10] This discovery has sparked interest into the exfoliation of layered crystals such as TMOs.[2] The strong polarizability of oxygen ions allows planar TMOs to show large, nonlinear, and non-uniform distributions of charges

within their lattices.[3] This feature helps to realize the electrostatic influence on length scales of 1–100 nm, which generate unique local surface and interfacial properties.[3] Therefore, the emergence of specific energy states near or on the surface of planar TMOs can be observed, which are absent in their bulk counterparts. **Figure** 2.1b presents a crystal structure of a layered TMO, in this case α-MoO$_3$ is shown as a model compound.

The manipulation of electronic properties in a TMO mainly depends on the variation of oxidation states of a transition metal. This can range from semi-metallic to wide-bandgap insulating properties for the same TMO layer at different stoichiometries.[4] Therefore, 2D TMOs can be obtained with a variety of bandgaps, presenting the prospect of engineering electronic and optical characteristics at almost any sought after wavelengths. Molybdenum oxide and its compounds are one of the most tunable groups of TMOs, which have been intensely investigated and are already employed in commercial applications.[4] A significant portion of this PhD research is based on this compound and therefore, a broad review of this material is presented in the sections below.

2.3.   Molybdenum oxides and their compounds

Molybdenum oxides are versatile oxide compounds with well-recognized applications in electronics,[11] catalysts,[12] sensors,[13] energy storage,[14] field emission devices,[15] lubricants,[16] superconductors,[17] thermal materials,[18] bio systems,[19] chromogenic,[20] and electrochromical systems[21]. The field of molybdenum oxide synthesis is rich and well documented. Different approaches such as vapor deposition[22-26] and liquid phase exfoliation techniques[27, 28] have been used for creating thin films of these oxides. Molybdenum oxides have been formed into a variety of structures including quantum dots,[29] nanorods and belts,[28, 30] two dimensional

sheets,[31] and nanopores[32] as well as other nano-morphologies, which are created by combining those fundamental shape-elements.[4]

Interestingly, molybdenum oxides are found in various stoichiometries, starting from wide bandgap fully stoichiometric MoO_3 to more conducting reduced oxides (MoO_{3-x}).[33-35] The generation of oxygen defects facilitates the transition from Mo^{6+} (MoO_3) ions to Mo^{4+} (MoO_2; $x = 1$).[36] Therefore, the oxide's appearance changes as a function of the degree of reduction through the generation of gap states: from transparent to yellow and eventually grayish/blue.[37, 38] There are many reports on doping and compounding of molybdenum oxides with both organic and inorganic materials to tune their structural, physical and chemical properties.[21, 39-41]

In the following sections, a comprehensive overview regarding molybdenum oxides will be presented and the text will focus on fundamentals, synthesis, manipulation and applications of these metal oxides.

2.3.1. *Fundamental properties*

The two most common crystal phases of MoO_3 are both based on the MoO_6 octahedron building block,[4] which can be assembled to form the thermodynamically stable orthorhombic α-phase or metastable monoclinic β-phase.[35, 42, 43] Both of these phases display distinct physical and chemical properties including differing refractive indices, bandgap energies, and mechanical hardness.[4] Further observed phases are the metastable high pressure phase MoO_3-II also known as ε-MoO_3 and the comparatively more stable phase of hexagonal h-MoO_3.[4, 44] Of the known MoO_3 phases, only the orthorhombic α-phase has the desired layered crystal structure, which facilitates the synthesis of 2D morphologies.[2] **Figure** 2.1 represents the crystal structures of all the phases of molybdenum oxides. Since this PhD research covers

only the orthorhombic α-phase, therefore, the important and relevant fundamental properties of this material will be presented and discussed in the following sections for brevity. A detailed review of the properties of the other MoO_3 morphologies was recently published by the author of this thesis and as such the reader is referred to reference[4] for further information.
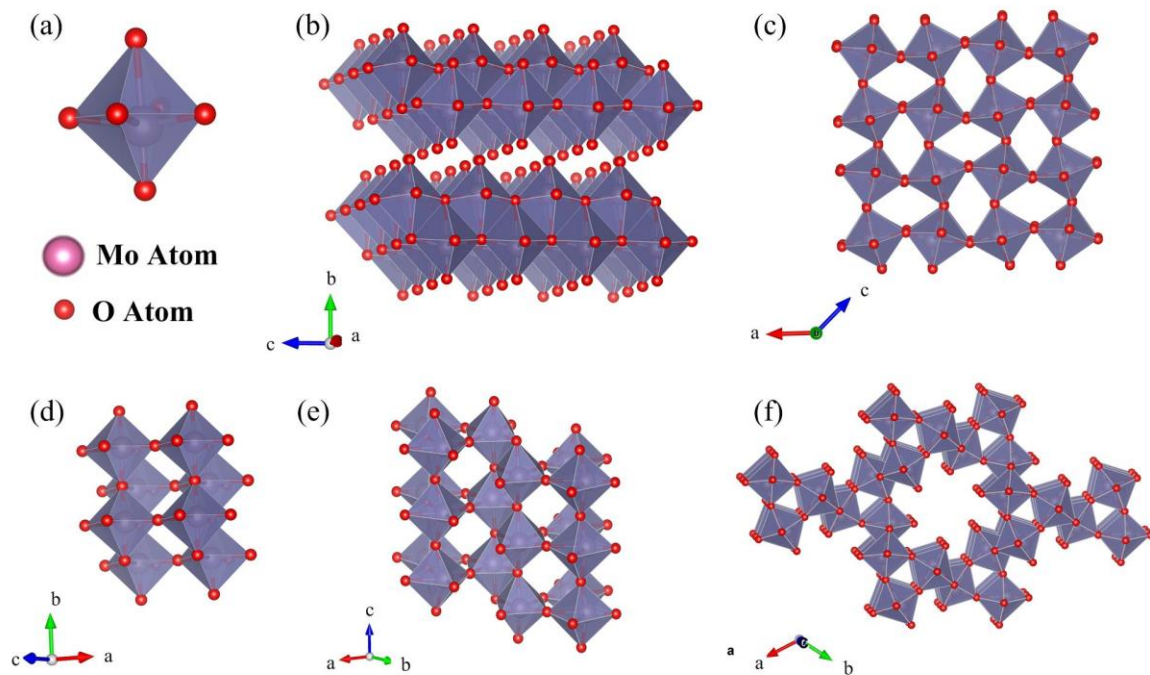
Figure 2.1. (a) MoO_6 octahedra in α-MoO_3 constitutes of molybdenum and oxygen atoms, (b) crystal structure of thermodynamically stable orthorhombic α-MoO_3 with layered orientation held together by van der Waals forces, and crystal patterns of (c) metastable monoclinic β-MoO_3, (d) ε-MoO_3, also recognized as MoO_3-II, (e) metastable h-MoO_3 and (f) tunnel structure along the c-axis of h-MoO_3 unit cell.[4]

2.3.1.1. *Crystal structures*

Orthorhombic α-MoO_3, possesses the well-known layered crystal structure of MoO_3 which offers the possibility to create 2D morphologies (see **Figure** 2.1b).[2] The layers are made of thin sheets featuring a thickness of ~0.7 nm composed of double layers of linked and distorted MoO_6 octahedra.[45] The Mo to Mo atom distance between two layers is 1.4 nm. The planar double layer sheets of distorted MoO_6 octahedra form edge-sharing zig-zag rows along the [001] direction and corner sharing rows along the [100] direction. In the vertical [010] direction, the distorted MoO_6 octahedra are held together by weak van der Waals forces resulting in stratification, while the internal interactions in the octahedra are dominated by strong covalent and ionic bonds.[35, 42, 43, 45]

The equilibrium bond distance significantly influences the properties of the Mo-O bond, where strong covalent nature is observed for the shortest bonds, a predominant ionic bond is exhibited for the longest bonds in the MoO_6 octahedron. [45] The crystal structures have three types of oxygen atoms due to their different coordination numbers (i.e. terminal (O_t), asymmetric (O_a) and symmetrically bridging (O_s)). The O_t only bonds to one Mo and the average distance is 1.67Å.[46] The O_a bonds to two Mo atoms and the bond lengths are 1.74Å and 2.25Å, respectively.[46, 47] The O_s bonds to three Mo atoms with two horizontal bonds with a distance of 1.95Å and one vertical bond with a longer length of 2.33Å (see **Figure** 2.2).[46, 47]
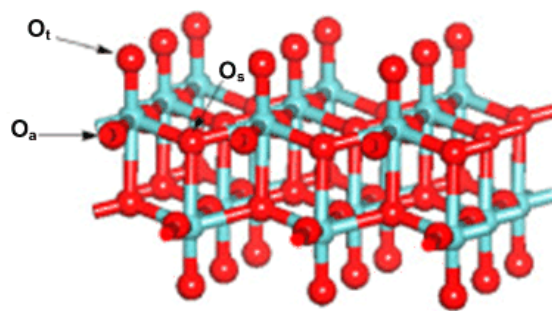
Figure 2.2. Crystal structures of α-MoO$_3$ showing the terminal (O$_t$), asymmetric (O$_a$) and symmetrically bridging (O$_s$) oxygen atoms.[46]

2.3.1.2. Electronic band structure

Stoichiometric and intrinsic MoO$_3$ in its α phase is an n-type semiconductor with an electron affinity above 6 eV and ionization energy larger than 9 eV.[33, 48] As such, it is a semiconductor with a wide bandgap of approximately 3 eV (a range from 2.7 to 3.2eV has been reported).[2] Other stoichiometric MoO$_3$ phases also feature similar bandgaps.[2, 27, 34, 49-52] The bandgap of the α-phase is indirect in nature.[53] The high work function of MoO$_3$ (generally >6.9 eV for the intrinsic semiconductor) has led to extensive applications of MoO$_3$ as anode interfacial layer in organic electronics.[33, 37, 48]

Various approaches have been proposed to manipulate the band structure of MoO$_3$ including: (i) introduction of dopants,[54, 55] (ii) creation of oxygen vacancies in the crystal structure generating donor or acceptor states[31, 37, 39, 56, 57] and (iii) structural changes such as reduction of crystal dimensions and transformation into quantum dots.[29, 58]

2.3.1.3. *Oxygen Vacancy, Doping, and Ion Intercalation*

The intrinsically wide-bandgap combined with low carrier concentrations of native MoO_3 limit its applications for electronics and optical devices that are required to operate in the visible spectrum.[4] As an approach to overcome such problems, doping allows to control and tune the carrier concentration and band structure.[31, 37, 39, 56, 57] Several reports have demonstrated the transformation of mostly ultraviolet photoactive MoO_3 into a visible or even infrared sensitive material by the introduction of oxygen vacancies or doping induced mid-gap states, allowing to attain highly efficient optoelectronic devices and photocatalysts.[59, 60]

The transition between semiconducting to semi-metallic properties can be controlled based on the fact that various amount of oxygen vacancies (i.e. Mo_4O_{11}, Mo_8O_{23}, and Mo_9O_{26}) can be obtained at high precision.[4, 31] Sub-stochiometric molybdenum oxide in the range of $0 < x \leq 0.125$ shows semiconducting properties (i.e. Mo_9O_{26} and Mo_8O_{23}), $0.125 \leq x < 1$ shows quasimetallic (i.e. Mo_4O_{11}) and $x = 1$ forms MoO_2 with a reduced bandgap of 0.24 eV (also sometimes considered semi metallic).[37, 61]

Intercalation of H^+ ions has been demonstrated to lead to the formation of H_2O groups placed within the H_xMoO_3 structure.[62] Due to the instability of the H_2O groups, molecular H_2O may be released forming oxygen vacancies and consequently transformation into MoO_{3-x} structure.[62, 63] After the intercalation and subsequent formation of MoO_{3-x}, a new defect state is formed within the bandgap.[56] The empty $4d$ band of defective molybdenum oxide has been reported to be partially occupied with electrons, giving rise to this defect band (**Figure** 2.3a, indicated as d_1) at 1.28 eV below the Fermi level (E_F).[37] A second defect band appears at 0.8 eV below the E_F at higher sub-stoichiometries (**Figure** 2.3a, indicated as d_2).[37] **Figure** 2.3b depicts the MoO_3 modification with H^+ ions intercalation, producing hydrogen bronze

structures. The electronic structure (**Figure** 2.3c) of H^+ intercalation modified MoO_3 structures present the inter bandgap states (red color) and "valence band-like Mo^{5+} states" (green color). At higher H^+ intercalation levels, more Mo bands are filled as a consequence of increased oxygen vacancy densities, which is represented in **Figure** 2.3c as a reduced width of oxygen associated electronic states (blue color).[64]

Alkali metals such as Li^+, Na^+, K^+ as well as organic compounds have also been adopted to be incorporated in the matrix of MoO_3 for lattice distortion and electronic band structure manipulation.[39, 40, 65, 66] Doping of molybdenum oxides with other metals has also been investigated leading to a general observed decreased in bandgap energy associated with increase dopant concentrations. This has been reported for Tb^+,[67] Fe^+,[68] Ag^+,[52] Eu^+,[69] Sn^+,[55] Co^+,[70] Ce^+,[71] and Er^{+}[72] dopants. The effects have been rationalized by lattice strain effects, induced defects and charge imbalance. The distortion of the MoO_3 octahedra is generally observed to increase with higher doping levels.[52, 53]
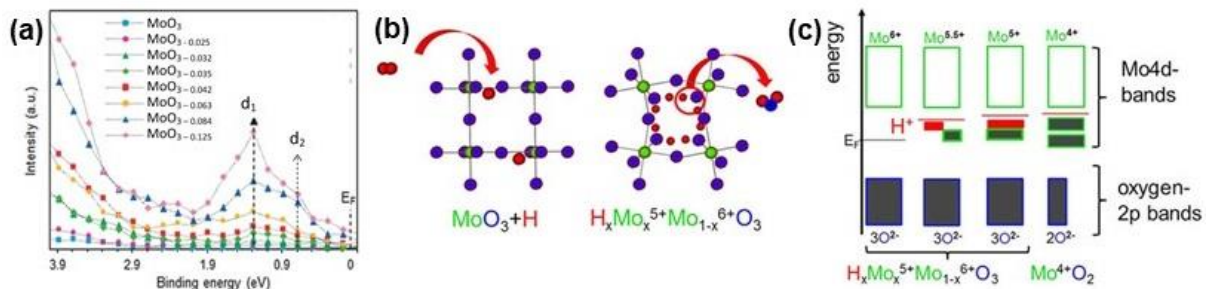
Figure 2.3.   (a) The valence photoemission spectra of MoO_{3-x} showing the defect bands for different x values,[37] (b) simplified crystal structures of MoO_3 and hydrogen molybdenum bronze showing that the intercalation of hydrogen leads to only slight increase in the cell volume, lattice distortion and hydrogen ordering rather than significant change in the MoO_3 crystal and (c) electronic band structure manipulation of MoO_3 by H^+ intercalation.[64]

2.3.1.4. *Electrochemical Properties*

The electrochemical behaviors of molybdenum oxides both in nanostructured and bulk forms have attracted significant attention due to the range of applications, including electrocatalysts,[73] sensors,[74] batteries,[75] solar-cells,[76] and electrochromics.[12] These oxides have been incorporated in a number of electrocatalytic reactions mainly due to their redox nature. The oxidation states of molybdenum oxides range from −II to +VI and coordination numbers from 0 to 8.[21] The redox nature of molybdenum oxides mainly arises due to the flexibility of molybdenum ions in changing their oxidation state, coordination, and/or arrangement of the coordination polyhedra, making these oxides attractive for various electrocatalytic applications.[77] Molybdenum can also be transformed to molybdenum oxide *via* electrochemical means.[4] The nature and composition of the formed surface oxides vary depending on the nature of the medium, electrolyte pH, electrode potential and processing parameters (e.g. temperature).[21] The Pourbaix diagram (**Figure** 2.4) shows the transition of molybdenum structures with regard to the pH and electrochemical potential, which provides important insight into corrosion and electrochemical behavior.[21]
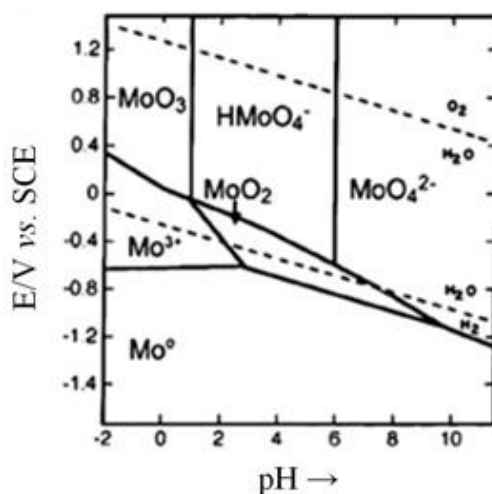
Figure 2.4. Potential–pH diagram of a Mo-H_2O system.[21]

2.3.2. *Synthesis of molybdenum oxides in 2D form*

A variety of methods have been used for synthesizing 2D MoO_3 and its sub-stoichiometric analogous. Synthesis approaches of molybdenum oxides cover processes both in liquid and gas phase media.[4] Solid films are mainly synthesized using vapor deposition techniques, which provides limited avenues for tuning the morphology during the synthesis process.[15] In comparison, liquid phase techniques are more versatile due to facilitating efficient dispersion of the 2D sheets in common solvents and the additional opportunity to deposit the individual flakes as thin films onto desired substrates.[13] Therefore, the 2D sheets dispersed in solvents can be utilized in both liquid and solid state applications. In this section, such methods will be presented and analyzed.

2.3.2.1. *Vapor Phase Synthesis*

Vapor-phase deposition techniques include different approaches involving condensation of vaporized source material onto target substrates. In general, these methods can be categorized into two different main techniques: (i) physical vapor deposition (PVD) and (ii) chemical vapor deposition (CVD).

The PVD deposition of molybdenum oxide involves condensation of vaporized source material onto target substrates.[4] Molybdenum and MoO_3 are mostly used as the source materials, for which the implementation of metallic molybdenum requires the reaction step with oxygen during the PVD process.[4] Although high energy is generally required for vaporizing the source material, the PVD methods are widely used for the fabrication of molybdenum oxide based devices due to their relative scalability and repeatability as well as ability to produce molybdenum oxides with high crystallinity, controlled stoichiometry and morphology.[15, 22]To date, a variety of PVD techniques including sputtering (radio frequency

(RF)[78] and direct current (DC)[79] magnetron sputtering), thermal evaporation,[80] electron beam evaporation,[22] and pulsed laser deposition[81] have been used for the deposition of thin molybdenum oxide and/or nanostructured films.

Synthesis of nanostructured molybdenum oxide using CVD methods generally relies on the thermal decomposition of a volatile molybdenum based precursor. Here energy is required for the sublimation of the precursor, which is much lower in comparison to that of the PVD methods.[4] Currently, molybdenum hexacarbonyl ($Mo(CO)_6$) is the most used precursor in CVD processes. However, due to its toxic nature, CVD growth of molybdenum oxides is not as popular as PVD techniques.[82] Similar to the PVD methods, material properties, stoichiometry and crystal phase of the CVD synthesized molybdenum oxides also strongly depend on the deposition parameters, such as precursor sublimation and substrate temperatures, the amount of precursor and the flow rate of the carrier gas.[26, 83, 84]

2.3.2.2.   *Liquid phase synthesis*

Significant research efforts have been focused on the elaboration of morphology-controllable synthesis techniques of MoO_3 structures, especially for establishing defined nanostructures.[31] In this context, liquid-phase synthesis methods (LPS) are generally chosen since they offer good control over materials' morphologies at low energy requirements and generally do not rely on complex equipment that reduce the need for expert operation skills, when compared with PVD deposition methods.[4]

Exfoliation synthesis techniques are facile and known to produce high quality atomically thin 2D nanosheets and can be conducted either mechanically or in liquid using high power

sonication.[13] These techniques are not costly and can be processed using a range of solvent mixtures chosen from a variety of frequently environmental friendly options.[4]

Orthorhombic α-MoO$_3$ is of special interest for exfoliation due to its layered structure. Exfoliation of thin nanosheets is possible due to the easy cleavage of the crystal at its weak point along the van der Waals gap of the α-MoO$_3$ planes.[31] It has been observed that 2D materials can show unique electronic and optical properties when the number of planes are reduced, due to changes in their electronic band structure.[15] [39, 56] Information regarding the exfoliation synthesis of 2D MoO$_3$ leading to fascinating functionalities can be found in previous reports.[2, 3]

The first example of mechanical exfoliation of MoO$_3$ reported in 2010.[45] It was found that the thinnest stand alone 2D plane that could be produced using mechanical cleavage was 2.8 nm thick, equivalent to two unit cells.[15, 45]

Liquid phase sonication is another exfoliation method that has been investigated as a high-yield approach.[31, 36, 52, 63] High energy probe sonication is most commonly utilized. Micrometer sized particles of layered α- MoO$_3$ are typically sonicated while suspended in a suitable solvent with matching surface tension ($\sim\gamma = -40$ mJ/m^2).[85]**Figure** 2.5 represents a schematic showing the process of exfoliation from bulk to 2D nanosheets. Surfactants can be employed to fine-tune the MoO$_3$–solvent interface.[63] The sonication process applies shear force on the surface of the crystal which results in the delamination of the top layer. Continuous sonication exfoliates the whole bulk of the crystal. Alsaif *et al.*[31] investigated the sonication process and evaluated five different mixtures of water with organic solvents. They have shown that the composition of the solvent environment influences the thickness, lateral dimensions, and synthetic yield of MoO$_3$ nanoflakes.[31] The maximum average thickness of $\sim$26 nm thick nanoflakes has been reported for exfoliation in N-methyl-2-pyrrolidone/water

mixtures, while significantly thinner nanosheets featuring a thickness of ~7 nm were obtained in isopropyl alcohol/water mixtures following an otherwise identical exfoliation process.[31]
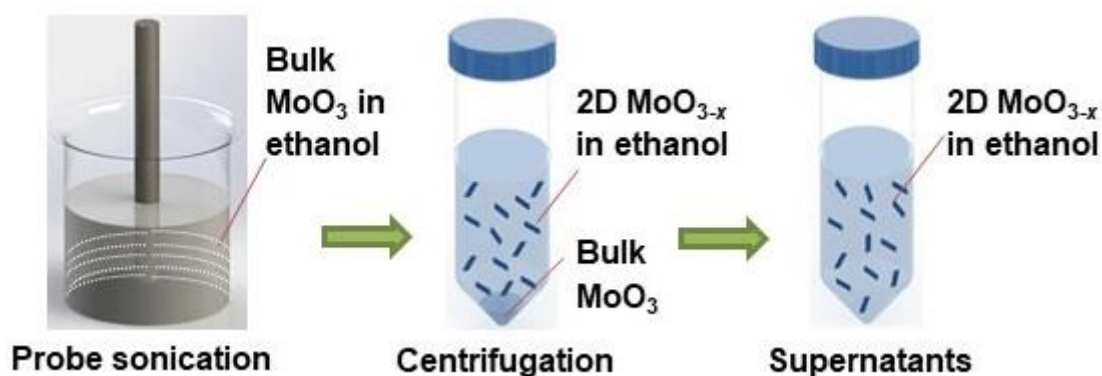
Figure 2.5. A schematic representation of liquid phase exfoliation of bulk molybdenum oxide to 2D molybdenum oxide nanosheet using high power probe sonication.[6]

2.3.3. *Applications of reduced molybdenum oxides and its compounds*

As discussed above, due to the wide versatility and adaptability, molybdenum oxides and its compounds have been utilized in range of applications.[4] In particular, the oxygen deficient or reduced molybdenum oxides facilitate exciting optical and electronic applications and play a significant role in improving their performance.[86] In this section, some of the important applications will be presented and discussed.

MoO_3 has a naturally low free carrier concentration, which is challenging for making transistors.[15] However, facile manipulation of free carrier concentrations and bandgap in molybdenum oxides has led to fabrication of 2D field-effect transistors (FETs).[15] Substoichiometric semiconducting MoO_{3-x} sheets, which are obtained from reducing α-MoO_3, have been reported to display carrier mobility values exceeding 1100 $cm^2V^{-1}s^{-1}$.[15]

Reduced MoO_{3-x} nanoflakes have also been shown to be used as semiconducting ink for printing FETs. Alsaif et al.[37] have successfully tuned the electronic properties of 2D MoO_{3-x} nanosheets by manipulating the level of oxygen deficiencies in such nanofalkes. For a 850 nm film made of nanosheets of MoO_{3-x} ($x = 0.042$), the carrier mobility was reported to be 600 $cm^2V^{-1}s^{-1}$ with a free electron concentration value of 1.6×10^{21} cm^{-3} and an optimal current on/off ratio of above 10^5 for the device.[37]

In general, molybdenum oxides are coated onto electrodes to improve the electrode's charge-injection characteristics.[4] These oxides are used as interfacial layers to reduce the barriers for electrode's charge-injection into the organic semiconductors.[87] MoO_3 presents a very low work function when compared to the other components of the organic solar cell, as shown in **Figure** 2.6a and therefore, have extensively been investigated as hole-injector in organic solar cells.[87] In an organic solar cell, the MoO_3 layer is commonly sandwiched between a solid organic semiconductor and an electrode material as an interfacial layer (**Figure** 2.6b).[87]
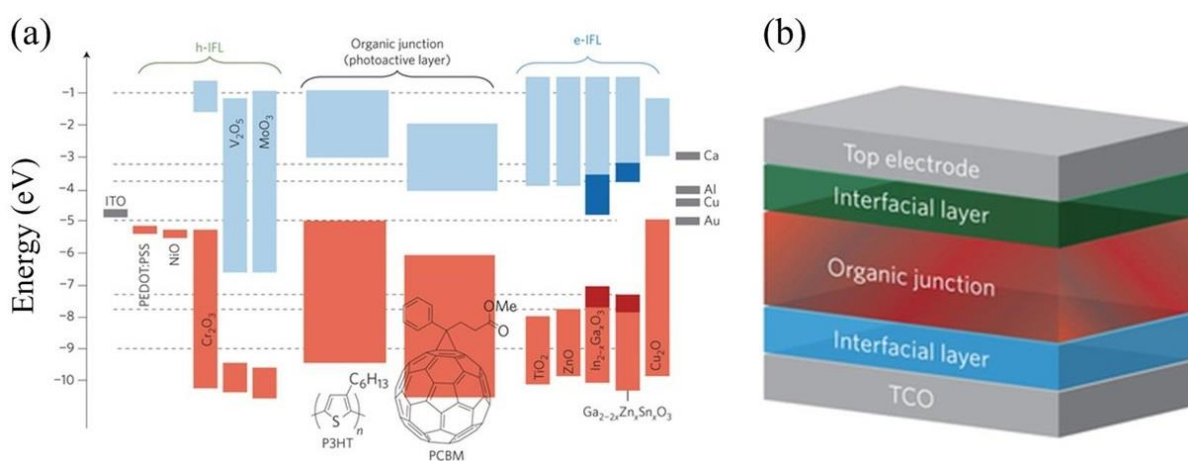
Figure 2.6.   (a) Electronic band diagram of the compounds utilized in organic devices plotted with respect to vacuum level. The grey, light blue and red colored regions indicate the work functions, lowest unoccupied molecular orbital (LUMO) levels and highest occupied

molecular orbital (HOMO) levels, respectively. The dark blue and dark red areas represent the energy range for LUMO and HOMO levels, respectively that rely on the metal oxide composition. Dashed lines are guides for the eyes. (b) A schematic representation of an organic solar cell showing the individual layers of the device architecture. [87]

2.3.3.1.   *Electrocatalysis*

Hydrogen gas (H_2) has been of great interest as a potential energy storage medium for the hypothesized future 'Hydrogen Economy', due to its clean, efficient and sustainable properties compared to fossil fuels (provided that it is generated from renewable energy sources).[88-90] Due to their wide variations and tunable properties, molybdenum oxides and their compounds have gained growing interest for potential application in electrocatalytic hydrogen evolution reactions (HER) for H_2 production.[4, 54, 91, 92] However, relatively modest reaction kinetics due to the lack of active edges limit the extensive use of full stoichiometric α-MoO_3 in electrocatalytic applications.[32] According to the Sabatier principle, a moderate binding of H atom on the catalytic site plays a key role to achieve optimum HER activity, which is presented by near-zero Gibbs free energy ($\Delta G_{ads}(H) \approx 0$) for H atom adsorption on the active sites of an electrocatalyst.[93] Presence of oxygen deficiencies and dislocations are desired to increase the prevalence of such binding sites in molybdenum oxides.[32]

In metal oxide catalysis, surface defects play a vital role for improving the activity of the catalyst.[94] In theory, layered and planar materials with stable oxygen vacancies can be utilized in the electrocatalytic process.[54] In planar molybdenum oxides, oxygen vacancies are accompanied by Mo dangling bonds, creating defect states close to the conduction band minimum.[94, 95] The presence of dangling bonds in oxygen deficient molybdenum oxides make them highly reactive, acting as active sites for HER.[96] A previously reported density

functional theory (DFT) calculations has suggested that the H_2 evolution energy barrier for an oxygen deficient molybdenum oxide is 1.28 eV (with surface Mo^{5+} in comparison to full stoichiometric Mo^{6+}), which is significantly lower than that of bulk MoO_3 (2.63 eV), suggesting its suitability as an electrocatalyst for HER.[32] Introducing surface defect such as oxygen vacancies can cause the emergence of gap states that act as shallow donors in layered TMOs and thus increase the free charge carrier concentration.[97-99] Inducing oxygen vacancies in TMOs has led to faster kinetics compared to their fully oxidized counterparts.[97, 99, 100] Therefore, the presence of oxygen vacancies in the α-MoO_3 lattice (resulting in the formation of α-MoO_{3-x} with $x>0$) is expected to provide more active sites to significantly improve its HER performance due to its ability to facilitate fast charge transfer.[54, 97, 101]

2.4. Transformation of layered molybdenum oxides into non-layered crystals

Metal Molybdate based oxides contain the MoO_4^{2-} unit and form an important type of materials that display various functional properties. Metal molybdates, with relatively large bivalent cations (Ba, Pb, Sr and Ca with ionic radius >0.99 Å), are typically found in the scheelite-type structures of non-layered body centred tetragonal nature.[5] These materials offer chemical and physical properties suitable for different applications such as photocatalysis and electrocatalysis.[102-113] Amongst the family of metal molybdates, lead molybdate ($PbMoO_4$) has shown to offer high stability and interesting photophysical and photocatalytic properties,[5, 108, 114-121] due to its favourable band edge positions that optimizes the driving force required to facilitate oxidation of dye components.[112, 122-125] These types of materials can be derived from facile topotactic reaction between metal salts and molybdenum oxides.

2.4.1. *Synthesis techniques and limitations*

Pb^{2+} based salts in aqueous solutions can react with molybdenum oxides to produce $PbMoO_4$ crystals *via* a facile room-temperature process.[6] **Figure 2.7** represents this reaction and crystal transformation of molybdenum oxide into $PbMoO_4$. Different liquid and gas/vacuum phase synthesis methods have been used for establishing low dimensional $PbMoO_4$ crystals.[6] Thus far, wet chemical synthesis process attracted much attention for synthesizing $PbMoO_4$ crystals.[5] In addition, a range of methods such as solid state reaction,[126] solvothermal,[127] hydrothermal,[108] Czochralski crystal growth,[128] sonochemical,[129] microwave-assisted synthesis,[112, 130] and precipitation method[124] have been widely explored for the synthesis of $PbMoO_4$ crystals. However, majority of these methods are complex synthesis techniques and none of these methods reported the synthesis of large nanosheets with 2D morphologies.

As discussed in the above sections, layered materials of van der Waals nature are traditional sources for synthesizing 2D nanosheets due to their weakly attached layers.[85, 131-133] A range of methods have been adopted to exfoliate layered materials, however, liquid phase exfoliation techniques are the most widely explored methods for high throughput applications.[85, 131] Nevertheless, these techniques cannot be used for exfoliating metal molybdates such as $PbMoO_4$. These materials only exist in non-stratified crystal structures (shown in **Figure** 2.7), and therefore, direct exfoliation into 2D nanosheets is not achievable. This remains a major limitation for these types of materials, since additional functional properties of these materials may emerge, while other properties are expected to be enhanced when synthesized in 2D form.
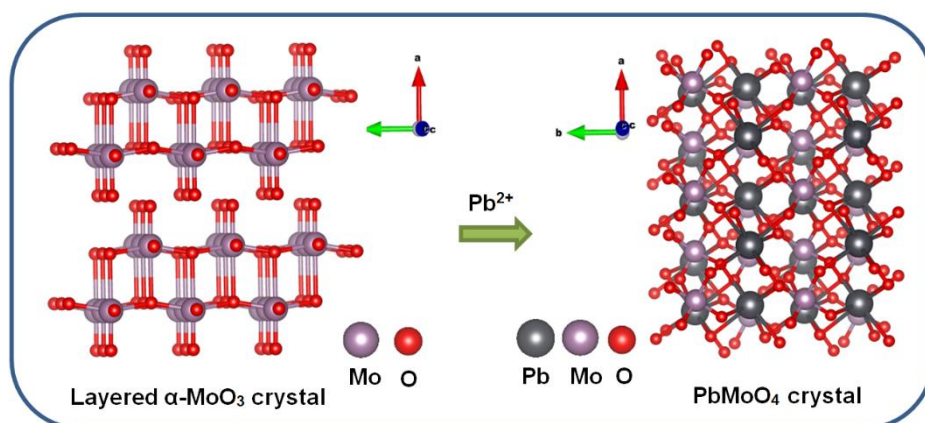
Figure 2.7. Crystal structure of orthorhombic α-MoO$_3$ and its transformation into scheelite-type PbMoO$_4$.[6]

2.4.2. Applications

Metal molybdates have unique chemical and physical properties for applications such as supercapacitors,[102, 103] batteries,[104] scintillator materials,[105, 106] humidity sensors,[110] electrocatalysts,[111] and photocatalysts.[112, 113]

In particular, PbMoO$_4$ is mostly investigated for photocatalytic applications. With rising concern regarding environmental remediation, photocatalysis is of particular interest due to its application in many chemical practices for the removal of toxic reagents in water and air using solar energy.[129, 134-136] Therefore, the search and application of various photocatalysts has gained importance for decomposing organic pollutants.[135] In this process, gradual degradation of the characteristic absorbance spectrum for a model organic dye with the aid of photocatalysts (2D nanosheets) under solar or UV light irradiation is investigated to evaluate their photocatalytic performances.

Inability to absorb efficient amount of solar light and fast deactivation of photocatalysts, deteriorate the photocatalytic applications of many of the materials.[136] In the past, metal molybdates, such as PbMoO$_4$ have shown reasonable photocatalytic performance compared

to the other molybdates and tungstates reported in literatures due to its favourable band position.[112, 123-125] However, due to its relatively wide bandgap, the photocatalytic activity of this material with different morphologies has been mainly tested using UV irradiation.[124] This is still a major limitation for the application of $PbMoO_4$ as a photocatalyst. Therefore, it is required to shift its photo-response towards the visible range, which may create the possibility of this material to be tested under solar light irradiation.[6] Doping and compounding can be a possible way to reduce the bandgap of this type of material,[114, 129] however, this will require additional synthesis steps and may create instability. Recently, formation of trap states in a quasi- 2D wide bandgap metal oxide has shown to shift the photo-response of the material for effective absorption of solar light resulting in enhanced photocatalytic performance without any doping.[135] The possibility of creating trap states within the bandgap of $PbMoO_4$ can potentially bring the photocatalytic operation into the visible light region. However, this approach has not been explored to date.

2.5.   Synthesis of Non-layered ultrathin large area 2D metal oxide nanosheets using liquid metal reaction environment

Liquid metals have been recently introduced as a reaction medium that facilitates the formation of large area 2D oxides of the non-layered crystals.[6, 8, 137-140] Low melting point post transition metals such as Ga, In and Sn undergo self-limiting Cabrera-Mott oxidation in air, leading to the formation of nanometre thin surface oxides.[140] If the metal is in its liquid state, adhesion of the surface oxide to the parent metal is minimal, allowing to apply van der Waals transfer techniques for transferring the grown oxide sheet onto desired substrates.[6, 8, 139, 140] When alloys are used, the surface oxide is dominated by the oxide that provides the greatest reduction in Gibbs free energy.[8] In most cases this leads to the surface oxide of low

melting liquid alloys being dominated by a binary oxide. This has been exploited for creating a variety of high quality 2D metal oxides that could be grown on the surface of complex low melting alloys which effectively function as a reaction solvent.[8] For example, surface composition of gallium based liquid metal alloys, such as gallium-indium-tin and gallium-indium, mainly produces gallium oxide skins in ambient conditions,[141, 142] despite the presence of indium and tin within both alloy compositions. The composition of the surface oxide is found to depend on the more favourable (i.e. more negative) Gibbs free energy of formation for the metal oxides that could grow on an alloy.[141, 142] Recently, this phenomena was successfully exploited for creating a variety of 2D materials using gallium based alloys.[8] Here, metals with oxides that feature a more negative Gibbs free energy of formation than gallium oxide, such as hafnium, aluminium and gadolinium were investigated (see **Figure** 2.8 a, b).[8] The grown oxide layer is isolated by gently touching the surface of the liquid metal alloy with a solid substrate. The direct transfer of the surface oxide onto a substrate surface is possible due to van der Waals attraction forces (see **Figure** 2.8c).[8]

As mentioned above, the oxide that provides the greatest reduction in Gibbs free energy is usually a binary compound, leading to single metal oxides dominating most liquid alloys. However, indium-tin alloys constitute an exception, since their surface oxide has been shown to be a ternary compound that contains both indium and tin, with an indium-tin ratio that resembles ITO.[143] The high solubility of tin ions in indium oxide likely allows for the formation of a ternary oxide on the surface of these alloys, leading to ITO being thermodynamically favoured over pure In_2O_3 and SnO_2.[143, 144]
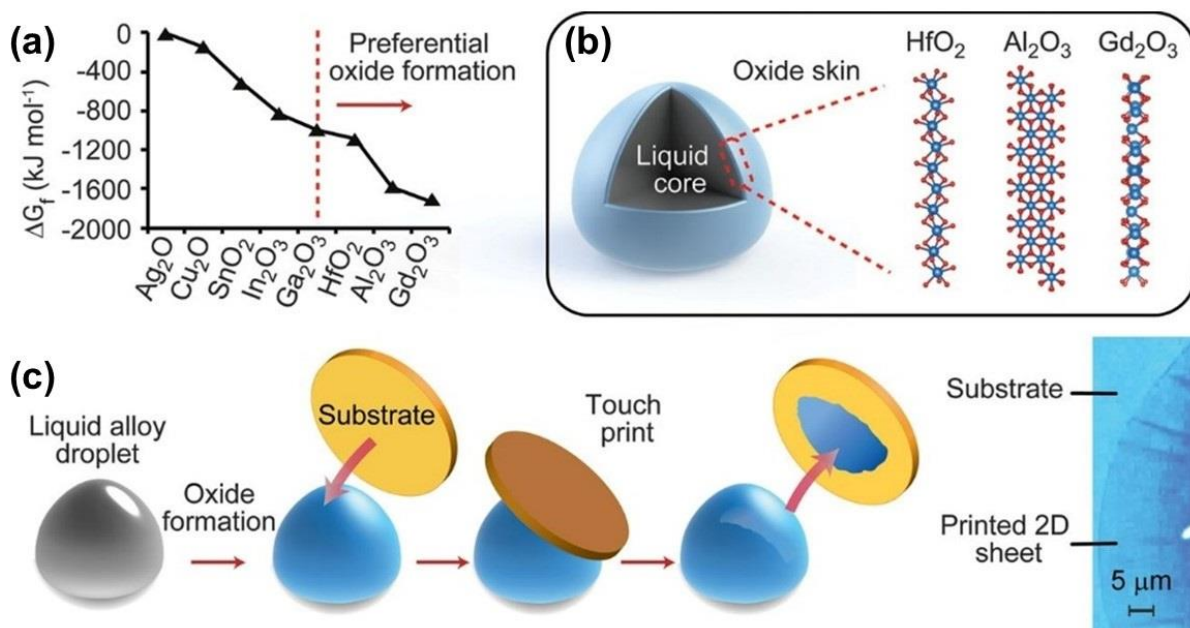
Figure 2.8. (a) Favourable Gibbs energy of a metal oxide within the alloy. The dominant oxides at the interface are indicated to the right of the red dashed line, (b) cross section of a liquid metal droplet, with probable crystal formation of thin layers of HfO_2, Al_2O_3, and Gd_2O_3 as indicated, and (c) schematic illustration of the van der Waals exfoliation method. The liquid metal droplet is initially exposed to an oxygen-containing medium. Touching the surface of the liquid metal droplet using a suitable solid substrate. Transfer of the interfacial oxide layer after touching. An optical image is also presented at the right.[8]

2.5.1. Non-layered metal oxides as TCOs

TCOs are typically non-layered doped metal oxide compounds.[145] These types of materials gained tremendous economic importance due to their unique electronic band structure that enables high conductivity, while simultaneously rendering the material transparent in the visible range.[9, 146, 147] The most prominent application of TCOs is as transparent electrodes in liquid crystal displays, organic light emitting diodes and touch responsive screens, which enabled the smartphone and flat panel monitor revolution, leading to a total global market for

TCOs (across all applications) of approximately \$7 bn.[147] Further applications include low emission windows,[9, 148, 149] a variety of optoelectronic devices,[150] solar cells,[9, 146, 151] plasmonics [152-154] and lab-on-a-chip biosensing.[155]

High performance TCOs are usually based on a select few binary oxides, with In_2O_3, SnO_2 and ZnO being dominant.[146] The reason for this is the comparatively low effective electron mass that can be realized in these systems, leading to high carrier mobilities, and in turn reduced sheet resistance.[9, 146] Heavy doping of these oxides is then utilized to increase the carrier concentration to a level where a carrier population above the conduction band minimum is created, allowing the material to achieve a conductivity that is only 2 orders of magnitude below that of metals.[9] The high transparency of TCOs originates from a pronounced Moss-Burstein shift that leads to optical bandgaps substantially wider than the electronic gap.[146]

2.5.2. Materials, synthesis and challenges

Tin doped indium oxide is one of the most important TCOs due its superior performance and the substantial developed knowledge base associated with its decades-long industrial use.[156] One of the main drawbacks of ITO is that it is commonly deposited using physical vapor-based deposition techniques that rely on vacuum technology and batch processing.[9, 147, 157-159] The typical film thickness of the deposited TCOs is in the range of 50 to 500 nm and due to their ceramic nature, these films are inherently brittle and thus incompatible with flexible electronics.[160] Furthermore, indium in ITO is an element with relatively low abundance and high cost, and while the worlds indium reserves are estimated to be sufficient to support global demand well into the 21st century, the reliance on comparatively thick ITO films may ultimately prove to be unsustainable and too costly.[161]

In response to these challenges, numerous alternative approaches towards creating transparent conductive systems have been proposed, with networks of conductive nanowires and large area graphene being intensely investigated.[156, 162-165] The utilization of nanowires is intrinsically incapable of producing a gap-free conductive surface, significantly limiting their use in numerous technologies.[166, 167] Graphene, on the other hand, allows achieving good conductivity and flexibility, while counterproductively leading to significant light absorption, with each layer of graphene absorbing approximately 2.5% of light in the visible spectrum.[156] Further limitations of graphene include the high temperature synthesis of large surface area graphene, which requires growth on metallic substrates or foils prior to being transferred onto the desired glass or polymer substrates.[156] The lack of micro and nano crystalline features for large area deposited graphene also leads to defect mediated crack propagation, rendering it substantially more brittle than micrometre sized sheets that have been mechanically exfoliated from graphite crystals.[168] As such, novel transparent and conductive materials that can overcome these limitations are highly sought after and the van der Waals exfoliation technique using liquid metal reaction medium can be an interesting route to solve these problems.

2.6.   Conclusion and outlook

The fundamentals and main applications of molybdenum oxides, as well as a selection of synthesis methods to obtain 2D morphologies of these oxides have been discussed. Doping and compounding this material is identified as the means to achieve highly efficient catalysts, electronic materials, sensors, optoelectronic devices, and electrochemical systems. Synthesis section mostly focused on the formation of 2D orthorhombic molybdenum oxides as they offer significant properties such as defect band within the bandgap upon the loss of oxygen,

plasmonic features in their sub-stoichiometric forms and significant surface-to-volume ratio that can be potentially used for many future advanced applications including electrocatalysts.

Metal molybdates, another important class of metal oxide compounds, offer interesting photophysical and photocatalytic properties due to their favourable band positions. These types of materials are typically found as non-layered crystals with scheelite-type structures of body centred tetragonal nature, which can be derived from molybdenum oxides. Amongst the family of metal molybdates, lead molybdate ($PbMoO_4$) has shown to offer high stability and has been proven as an excellent photocatalyst. However, due to non-stratified crystal structures direct exfoliation of these materials into 2D nanosheets is not feasible. This remains a major limitation for these types of materials as many of the functional properties of these materials cannot be realized unless they are synthesized in 2D form.

Another important class of non-layered metal oxides are TCOs. These types of materials gained remarkable economic importance due to their unique electronic band structure that enables high conductivity, while simultaneously rendering the material transparent in the visible range. ITO is identified as one of the most important and best performing TCOs. However, flexible and low temperature synthesis of this material is still a challenge in the decade long research filed, which needs considerable attention to address.

2.7. References

1. Tiwari, J.N., Tiwari, R.N. & Kim, K.S. Zero-dimensional, one-dimensional, two-dimensional and three-dimensional nanostructured materials for advanced electrochemical energy devices. *Prog. Mater. Sci.* **57**, 724-803 (2012).

2. Balendhran, S. et al. Two-Dimensional Molybdenum Trioxide and Dichalcogenides. *Adv. Funct. Mater.* **23**, 3952-3970 (2013).

3. Kalantar-zadeh, K. et al. Two dimensional and layered transition metal oxides. *Appl. Mater. Today* **5**, 73-89 (2016).

4. de Castro, I.A. et al. Molybdenum Oxides – From Fundamentals to Functionality. *Adv. Mater.* **29**, 1701619 (2017).

5. Bomio, M.R.D. et al. Toward Understanding the Photocatalytic Activity of $PbMoO_4$ Powders with Predominant (111), (100), (011), and (110) Facets. A Combined Experimental and Theoretical Study. *J. Phys. Chem. C* **117**, 21382-21395 (2013).

6. Datta, R.S. et al. Two dimensional $PbMoO_4$: A photocatalytic material derived from a naturally non-layered crystal. *Nano Energy* **49**, 237-246 (2018).

7. Xiao, X. et al. Scalable salt-templated synthesis of two-dimensional transition metal oxides. *Nat. Commun.* **7**, 11296 (2016).

8. Zavabeti, A. et al. A liquid metal reaction environment for the room-temperature synthesis of atomically thin metal oxides. *Science* **358**, 332 (2017).

9. Ellmer, K. Past achievements and future challenges in the development of optically transparent electrodes. *Nat. Photonics* **6**, 809 (2012).

10. Novoselov, K.S. et al. Electric Field Effect in Atomically Thin Carbon Films. *Science* **306**, 666 (2004).

11. Lu, J. et al. Ultrasensitive Phototransistor Based on K-Enriched MoO_3 Single Nanowires. *J. Phys. Chem. C* **116**, 22015-22020 (2012).

12. Yao, D.D., Rani, R.A., O'Mullane, A.P., Kalantar-zadeh, K. & Ou, J.Z. Enhanced Coloration Efficiency for Electrochromic Devices based on Anodized Nb_2O_5/Electrodeposited MoO_3 Binary Systems. *J. Phys. Chem. C* **118**, 10867-10873 (2014).

13. Alsaif, M.M.Y.A. et al. Two dimensional α-MoO$_3$ nanoflakes obtained using solvent-assisted grinding and sonication method: Application for H$_2$ gas sensing. *Sens. Actuator B-Chem.* **192**, 196-204 (2014).

14. Hu, X., Zhang, W., Liu, X., Mei, Y. & Huang, Y. Nanostructured Mo-based electrode materials for electrochemical energy storage. *Chem. Soc. Rev.* **44**, 2376-2404 (2015).

15. Balendhran, S. et al. Enhanced Charge Carrier Mobility in Two-Dimensional High Dielectric Molybdenum Oxide. *Adv. Mater.* **25**, 109-114 (2013).

16. Xu, Z., Zhang, Q. & Zhai, W. Wear and friction behaviour of TiAl matrix self-lubricating composites filled with WS$_2$, MoO$_3$ or multilayer graphene. *RSC Adv.* **5**, 93554-93562 (2015).

17. Kuzovnikov, M.A., Meng, H. & Tkacz, M. Nonstoichiometric molybdenum hydride. *J. Alloys Compd.* **694**, 51-54 (2017).

18. Xu, J. et al. High thermoelectric performance of reduced lanthanide molybdenum oxides densified by spark plasma sintering. *J. Alloys Compd.* **500**, 22-25 (2010).

19. Krishnamoorthy, K., Veerapandian, M., Yun, K. & Kim, S.J. New function of molybdenum trioxide nanoplates: Toxicity towards pathogenic bacteria through membrane stress. *Colloids Surf. B* **112**, 521-524 (2013).

20. Rouhani, M. et al. The influence of initial stoichiometry on the mechanism of photochromism of molybdenum oxide amorphous films. *Sol. Energy Mater Sol. Cells* **126**, 26-35 (2014).

21. Saji, V.S. & Lee, C.-W. Molybdenum, Molybdenum Oxides, and their Electrochemistry. *ChemSusChem* **5**, 1146-1161 (2012).

22. Sivakumar, R., Gopalakrishnan, R., Jayachandran, M. & Sanjeeviraja, C. Characterization on electron beam evaporated α-MoO$_3$ thin films by the influence of substrate temperature. *Curr. Appl. Phys.* **7**, 51-59 (2007).

23. Santhosh, S. et al. Effect of Ablation Rate on the Microstructure and Electrochromic Properties of Pulsed-Laser-Deposited Molybdenum Oxide Thin Films. *Langmuir* **33**, 19-33 (2017).

24. Chang, W.-C. et al. Post-deposition annealing control of phase and texture for the sputtered MoO_3 films. *CrystEngComm* **13**, 5125-5132 (2011).

25. Di Yao, D., Field, M.R., O'Mullane, A.P., Kalantar-zadeh, K. & Ou, J.Z. Electrochromic properties of TiO_2 nanotubes coated with electrodeposited MoO_3. *Nanoscale* **5**, 10353-10359 (2013).

26. Ashraf, S., Blackman, C.S., Hyett, G. & Parkin, I.P. Aerosol assisted chemical vapour deposition of MoO_3 and MoO_2 thin films on glass from molybdenum polyoxometallate precursors; thermophoresis and gas phase nanoparticle formation. *J. Mater. Chem.* **16**, 3575-3582 (2006).

27. Chithambararaj, A., Rajeswari Yogamalar, N. & Bose, A.C. Hydrothermally Synthesized h-MoO_3 and α-MoO_3 Nanocrystals: New Findings on Crystal-Structure-Dependent Charge Transport. *Cryst. Growth Des.* **16**, 1984-1995 (2016).

28. Cong, S. et al. Growth and Extension of One-Step Sol–Gel Derived Molybdenum Trioxide Nanorods via Controlling Citric Acid Decomposition Rate. *Cryst. Growth Des.* **15**, 4536-4542 (2015).

29. Xiao, S.J. et al. Highly Photoluminescent Molybdenum Oxide Quantum Dots: One-Pot Synthesis and Application in 2,4,6-Trinitrotoluene Determination. *ACS Appl. Mater. Interfaces* **8**, 8184-8191 (2016).

30. Wang, S. et al. Hydrothermal route to single crystalline α-MoO_3 nanobelts and hierarchical structures. *Solid State Commun.* **136**, 283-287 (2005).

31.   Alsaif, M.M.Y.A. et al. Exfoliation Solvent Dependent Plasmon Resonances in Two-Dimensional Sub-Stoichiometric Molybdenum Oxide Nanoflakes. *ACS Appl. Mater. Interfaces* **8**, 3482-3493 (2016).

32.   Luo, Z. et al. Mesoporous MoO_{3-x} Material as an Efficient Electrocatalyst for Hydrogen Evolution Reactions. *Adv. Energy Mater.* **6**, 1600528-n/a (2016).

33.   Qu, Q., Zhang, W.-B., Huang, K. & Chen, H.-M. Electronic structure, optical properties and band edges of layered MoO_3: A first-principles investigation. *Comput. Mater. Sci.* **130**, 242-248 (2017).

34.   Jittiarporn, P., Sikong, L., Kooptarnond, K. & Taweepreda, W. Effects of precipitation temperature on the photochromic properties of h-MoO_3. *Ceram. Int.* **40**, 13487-13495 (2014).

35.   Scanlon, D.O. et al. Theoretical and Experimental Study of the Electronic Structures of MoO_3 and MoO_2. *J. Phys. Chem. C* **114**, 4636-4645 (2010).

36.   Alsaif, M.M.Y.A. et al. Substoichiometric two-dimensional molybdenum oxide flakes: a plasmonic gas sensing platform. *Nanoscale* **6**, 12780-12791 (2014).

37.   Alsaif, M.M.Y.A. et al. High-Performance Field Effect Transistors Using Electronic Inks of 2D Molybdenum Oxide Nanoflakes. *Adv. Funct. Mater.* **26**, 91-100 (2016).

38.   Greenblatt, M. Molybdenum oxide bronzes with quasi-low-dimensional properties. *Chem. Rev.* **88**, 31-53 (1988).

39.   Huang, Q., Hu, S., Zhuang, J. & Wang, X. MoO_{3-x}-Based Hybrids with Tunable Localized Surface Plasmon Resonances: Chemical Oxidation Driving Transformation from Ultrathin Nanosheets to Nanotubes. *Chem. Eur. J* **18**, 15283-15287 (2012).

40.   Rajagopal, S., Bharaneswari, M., Nataraj, D., Khyzhun, O.Y. & Djaoued, Y. Systematic synthesis and analysis of change in morphology, electronic structure and photoluminescence properties of 2,2[prime or minute]-dipyridyl intercalated MoO_3

hybrid nanostructures and investigation of their photocatalytic activity. *RSC Adv.* **6**, 88287-88299 (2016).

41.   Dong, W. et al. Bifunctional MoO_3–WO_3/Ag/MoO_3–WO_3 Films for Efficient ITO–Free Electrochromic Devices. *ACS Appl. Mater. Interfaces* **8**, 33842-33847 (2016).

42.   Carcia, P.F. & McCarron, E.M. Synthesis and properties of thin film polymorphs of molybdenum trioxide. *Thin Solid Films* **155**, 53-63 (1987).

43.   Yao, D.D. et al. Electrodeposited α- and β-Phase MoO_3 Films and Investigation of Their Gasochromic Properties. *Cryst. Growth Des.* **12**, 1865-1870 (2012).

44.   Mai, L. et al. Molybdenum oxide nanowires: synthesis & properties. *Mater. Today* **14**, 346-353 (2011).

45.   Kalantar-zadeh, K. et al. Synthesis of nanometre-thick MoO_3 sheets. *Nanoscale* **2**, 429-433 (2010).

46.   Lei, Y.-H. & Chen, Z.-X. A theoretical study of stability and vacancy replenishing of MoO_3(010) surfaces in oxygen atmosphere. *Appl. Surf. Sci.* **361**, 107-113 (2016).

47.   Li, Y. et al. Flexible electrode for long-life rechargeable sodium-ion batteries: effect of oxygen vacancy in MoO_{3-x}. *J. Mater. Chem. A* **4**, 5402-5405 (2016).

48.   Meyer, J. et al. Transition Metal Oxides for Organic Electronics: Energetics, Device Physics and Applications. *Adv. Mater.* **24**, 5408-5427 (2012).

49.   Chithambararaj, A. & Bose, A.C. Investigation on structural, thermal, optical and sensing properties of meta-stable hexagonal MoO_3 nanocrystals of one dimensional structure. *Beilstein J. Nanotechnol.* **2**, 585-592 (2011).

50.   Ramana, C.V. et al. Low-temperature synthesis of morphology controlled metastable hexagonal molybdenum trioxide (MoO_3). *Solid State Commun.* **149**, 6-9 (2009).

51. Zheng, L., Xu, Y., Jin, D. & Xie, Y. Novel Metastable Hexagonal MoO$_3$ Nanobelts: Synthesis, Photochromic, and Electrochromic Properties. *Chem. Mater.* **21**, 5681-5690 (2009).

52. Hanlon, D. et al. Production of Molybdenum Trioxide Nanosheets by Liquid Exfoliation and Their Application in High-Performance Supercapacitors. *Chem. Mater.* **26**, 1751-1763 (2014).

53. Huang, P.-R., He, Y., Cao, C. & Lu, Z.-H. Impact of lattice distortion and electron doping on α-MoO$_3$ electronic structure. *Sci. Rep.* **4**, 7131 (2014).

54. Li, L., Zhang, T., Yan, J., Cai, X. & Liu, S. P Doped MoO$_{3-x}$ Nanosheets as Efficient and Stable Electrocatalysts for Hydrogen Evolution. *Small* **13**, 1700441 (2017).

55. Boukhachem, A. et al. Structural, optical, vibrational and photoluminescence studies of Sn-doped MoO$_3$ sprayed thin films. *Mater. Res. Bull.* **72**, 252-263 (2015).

56. Alsaif, M.M.Y.A. et al. Tunable Plasmon Resonances in Two-Dimensional Molybdenum Oxide Nanoflakes. *Adv. Mater.* **26**, 3931-3937 (2014).

57. Xiang, D., Han, C., Zhang, J. & Chen, W. Gap States Assisted MoO$_3$ Nanobelt Photodetector with Wide Spectrum Response. *Sci. Rep.* **4**, 4891 (2014).

58. Lu, X. et al. Preparation of MoO$_3$ QDs through combining intercalation and thermal exfoliation. *J. Mater. Chem. C* **4**, 6720-6726 (2016).

59. Tan, X. et al. Plasmonic MoO$_{3-x}$@MoO$_3$ nanosheets for highly sensitive SERS detection through nanoshell-isolated electromagnetic enhancement. *Chem. Commun.* **52**, 2893-2896 (2016).

60. Vasilopoulou, M. et al. The Influence of Hydrogenation and Oxygen Vacancies on Molybdenum Oxides Work Function and Gap States for Application in Organic Optoelectronics. *J. Am. Chem. Soc.* **134**, 16178-16187 (2012).

61. Hu, Z., Liu, G., Chen, X., Shen, Z. & Yu, J.C. Enhancing Charge Separation in Metallic Photocatalysts: A Case Study of the Conducting Molybdenum Dioxide. *Adv. Funct. Mater.* **26**, 4445-4455 (2016).

62. Ou, J.Z., Campbell, J.L., Yao, D., Wlodarski, W. & Kalantar-zadeh, K. In Situ Raman Spectroscopy of H_2 Gas Interaction with Layered MoO_3. *J. Phys. Chem. C* **115**, 10757-10763 (2011).

63. Ji, F. et al. 2D-MoO_3 nanosheets for superior gas sensors. *Nanoscale* **8**, 8696-8703 (2016).

64. Borgschulte, A. et al. Hydrogen reduction of molybdenum oxide at room temperature. *Sci. Rep.* **7**, 40761 (2017).

65. Kovendhan, M. et al. 'Li' doping induced physicochemical property modifications of MoO_3 thin films. *Appl. Surf. Sci.* **284**, 624-633 (2013).

66. Tahini, H.A. et al. Mobile Polaronic States in α-MoO_3: An ab Initio Investigation of the Role of Oxygen Vacancies and Alkali Ions. *ACS Appl. Mater. Interfaces* **8**, 10911-10917 (2016).

67. Sanal Kumar, G. et al. Terbium oxide doped MoO_3 nanostructures: Morphology engineering and enhanced photoluminescence. *J. Alloys Compd.* **698**, 215-227 (2017).

68. Xu, R. et al. One-step synthesis and the enhanced xylene-sensing properties of Fe-doped MoO_3 nanobelts. *RSC Adv.* **6**, 106364-106369 (2016).

69. Phuruangrat, A., Cheed-Im, U., Thongtem, T. & Thongtem, S. High visible light photocatalytic activity of Eu-doped MoO_3 nanobelts synthesized by hydrothermal method. *Mater. Lett.* **172**, 166-170 (2016).

70. Wang, M. & Koski, K.J. Reversible Chemochromic MoO_3 Nanoribbons through Zerovalent Metal Intercalation. *ACS Nano* **9**, 3226-3233 (2015).

71. Liu, Z., Jin, Y., Teng, F., Hua, X. & Chen, M. An efficient Ce-doped MoO_3 catalyst and its photo-thermal catalytic synergetic degradation performance for dye pollutant. *Catal. Commun.* **66**, 42-45 (2015).

72. Ren, P. et al. Green photoluminescence from erbium-doped molybdenum trioxide. *Mater. Lett.* **122**, 320-322 (2014).

73. Kosminsky, L., Matos, R.C., Tabacniks, M.H. & Bertotti, M. Electrochemical Codeposition of Platinum and Molybdenum Oxides: Formation of Composite Films with Distinct Electrocatalytic Activity for Hydrogen Peroxide Detection. *Electroanalysis* **15**, 733-738 (2003).

74. Balendhran, S. et al. Field Effect Biosensing Platform Based on 2D α-MoO_3. *ACS Nano* **7**, 9753-9760 (2013).

75. Mai, L.Q. et al. Lithiated MoO_3 Nanobelts with Greatly Improved Performance for Lithium Batteries. *Adv. Mater.* **19**, 3712-3716 (2007).

76. Battaglia, C. et al. Hole Selective MoO_x Contact for Silicon Solar Cells. *Nano Lett.* **14**, 967-971 (2014).

77. Labanowska, M. EPR Monitoring of Redox Processes in Transition Metal Oxide Catalysts. *ChemPhysChem* **2**, 712-731 (2001).

78. Priyanka, D., Saakshi, D. & Samaresh, D. Synthesis of α-MoO_3 nano-flakes by dry oxidation of RF sputtered Mo thin films and their application in gas sensing. *Semicond. Sci. Technol.* **31**, 115010 (2016).

79. Yordanov, R., Boyadjiev, S., Georgieva, V. & Vergov, L. Characterization of thin MoO_3 films formed by RF and DC-magnetron reactive sputtering for gas sensor applications. *J Phys Conf Ser.* **514**, 012040 (2014).

80. Siciliano, T., Tepore, A., Filippo, E., Micocci, G. & Tepore, M. Characteristics of molybdenum trioxide nanobelts prepared by thermal evaporation technique. *Mater. Chem. Phys* **114**, 687-691 (2009).

81. Al-Kuhaili, M.F., Durrani, S.M.A. & Bakhtiari, I.A. Pulsed laser deposition of molybdenum oxide thin films. *Appl. Phys. A* **98**, 609-615 (2010).

82. Szekeres, A., Ivanova, T. & Gesheva, K. Spectroscopic ellipsometry study of CVD molybdenum oxide films: effect of temperature. *J. Solid State Electrochem.* **7**, 17-20 (2002).

83. Donnadieu, A., Davazoglou, D. & Abdellaoui, A. Structure, optical and electro-optical properties of polycrystalline WO_3 and MoO_3 thin films prepared by chemical vapour deposition. *Thin Solid Films* **164**, 333-338 (1988).

84. Ivanova, T., Gesheva, K.A., Popkirov, G., Ganchev, M. & Tzvetkova, E. Electrochromic properties of atmospheric CVD MoO_3 and MoO_3–WO_3 films and their application in electrochromic devices. *Mater. Sci. Eng. B.* **119**, 232-239 (2005).

85. Coleman, J.N. et al. Two-Dimensional Nanosheets Produced by Liquid Exfoliation of Layered Materials. *Science* **331**, 568 (2011).

86. Datta, R.S. et al. Highly active two dimensional α-$MoO_{3−x}$ for the electrocatalytic hydrogen evolution reaction. *J. Mater. Chem. A* **5**, 24223-24231 (2017).

87. Yu, X., Marks, T.J. & Facchetti, A. Metal oxides for optoelectronic applications. *Nat. Mater.* **15**, 383 (2016).

88. Xie, J. et al. Defect-Rich MoS_2 Ultrathin Nanosheets with Additional Active Edge Sites for Enhanced Electrocatalytic Hydrogen Evolution. *Adv. Mater.* **25**, 5807-5813 (2013).

89. Thangasamy, P., Ilayaraja, N., Jeyakumar, D. & Sathish, M. Electrochemical cycling and beyond: unrevealed activation of MoO_3 for electrochemical hydrogen evolution reactions. *Chem. Commun.* **53**, 2245-2248 (2017).

90. Najafpour, M.M. et al. Transformation of $La_{0.65}Sr_{0.35}MnO_3$ in electrochemical water oxidation. *Int. J. Hydrog. Energy* **42**, 8560-8568 (2017).

91. Wang, C., Tian, B., Wu, M. & Wang, J. Revelation of the Excellent Intrinsic Activity of $MoS_2|NiS|MoO_3$ Nanowires for Hydrogen Evolution Reaction in Alkaline Medium. *ACS Appl. Mater. Interfaces* **9**, 7084-7090 (2017).

92. Chen, Z. et al. Core–shell MoO_3–MoS_2 Nanowires for Hydrogen Evolution: A Functional Design for Electrocatalytic Materials. *Nano Lett.* **11**, 4168-4175 (2011).

93. Huang, Z. et al. Dimeric $[Mo_2S_{12}]_2^-$ Cluster: A Molecular Analogue of MoS_2 Edges for Superior Hydrogen-Evolution Electrocatalysis. *Angew. Chem. Int. Ed.* **54**, 15181-15185 (2015).

94. Chen, M., Friend, C.M. & Kaxiras, E. The Chemical Nature of Surface Point Defects on MoO_3(010): Adsorption of Hydrogen and Methyl. *J. Am. Chem. Soc.* **123**, 2224-2230 (2001).

95. K. C, S., Longo, R.C., Addou, R., Wallace, R.M. & Cho, K. Electronic properties of MoS_2/MoO_x interfaces: Implications in Tunnel Field Effect Transistors and Hole Contacts. *Sci. Rep.* **6**, 33562 (2016).

96. Sun, Y., Gao, S., Lei, F. & Xie, Y. Atomically-thin two-dimensional sheets for understanding active sites in catalysis. *Chem. Soc. Rev.* **44**, 623-636 (2015).

97. Kim, H.-S. et al. Oxygen vacancies enhance pseudocapacitive charge storage properties of MoO_{3-x}. *Nat. Mater.* **16**, 454 (2017).

98. Zhuiykov, S., Kats, E., Carey, B. & Balendhran, S. Proton intercalated two-dimensional WO_3 nano-flakes with enhanced charge-carrier mobility at room temperature. *Nanoscale* **6**, 15029-15036 (2014).

99. Jin, H., Wang, L., Searles, D.J. & Sun, C. Comparison of the effect of hydrogen incorporation and oxygen vacancies on the properties of anatase TiO_2: electronics, optical absorption, and interaction with water. *Chin. Sci. Bull.* **59**, 2175-2180 (2014).

100. Wang, G., Ling, Y. & Li, Y. Oxygen-deficient metal oxide nanostructures for photoelectrochemical water oxidation and other applications. *Nanoscale* **4**, 6682-6691 (2012).

101. Haque, F. et al. Ordered intracrystalline pores in planar molybdenum oxide for enhanced alkaline hydrogen evolution. *J. Mater. Chem. A* (2019).

102. Mai, L.-Q. et al. Hierarchical $MnMoO_4$/$CoMoO_4$ Heterostructured Nanowires with Enhanced Supercapacitor Performance. *Nat. Commun.* **2**, 381 (2011).

103. Zhang, Z. et al. Facile Hydrothermal Synthesis of $NiMoO_4$@$CoMoO_4$ Hierarchical Nanospheres for Supercapacitor Applications. *Phys. Chem. Chem. Phys.* **17**, 20795-20804 (2015).

104. Xiao, W., Chen, J.S., Li, C.M., Xu, R. & Lou, X.W. Synthesis, Characterization, and Lithium Storage Capability of $AMoO_4$ (A = Ni, Co) Nanorods. *Chem. Mater.* **22**, 746-754 (2010).

105. Mikhailik, V.B. & Kraus, H. Performance of Scintillation Materials at Cryogenic Temperatures. *Phys. Status Solidi B* **247**, 1583-1599 (2010).

106. Mikhailik, V.B. et al. Structure, Luminescence and Scintillation Properties of the $MgWO_4$–$MgMoO_4$ System. *J. Phys. Condens. Matter* **20**, 365219 (2008).

107. Zhen, L. et al. High Photocatalytic Activity and Photoluminescence Property of Hollow $CdMoO_4$ Microspheres. *Scr. Mater.* **58**, 461-464 (2008).

108. Sczancoski, J.C. et al. Morphology and Blue Photoluminescence Emission of PbMoO$_4$ Processed in Conventional Hydrothermal. *J. Phys. Chem. C* **113**, 5812-5822 (2009).

109. Kajitani, T. & Itoh, M. Time-Resolved Composite Nature of the Self-Trapped Exciton Luminescence in PbMoO$_4$. *Phys. Status Solidi C* **8**, 108-111 (2011).

110. Sundaram, R. & Nagaraja, K.S. Solid State Electrical Conductivity and Humidity Sensing Studies on Metal Molybdate–Molybdenum Trioxide Composites (M = Ni^{2+}, Cu^{2+} and Pb^{2+}). *Sens. Actuator B-Chem.* **101**, 353-360 (2004).

111. Yan, X. et al. Converting CoMoO$_4$ into CoO/MoO$_x$ for Overall Water Splitting by Hydrogenation. *ACS Sustain. Chem. Eng.* **4**, 3743-3749 (2016).

112. Hernández-Uresti, D.B., Martínez-de la Cruz, A. & Aguilar-Garib, J.A. Photocatalytic Activity of PbMoO$_4$ Molybdate Synthesized by Microwave Method. *Catal. Today* **212**, 70-74 (2013).

113. Kwolek, P. et al. Lead Molybdate - a Promising Material for Optoelectronics and Photocatalysis. *J. Mater. Chem. C* **3**, 2614-2623 (2015).

114. Kato, H., Matsudo, N. & Kudo, A. Photophysical and Photocatalytic Properties of Molybdates and Tungstates with a Scheelite Structure. *Chem. Lett.* **33**, 1216-1217 (2004).

115. Zhang, Y., Holzwarth, N.A.W. & Williams, R.T. Electronic Band Structures of the Scheelite Materials CaMoO$_4$, CaWO$_4$, PbMoO$_4$, and PbWO$_4$. *Phys. Rev. B* **57**, 12738-12750 (1998).

116. Groenink, J.A. & Blasse, G. Some New Observations on the Luminescence of PbMoO$_4$ and PbWO$_4$. *J. Solid State Chem.* **32**, 9-20 (1980).

117. Senguttuvan, N., Babu, S.M. & Subramanian, C. Synthesis, Crystal Growth and Mechanical Properties of Lead Molybdate. *Mater. Sci. Eng., B* **47**, 269-273 (1997).

118. Errandonea, D., Santamaria-Perez, D., Grover, V., Achary, S.N. & Tyagi, A.K. High-Pressure X-Ray Diffraction Study of Bulk and Nanocrystalline $PbMoO_4$. *J. Appl. Phys.* **108**, 073518 (2010).

119. Kudo, A. et al. Photoactivity of Ternary Lead-Group IV B Oxides for Hydrogen and Oxygen Evolution. *Catal. Lett.* **5**, 61-66 (1990).

120. Spassky, D.A. et al. Optical and Luminescent Properties of the Lead and Barium Molybdates. *Radiat. Meas.* **38**, 607-610 (2004).

121. Kunkel, K., Milke, E. & Binnewies, M. Formation of Ternary Lead-Molybdenum Oxides $PbMoO_4$, $PbMo_2O_7$, Pb_2MoO_5 and $PbMo_3O_{10}$ in the Gas Phase: A Mass Spectrometric and Quantum Chemical Investigation. *Int. J. Mass spectrom.* **374**, 12-19 (2014).

122. Dai, K. et al. Enhancing the Photocatalytic Activity of Lead Molybdate by Modifying with Fullerene. *J. Mol. Catal. A: Chem.* **374-375**, 111-117 (2013).

123. Du, W. et al. Black Lead Molybdate Nanoparticles: Facile Synthesis and Photocatalytic Properties Responding to Visible Light. *Appl. Surf. Sci.* **328**, 428-435 (2015).

124. Hernández-Uresti, D.B., Martínez-de la Cruz, A. & Torres-Martínez, L.M. Photocatalytic Properties of $PbMoO_4$ Synthesized by Co-Precipitation Method: Organic Dyes Degradation Under UV Irradiation. *Res. Chem. Intermed.* **38**, 817-828 (2012).

125. Martínez-de la Cruz, A., Hernández-Uresti, D.B., Torres-Martínez, L.M. & Lee, S.W. Photocatalytic Properties of $PbMoO_4$ synthesized by a Hydrothermal Reaction. *React. Kinet. Mech. Cat.* **107**, 467-475 (2012).

126. Zeng, H.C. Synthesis of stoichiometric lead molybdate $PbMoO_4$: An x-ray diffraction, Fourier transform infrared spectroscopy, and differential thermal analysis study. *J. Mater. Res.* **11**, 703-715 (2011).

127. Xing, G.-J. et al. Photoluminescence and photocatalytic properties of uniform $PbMoO_4$ polyhedral crystals synthesized by microemulsion-based solvothermal method. *Ceram. Int.* **37**, 2951-2956 (2011).

128. Zeng, H.C. Rectangular vacancy island formation and self-depletion in Czochralski-grown $PbMoO_4$ single crystal during heat treatment. *J. Cryst. Growth.* **160**, 119-128 (1996).

129. Kim, T.-H. et al. Synthesis of $TiO_{2-x}N_y$/Ag–$PbMoO_4$ nanocomposites: An effective approach for photoinactivation of green tide under simulated solar light. *Mater. Lett.* **101**, 99-102 (2013).

130. Phuruangrat, A., Thongtem, T. & Thongtem, S. Synthesis of lead molybdate and lead tungstate via microwave irradiation method. *J. Cryst. Growth.* **311**, 4076-4081 (2009).

131. Nicolosi, V., Chhowalla, M., Kanatzidis, M.G., Strano, M.S. & Coleman, J.N. Liquid Exfoliation of Layered Materials. *Science* **340** (2013).

132. Mayorga-Martinez, C.C., Sofer, Z. & Pumera, M. Layered Black Phosphorus as a Selective Vapor Sensor. *Angew. Chem. Int. Ed.* **54**, 14317-14320 (2015).

133. Mayorga-Martinez, C.C., Ambrosi, A., Eng, A.Y.S., Sofer, Z. & Pumera, M. Metallic 1T-WS_2 for Selective Impedimetric Vapor Sensing. *Adv. Funct. Mater.* **25**, 5611-5616 (2015).

134. Gautam, A., Kshirsagar, A., Biswas, R., Banerjee, S. & Khanna, P.K. Photodegradation of organic dyes based on anatase and rutile TiO_2 nanoparticles. *RSC Adv.* **6**, 2746-2759 (2016).

135. Syed, N. et al. Sonication-Assisted Synthesis of Gallium Oxide Suspensions Featuring Trap State Absorption: Test of Photochemistry. *Adv. Funct. Mater.* **27**, 1702295 (2017).

136. Dong, H. et al. An overview on limitations of TiO_2-based particles for photocatalytic degradation of organic pollutants and the corresponding countermeasures. *Water Res.* **79**, 128-146 (2015).

137. Syed, N. et al. Printing two-dimensional gallium phosphate out of liquid metal. *Nat. Commun.* **9**, 3618 (2018).

138. Carey, B.J. et al. Wafer-scale two-dimensional semiconductors from printed oxide skin of liquid metals. *Nat. Commun.* **8**, 14482 (2017).

139. Daeneke, T. et al. Wafer-Scale Synthesis of Semiconducting SnO Monolayers from Interfacial Oxide Layers of Metallic Liquid Tin. *ACS Nano* **11**, 10974-10983 (2017).

140. Daeneke, T. et al. Liquid metals: fundamentals and applications in chemistry. *Chem. Soc. Rev.* **47**, 4073-4111 (2018).

141. Dickey, M.D. et al. Eutectic Gallium-Indium (EGaIn): A Liquid Metal Alloy for the Formation of Stable Structures in Microchannels at Room Temperature. *Adv. Funct. Mater.* **18**, 1097-1104 (2008).

142. Kim, D. et al. Recovery of Nonwetting Characteristics by Surface Modification of Gallium-Based Liquid Metal Droplets Using Hydrochloric Acid Vapor. *ACS Appl. Mater. Interfaces* **5**, 179-185 (2013).

143. Preuß, A., Adolphi, B. & Wegener, T. The kinetic of the oxidation of InSn48. *Fresenius' J. Anal. Chem.* **353**, 399-402 (1995).

144. Nadaud, N., Lequeux, N., Nanot, M., Jové, J. & Roisnel, T. Structural Studies of Tin-Doped Indium Oxide (ITO) and $In_4Sn_3O_{12}$. *J. Solid State Chem.* **135**, 140-148 (1998).

145. Bierwagen, O. Indium oxide—a transparent, wide-band gap semiconductor for (opto)electronic applications. *Semicond. Sci. Technol.* **30**, 024001 (2015).

146. Dixon, S.C., Scanlon, D.O., Carmalt, C.J. & Parkin, I.P. n-Type doped transparent conducting binary oxides: an overview. *J. Mater. Chem. C* **4**, 6946-6961 (2016).

147. Zheng, Q. & Kim, J.-K. in Graphene for Transparent Conductors: Synthesis, Properties and Applications (eds. Zheng, Q. & Kim, J.-K.) 1-27 (Springer New York, New York, NY, 2015).

148. Lampert, C.M. Heat mirror coatings for energy conserving windows. *Sol. Energy Mater.* **6**, 1-41 (1981).

149. Lewis, B.G. & Paine, D.C. Applications and Processing of Transparent Conducting Oxides. *MRS Bull.* **25**, 22-27 (2000).

150. Greenham, N.C., Moratti, S.C., Bradley, D.D.C., Friend, R.H. & Holmes, A.B. Efficient light-emitting diodes based on polymers with high electron affinities. *Nature* **365**, 628 (1993).

151. Yu, Z. et al. Indium tin oxide as a semiconductor material in efficient p-type dye-sensitized solar cells. *NPG Asia Mater.* **8**, e305 (2016).

152. Guo, P., Schaller, R.D., Ketterson, J.B. & Chang, R.P.H. Ultrafast switching of tunable infrared plasmons in indium tin oxide nanorod arrays with large absolute amplitude. *Nat. Photonics* **10**, 267 (2016).

153. Naik, G.V., Shalaev, V.M. & Boltasseva, A. Alternative Plasmonic Materials: Beyond Gold and Silver. *Adv. Mater.* **25**, 3264-3294 (2013).

154. Alam, M.Z., De Leon, I. & Boyd, R.W. Large optical nonlinearity of indium tin oxide in its epsilon-near-zero region. *Science* **352**, 795 (2016).

155. Srinivasan, V., Pamula, V.K. & Fair, R.B. An integrated digital microfluidic lab-on-a-chip for clinical diagnostics on human physiological fluids. *Lab Chip* **4**, 310-315 (2004).

156. Bae, S. et al. Roll-to-roll production of 30-inch graphene films for transparent electrodes. *Nat. Nanotechnol.* **5**, 574 (2010).

157. Shigesato, Y., Takaki, S. & Haranou, T. Crystallinity and electrical properties of tin-doped indium oxide films deposited by DC magnetron sputtering. *Appl. Surf. Sci.* **48-49**, 269-275 (1991).

158. Tahar, R.B.H., Ban, T., Ohya, Y. & Takahashi, Y. Tin doped indium oxide thin films: Electrical properties. *J. Appl. Phys.* **83**, 2631-2645 (1998).

159. Wen, L., Sahu, B.B. & Han, J.G. Development and utility of a new 3-D magnetron source for high rate deposition of highly conductive ITO thin films near room temperature. *Phys. Chem. Chem. Phys.* **20**, 4818-4830 (2018).

160. Cairns, D.R. et al. Strain-dependent electrical resistance of tin-doped indium oxide on polymer substrates. *Appl. Phys. Lett.* **76**, 1425-1427 (2000).

161. Werner, T.T., Mudd, G.M. & Jowitt, S.M. Indium: key issues in assessing mineral resources and long-term supply from recycling. *Trans. Inst. Min. Metall., Sect. B* **124**, 213-226 (2015).

162. Wang, X., Zhi, L. & Müllen, K. Transparent, Conductive Graphene Electrodes for Dye-Sensitized Solar Cells. *Nano Lett.* **8**, 323-327 (2008).

163. Wu, Z. et al. Transparent, Conductive Carbon Nanotube Films. *Science* **305**, 1273-1276 (2004).

164. Hecht, D.S., Hu, L. & Irvin, G. Emerging Transparent Electrodes Based on Thin Films of Carbon Nanotubes, Graphene, and Metallic Nanostructures. *Adv. Mater.* **23**, 1482-1513 (2011).

165. Wu, H. et al. A transparent electrode based on a metal nanotrough network. *Nat. Nanotechnol.* **8**, 421 (2013).

166. Margulis, G.Y. et al. Spray Deposition of Silver Nanowire Electrodes for Semitransparent Solid-State Dye-Sensitized Solar Cells. *Adv. Energy Mater.* **3**, 1657-1663 (2013).

167. Morgenstern, F.S.F. et al. Ag-nanowire films coated with ZnO nanoparticles as a transparent electrode for solar cells. *Appl. Phys. Lett.* **99**, 183307 (2011).

168. Cao, C. et al. Nonlinear fracture toughness measurement and crack propagation resistance of functionalized graphene multilayers. *Sci. Adv.* **4**, eaao7202 (2018).

Chapter 3

Highly active two dimensional α-MoO$_{3-x}$ for the electrocatalytic hydrogen evolution reaction

3.1. Introduction

The development of earth-abundant electrocatalysts for the hydrogen evolution reaction (HER), with strong activity and stability, is of great interest in the field of clean energy research. The two dimensional (2D) morphology can significantly improve the HER activity by offering ultrathin structure with high surface area-to-volume ratios. Especially, if the aspect ratio of the individual nanosheets is moderate to low, the morphology can provide more catalytic edge sites for H$_2$ production.[1-3] In 2D nanosheets, a large number of exposed surface atoms are likely to escape from their respective lattice, which may produce vacancy-type defects.[4] Such vacancy defects, along with the associated structural disorder and edge sites can reduce the coordination number of surface atoms, producing dangling bonds and lead to higher catalytic activities in 2D nanosheets.[3, 4] Additionally, adding surface topological imperfections also enhance the catalytic activities. Catalytic reactions usually occur on the low coordinated steps, terraces, edges and kinks.[3, 5] In HER process, the adsorption

of water molecules usually occurs at a higher rate on the low coordinated active sites, which are abundant in the materials containing 2D morphologies.[3, 4]

Due to the layered crystal arrangement of orthorhombic α-MoO$_3$, this material can be exfoliated into 2D nanosheets, featuring a large surface area. Variations in the oxidation states of molybdenum facilitate crystal structure, morphology and oxygen vacancies tuning, making these oxide compounds suitable for electrochemical applications. Here, it is hypothesized that the combination of both oxygen deficient structure and 2D morphology can significantly activate the HER performance of molybdenum oxides. Molybdenum oxides have been shown to be easily formed into reduced 2D sheets.[6-8] Many reports are available demonstrating that electronic properties of 2D molybdenum oxides can be tuned by introducing oxygen deficiencies *via* various methods.[9-11] These features of 2D molybdenum oxides make them potentially more attractive for HER processes compared to many other 2D metal oxides. In this work, oxygen deficient 2D α-MoO$_{3-x}$ nanosheets (synthesized using liquid exfoliation method) is utilized to explore their HER performance in an alkaline condition. The facile preparation of ultrathin 2D nanosheets also allows for the formation of oxygen vacancies in the structure of high surface-to-volume ratio. The oxygen defects, surface steps and dislocations, and also edges of the 2D nanosheets are shown to significantly improve the electrocatalytic HER performance compared to the bulk form and fully stoichiometric α-MoO$_3$.

3.2. Methods

3.2.1. *Liquid phase exfoliation of molybdenum oxide nanosheets*

The exfoliation process of 2D molybdenum oxide nanosheets was adopted from a previously described procedure with slight modifications.[6, 8] In this work, 3 g of the

molybdenum oxide powder (99% purity, from China Rare Metal Material Co.) was ground with 0.6 ml ethanol for 30 mins. The powder was then dispersed into 45 ml ethanol solution, probe-sonicated (Ultrasonic Processor GEX500) for 60 mins at a power of 100 W, and centrifuged at 2500 rcf for 30 mins at room temperature, afterwards. Finally, the yellow/blue supernatant, containing a high concentration of 2D nanosheets, was collected.

3.2.2. Apparatus

Atomic force microscopy (AFM) measurements were recorded on a Bruker Dimension Icon AFM. X-ray photoelectron spectroscopy (XPS) was performed on a Thermo scientific K-Alpha instrument equipped with monochromated aluminium K- α source (1486.7 eV). 2D nanosheets suspension was used for ultraviolet-visible (UV-Vis) measurements. A Lambda 1050 UV/VIS/NIR Spectrometer (Perkin Elmer) equipped with a 150 mm InGaAs detector in the integrating sphere was utilised for this measurement. The solutions containing 2D nanosheets were drop cast onto Cu grids for high resolution transmission electron microscopy (HRTEM - JEOL 2100F) characterisations. Transmission electron microscopy (TEM) was conducted using JEOL 1010. Electron energy-loss spectroscopy (EELS) spectra were recorded using the scanning transmission electron microscopy (STEM) mode of JEOL 2100F. X-ray diffraction (XRD) patterns were collected using a Bruker D4 ENDEAVOR with monochromatic Cu K α as radiation source (λ= 0.154 nm). Raman spectroscopy was conducted using a 532 nm laser on a LabRAM HR Evolution Raman spectrometer (Horiba Scientific).

3.2.3. Electrochemical studies

HER catalytic activity tests were carried out in a standard three-electrode setup controlled by a CHI 760D (CH Instrument Co.) workstation. The cell setup contained a working electrode (nickel foam) coated with the samples (2D nanosheets), an Ag/AgCl (in 1 M KCl, aq) reference electrode, a graphite rod counter electrode and 0.1 M KOH solution as the electrolyte. The reference electrode was calibrated against and converted to a reversible hydrogen electrode (RHE). Linear sweep voltammetry was performed at 5 mVs^{-1} scan rate for the polarization curves. All polarization curves were iR-corrected. The solution deposited on the working electrode was prepared as follows: 100 mg of carbon powder was dispersed in a mixture of deionised (DI) water and isopropanol (IPA) (40 mL: 10 mL). Thereafter, 5 mg of each catalyst (bulk and 2D α-MoO$_{3-x}$) was mixed with 2.5 mL of the as prepared carbon solution and sonicated for 5 mins, followed by adding 10 µL of polytetrafluoroethylene solution (60% in water, Sigma) and sonication for 5 mins to form a suspension. Finally, 100 µL of a suspension was drop-casted onto 0.25 cm^2 area of Ni foam using a micropipette. HER measurement on bare Ni foam was also performed using 0.25 cm^2 geometric area.[12-14]

The 2D nanosheets and bulk sample were further utilized in the cyclic voltammetry (CV) measurements in the same electrochemical cell to determine the electrochemical double-layer capacitance (EDLC) of both the materials. The CV measurements were performed over a range of scan rates at 0.45 V versus RHE in 0.1M KOH.

3.3. Results and discussions

2D nanosheets were prepared following the procedure described in the Methods section, during which the bulk crystals were ground in ethanol followed by high power

ultrasonication, facilitating mechanical liquid phase exfoliation. Ethanol was used as the solvent due to its favourable Hansen solubility parameters (HSP) with respect to bulk α-MoO$_3$ which facilitates the efficient exfoliation into 2D nanosheets.[8] The suspension has a yellow/blue colour (**Figure** 3.1). As previously shown, the well-matched properties of the chosen solvent and surface energy of molybdenum oxide allow a stable colloidal suspension after exfoliation.[8, 15, 16]

A series of characterisations were applied to assess the 2D structural features and crystal properties of the as synthesized nanosheets. Furthermore, these nanosheets were incorporated into a three-electrode based electrochemical system to evaluate their potentials in electrocatalytic HER as presented in detail in the Methods section.
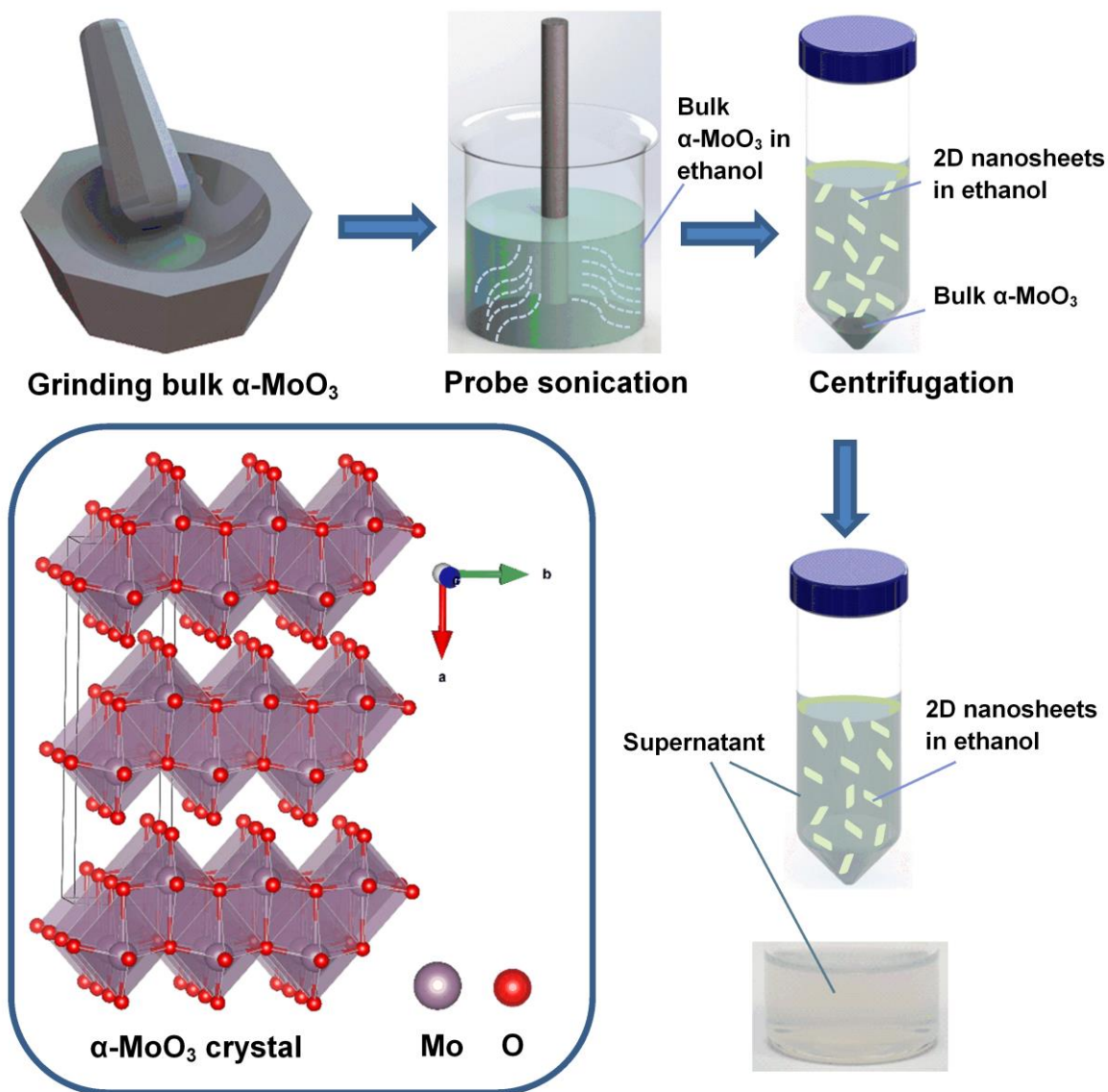
Figure 3.1. A schematic diagram describing the step-by-step synthesis process from bulk α-MoO$_3$ to 2D nanosheets.

The surface morphology and thicknesses of the 2D nanosheets were investigated using AFM. The AFM analysis revealed that exfoliated 2D nanosheets have the average thickness of T_{av} = 4.4 nm (**Figure** 3.2a), which corresponds to ~6 fundamental layers of α-MoO$_3$ (0.7 nm is the monolayer thickness).[17] It is also evident from the AFM characterisation that the exfoliated 2D nanosheets possess step-rich basal surfaces

(**Figure** 3.2b), which result in the increase of dangling bonds and active sites. AFM also showed that the nanosheets had the average lateral sizes of L_{av} = 125 nm (**Figure** 3.3a), which is also in good agreement with the TEM images (see **Figure** 3.3b, c). These values lead to a 2D nanosheet aspect ratio (L_{av} / T_{av}) of ~28, which is comparable with the previously reported values obtained for the exfoliated 2D molybdenum oxide nanosheets.[8]
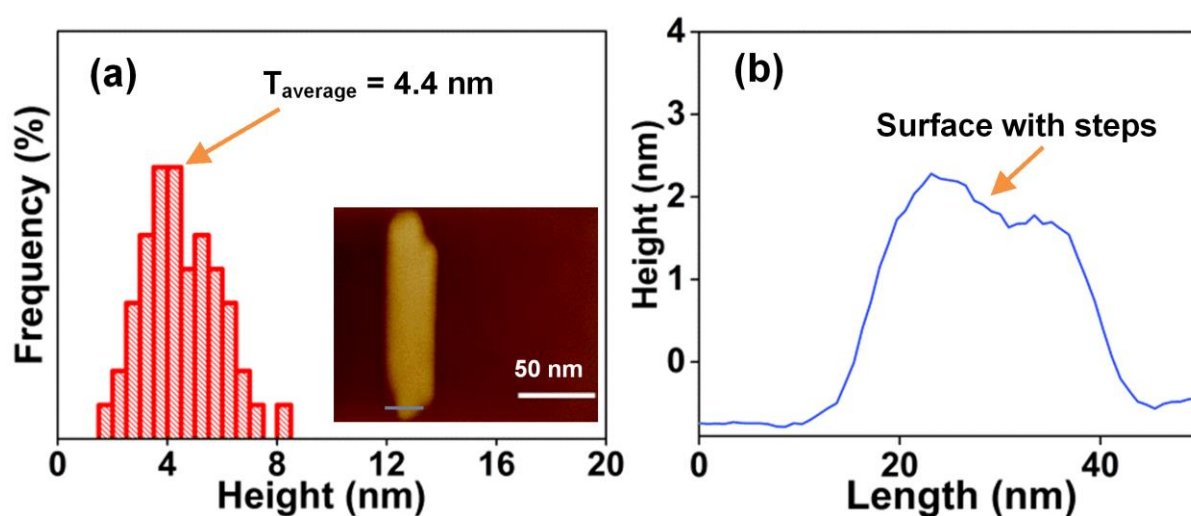
Figure 3.2.   AFM characterisation of 2D nanosheets (a) frequency histogram of the observed thickness of the 2D nanosheets, AFM image of the nanosheet (inset), and (b) corresponding thickness profile.
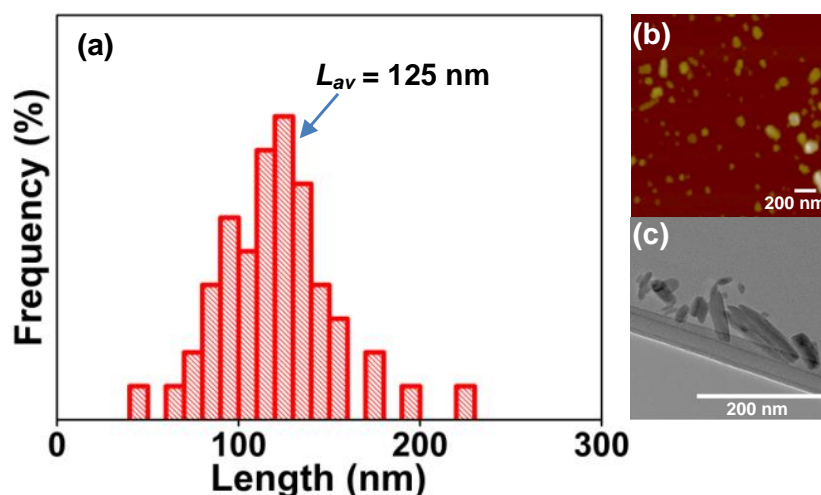
Figure 3.3. (a) Frequency histogram of the observed lateral sizes of 2D MoO_{3-x} nanosheets using AFM, (b) large area AFM image of 2D MoO_{3-x} nanosheets, and (c) large area TEM image showing the 2D MoO_{3-x} nanosheets.

XPS was utilized to investigate any changes to the oxidation states and binding energies of the material due to the exfoliation process with reference to the bulk precursor powder. The XPS spectra of the Mo 3d region are presented in **Figure** 3.4. For the bulk α-MoO_3, the doublets at 236.4 and 233.3 eV are ascribed to the binding energies of the Mo $3d_{3/2}$ and Mo $3d_{5/2}$ orbital electrons of Mo^{6+}, respectively (**Figure** 3.4a).[18] Upon the formation of exfoliated 2D nanosheets, two new peaks of Mo 3d XPS appear at the lower binding energies of 235.1 and 232.0 eV, belonging to Mo^{5+} oxidation state (see **Figure** 3.4b).[9, 19] The emergence of Mo^{5+} oxidation state is associated with the presence of oxygen vacancies in the 2D nanosheets and therefore, the structure can be referred to as 2D α-MoO_{3-x}.[20] During the formation of oxygen deficient structure, the Mo^{6+} neighbouring the oxygen vacancy in the α-MoO_3 lattice is reduced to Mo^{5+}, donating an electron to the conduction band.[9, 21] This donated electron is delocalized within the layers and acts as a Drude-model like free electron,[21] therefore, altering the electronic configuration of the α-MoO_3.[9, 21] The presence of

oxygen vacancy is also evident in the O 1s spectra, where the intense peak attributed to lattice oxygen (O^{2-}) shifts to a lower binding energy for the 2D α-MoO$_{3-x}$ with reference to the bulk α-MoO$_3$ (**Figure** 3.4c, d).[22] Considering the integral areas of Mo^{6+} and Mo^{5+} peaks, the value of x in 2D MoO$_{3-x}$ is determined ~ 0.045.
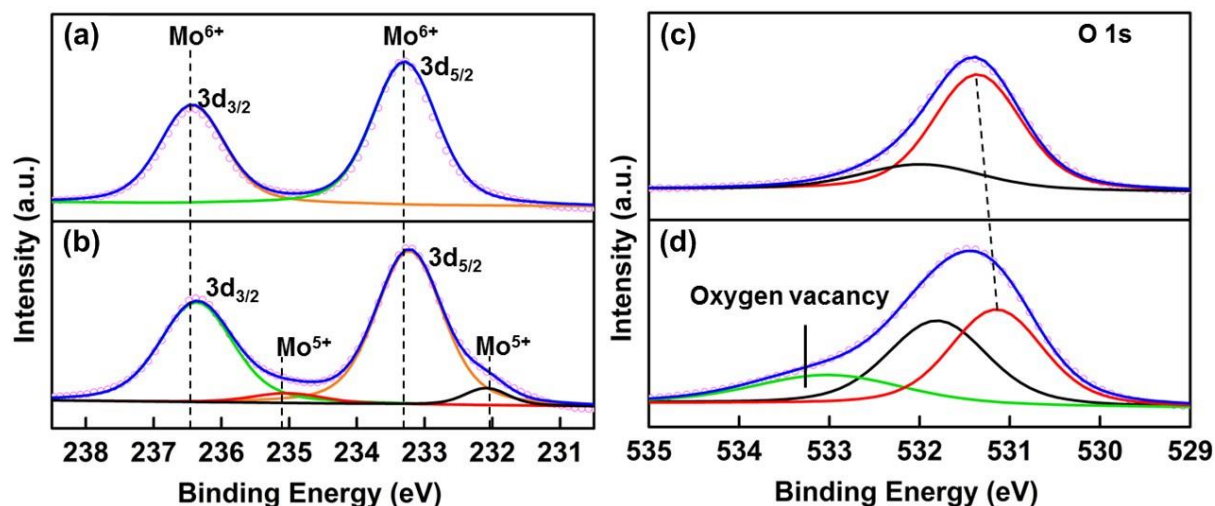
Figure 3.4. Mo 3d XPS spectra of (a) bulk α-MoO$_3$ and (b) 2D α-MoO$_{3-x}$, and O 1s XPS spectra of (c) bulk α-MoO$_3$ and (d) 2D α-MoO$_{3-x}$.

The changes in electronic configuration of the exfoliated 2D nanosheets were further investigated using the XPS valence band spectra, UV-vis spectroscopy and Tauc plot analysis. For bulk α-MoO$_3$, the distance between valence band edge and Fermi level (E_f) is ~3 eV, which suggests its *n*-type feature (**Figure** 3.5a).[23] Interestingly, due to the presence of oxygen vacancies in the 2D α-MoO$_{3-x}$ nanosheets, a newly occupied state appears between the E_f and valence band edge energy levels. This defect state (indicated in the **Figure** 3.5a) appears due to the removal of O^{2-} ions from the valence band spectra of 2D α-MoO$_{3-x}$.[11] In order to maintain the charge neutrality, the Mo^{6+} state reduces to Mo^{5+} indicating a slight semiconducting-to-metallic transformation.[6, 11] Consequently, the previously empty 4*d* band of molybdenum oxide becomes

partially filled with electrons, giving rise to the defect state observed in the valence band spectra ~1.4 eV below E_f.[8, 9] In order to analyse the bandgap energy of the 2D nanosheets, the integrating sphere supported UV-Vis spectroscopy was conducted. It has been reported that 2D α-MoO$_{3-x}$ features an indirect bandgap[24] and here the Tauc plot (**Figure** 3.5b) based on the UV-Vis data reveals that the bandgap of this material is ~2.9 eV. The narrow bandgap energy of the 2D α-MoO$_{3-x}$ compared to the pristine molybdenum oxide (~3.2 eV)[10] refers to the presence of defect and enhanced electrical conduction in the reduced 2D nanosheets.[6]
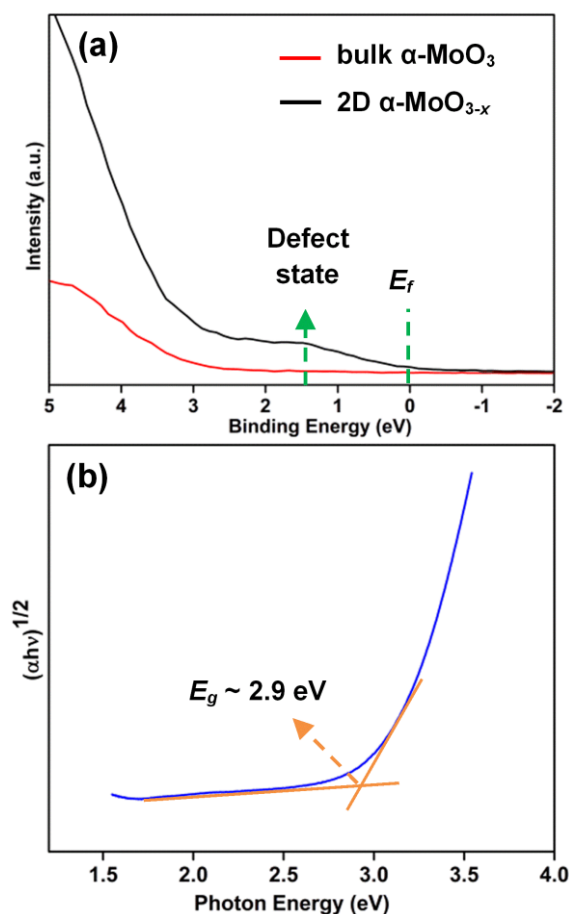
Figure 3.5. (a) The XPS valence graphs of bulk α-MoO$_3$ and 2D α-MoO$_{3-x}$ and (b) Tauc-plot of 2D α-MoO$_{3-x}$.

The HRTEM was utilized in order to investigate the lattice arrangement of the 2D α-MoO$_{3-x}$ nanosheets. The lattice fringes of the 2D nanosheets exhibit a spacing of 0.39 nm representing (1 0 0) plane of orthorhombic α-MoO$_3$ (see **Figure** 3.6a), and in agreement with the previously reported oxygen deficient α-MoO$_{3-x}$ structure.[6, 9] Interestingly, many distortions and dislocations can be observed in the lattice fringes of the 2D nanosheets, which suggest a defect-rich structure. The slightly reduced average lattice spacing of 0.36 nm can also be a sign of surface defects. This has generally been attributed to the presence of oxygen vacancies in the structure.[6] Careful observation of the HRTEM images reveals that the surface defects are widely available on the surface. Additionally, the edges of the nanosheets are rough that also contribute to the presence of more corner and edge defects and dangling bonds (**Figure** 3.6a, b). The corresponding fast Fourier transform (FFT) patterns also revealed the (0 0 1) and (0 0 2) planes, which are also associated with the orthorhombic crystal structure of α-MoO$_3$ and in agreement with the previously reported literatures.[6, 25] In order to obtain further insight on the oxygen vacancies, EELS spectra were recorded in a scanning transmission electron microscopy (STEM) microscope. Precise chemical information on molybdenum oxides can be extracted from the oxygen-K (O-K) edges obtained using EELS spectra.[26] The O-K prepeak for the 2D α-MoO$_{3-x}$ nanosheet is situated at 533.1 eV, which is at higher energy compared to the prepeak of bulk α-MoO$_3$ at 532.3 eV (**Figure** 3.6c). Shift to the higher energy suggests a lower oxidation state of the Mo metal linked to the oxygen atoms.[27] This indicates the presence of oxygen vacancies in the 2D α-MoO$_{3-x}$ nanosheets, rather than a phase transformation.[27]
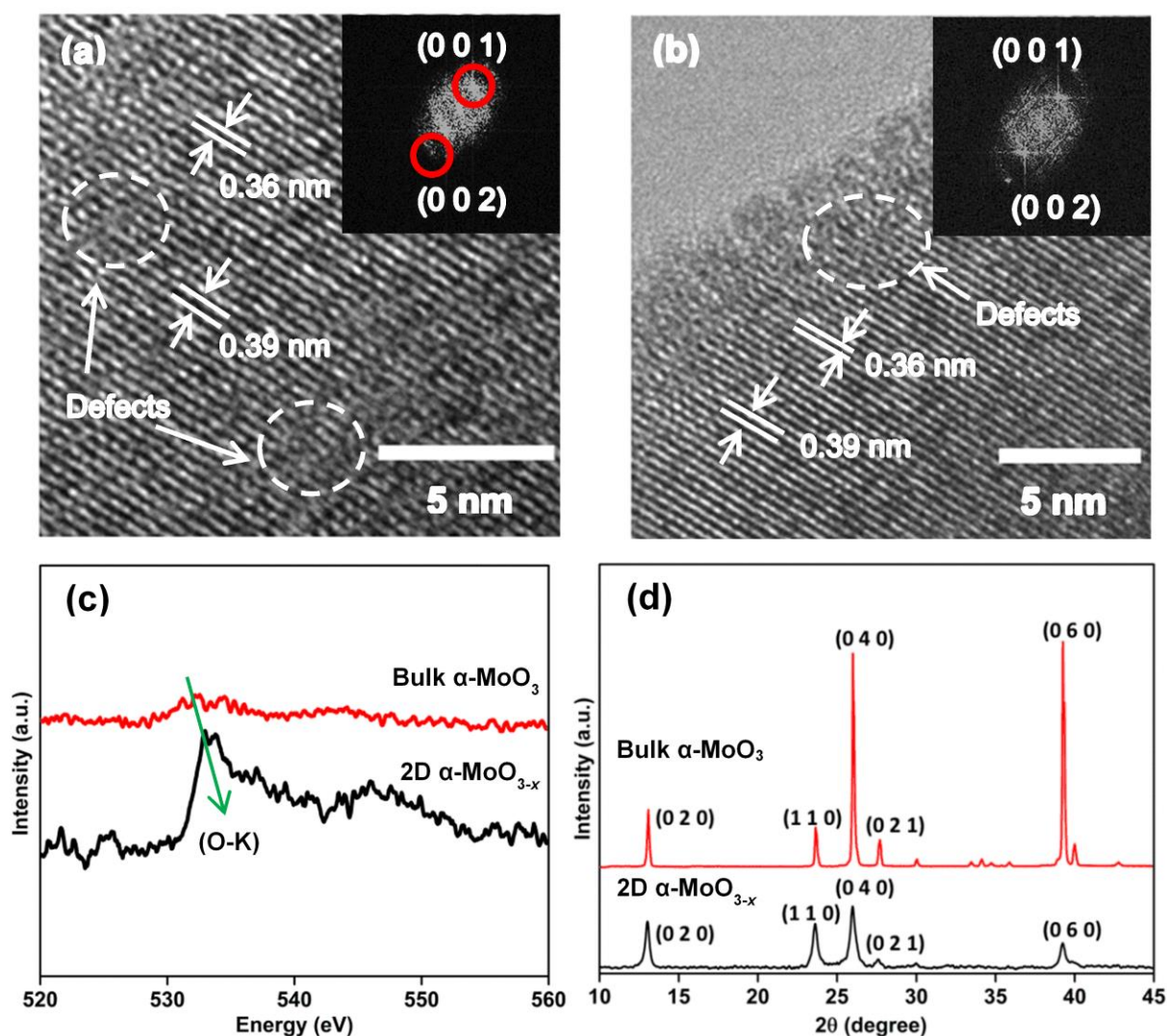
Figure 3.6. (a) HRTEM image of the surface of 2D α-MoO$_{3-x}$ nanosheets with FFT image (inset) showing the highlighted characteristic diffraction spots, (b) HRTEM image of the edge of 2D α-MoO$_{3-x}$ nanosheets with FFT image (inset) showing the highlighted characteristic diffraction spots, (c) EELS core-loss spectra of bulk α-MoO$_3$ and 2D α-MoO$_{3-x}$ nanosheet showing the O-K edge. The green arrow highlights the shift to a higher energy. All the spectra were adjusted to the zero-loss peak, and (d) XRD patterns of bulk α-MoO$_3$ and 2D α-MoO$_{3-x}$.

XRD patterns of the 2D α-MoO$_{3-x}$ nanosheets deposited on glass substrates were analyzed in order to understand any changes in the crystal structure during the

synthesis of 2D α-MoO$_{3-x}$. Bulk α-MoO$_3$ was also characterized for comparison and referencing. Using XRD patterns, both bulk and 2D α-MoO$_{3-x}$ can be indexed to the thermodynamically stable orthorhombic (α-MoO$_3$) crystal structure with lattice parameters of a = 3.962 Å, b = 13.858 Å, c = 3.697 Å (JCPDs, no. 05-0508).[25] For the 2D α-MoO$_{3-x}$, the most intense diffraction peaks are associated with the (0 2 0), (1 1 0), (0 4 0), (0 2 1) and (0 6 0) planes, respectively (see **Figure** 3.6d) which are in agreement with peaks of previously reported XRD patterns for α-MoO$_{3-x}$ crystals.[25, 28] The XRD patterns in **Figure** 3.6d show that the most intense planes (020), (040) and (0 6 0), which attribute to the b-lattice plane interlayers, are shifted to slightly lower angles (0.06°, 0.02° and 0.02°, respectively) in 2D α-MoO$_{3-x}$ nanosheets with conspicuous broadening of the peaks compared to the bulk α-MoO$_3$. This suggests that the oxygen vacancy occurred in the crystal lattice of 2D α-MoO$_{3-x}$ nanosheets, which is attributed to a vacancy at the terminal oxygen (O$_t$) site with two accompanying Mo^{5+} ions.[28]

The samples were then characterized using Raman spectroscopy to investigate their vibrational signatures. Raman spectroscopy was conducted at 532 nm excitation with 0.9 mW laser power and samples were placed on gold coated substrates. In both Raman spectra of bulk MoO$_3$ and 2D α-MoO$_{3-x}$ strong peaks at the 282, 665, 821, and 997 cm^{-1} are seen, which are all in agreement with previously reported peak positions of orthorhombic molybdenum oxide (see **Figure** 3.7).[6, 29] The 282 cm^{-1} peak is related to the bending mode for the double bond (Mo=O) vibration and the peak at 665 cm^{-1} is correlated to tri-coordinated oxygen (Mo$_3$–O) stretching mode.[6] The 821 cm^{-1} peak is attributed to the bi-coordinated oxygen (Mo$_2$–O) stretching mode, while The 997 cm^{-1} peak represents the terminal oxygen (Mo^{6+}=O) stretching mode of α-MoO$_{3-x}$ structure.[20, 29] Additionally, the Raman peaks at lower wavenumbers of 336 and 375

cm^{-1} can be assigned to the bending and scissoring modes of O–Mo–O, respectively.[29] For 2D α-MoO$_{3-x}$ these peaks at lower wavenumbers were observed to become weaker compared to the bulk α-MoO$_3$ due to the formation of thinner nanosheets (**Figure** 3.7).[7] Confirming the presence of oxygen vacancies after exfoliation, the newly emerged 489 and 890 cm^{-1} peaks can be assigned to Mo=O stretching and Mo$_2$–O stretching modes of MoO$_{3-x}$, respectively (**Figure** 3.7b).[30, 31]
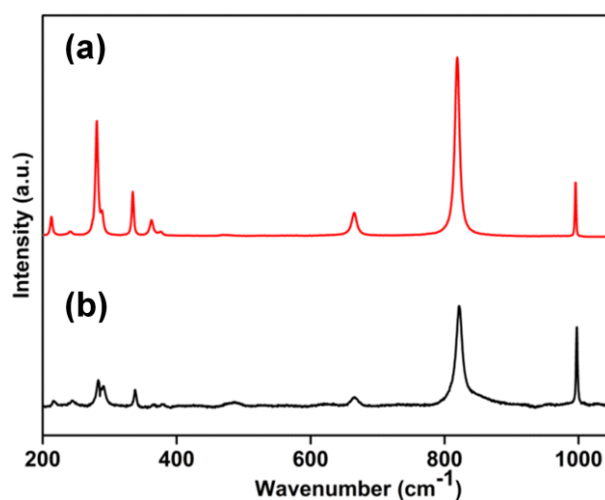
Figure 3.7.   Raman spectra of (a) bulk α-MoO$_3$ and (b) 2D α-MoO$_{3-x}$.

In this work, the electrocatalytic HER activities of the as-synthesized 2D α-MoO$_{3-x}$ nanosheets were examined in alkaline (0.1 M KOH) solutions. Due to the high solubility and inferior electrocatalytic performance of molybdenum oxides in acids,[32, 33] this work is focused on alkaline media. All materials were deposited onto 3D porous nickel (Ni) foam (as described in the Methods section), which is commonly used and provides a large surface area as the working electrode.[34] For comparison, bulk α-MoO$_3$ and bare Ni foam electrodes were also tested under identical conditions. **Figure** 3.8a shows the HER polarization curves of various electrocatalysts in 0.1 M KOH solutions. For the 2D α-MoO$_{3-x}$, an overpotential value of 142 mV was required to

achieve standard 10 mA cm^{-2} HER current density. On the other hand, bare Ni foam and bulk α-MoO$_3$ exhibited a much larger required overpotential values of 265 mV and 220 mV, respectively.

For comparison, Tafel plots were derived using the polarization graphs (**Figure** 3.8b) to investigate the kinetics of their HER performances and determine the predominant HER mechanism.[35, 36] The smaller value of Tafel slope indicates the faster HER rate for an electrocatalyst. A Tafel slope of 58 mVdec^{-1} was observed for the 2D α-MoO$_{3-x}$ nanosheets, which is much smaller than the value obtained for bulk α-MoO$_3$ (122 mVdec^{-1}) and bare Ni foam electrode (115 mVdec^{-1}). The lower Tafel slope value of 2D α-MoO$_{3-x}$ nanosheets suggests a fast HER rate *via* the Volmer–Heyrovsky process (step 1: $H_2O_{(liquid)}+e^- \leftrightarrow H_{(adsorption)}+OH^-$ and step 2: $H_{(adsorption)}+H_2O_{(liquid)}+e^- \leftrightarrow H_{2(gas)}+OH^-$), similar to the previously reported HER in TMOs.[37] With a Tafel slope close (or larger) to 116 mV dec^{-1}, the HER rate can be defined as a slow discharge reaction *via* the Volmer-Heyrovsky process,[36] such as the Tafel slope of bulk α-MoO$_3$ measured in this work.
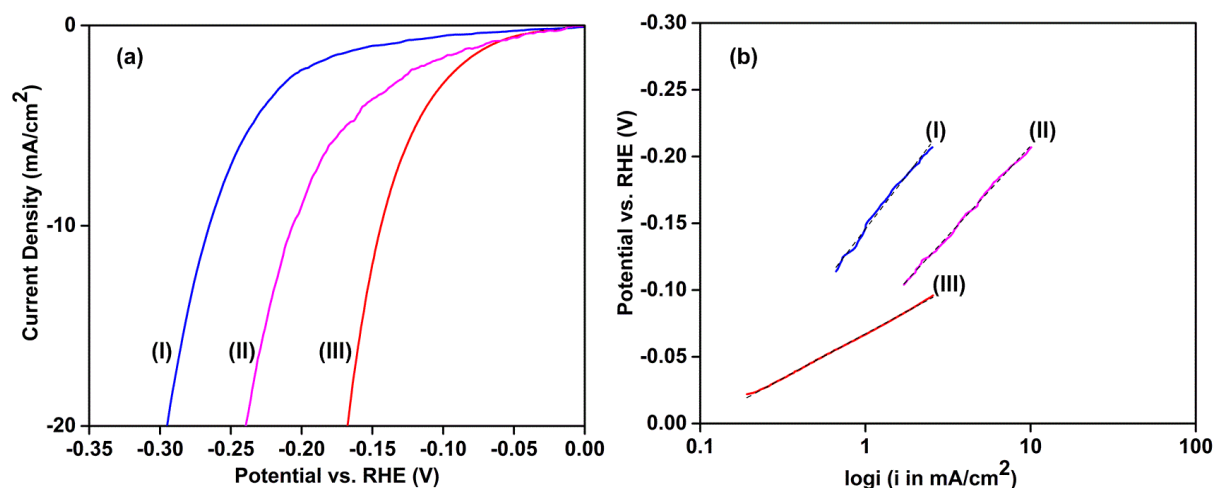
Figure 3.8. (a) Linear sweep voltammogram of HER on (I) bare Ni foam, (II) bulk α-MoO$_3$, (III) 2D α-MoO$_{3-x}$, and (b) Tafel plots of (I) bare Ni foam, (II) bulk α-MoO$_3$, (III) 2D α-MoO$_{3-x}$ in 0.1 M KOH.

In addition, the 2D α-MoO$_{3-x}$ exhibited excellent durability after 1000 cycles of cyclic voltammetry, where no obvious loss of activity was observed (see **Figure** 3.9a). The long-term HER performance of 2D α-MoO$_{3-x}$ nanosheets (annealed at 200°C, this annealing temperature does not change the stoichiometry but instead stabilises the flakes on the surface) also showed negligible loss under a static overpotential (**Figure** 3.9c). This suggests that negligible corrosion of electrocatalyst occurred in the basic electrolyte (0.1 M KOH) and features a robust stability of the 2D α-MoO$_{3-x}$ nanosheets.
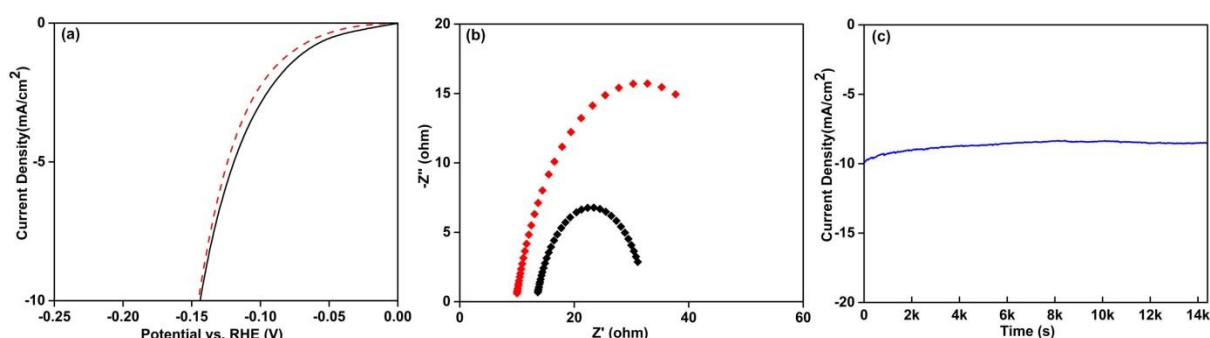
Figure 3.9.   (a) Linear sweep voltammogram recorded for 2D α-MoO$_{3-x}$ before and after 1000 cycles of cyclic voltammetry, (b) fitted Nyquist plot of bulk α-MoO$_3$ (red symbol) and 2D α-MoO$_{3-x}$ (black symbol) at 0.17V vs. RHE, and (c) time-dependent current density of 2D α-MoO$_{3-x}$ nanosheets during HER with 14.4k seconds at fixed overpotential of 0.14 V vs RHE.

In order to gain information about the active sites of MoO$_{3-x}$ as an electrocatalyst EDLC characterization was conducted. To determine the EDLC of 2D α-MoO$_{3-x}$ and bulk α-MoO$_3$, CV was performed in the similar electrochemical cell that was utilized

for HER tests. As can be seen in **Figure** 3.10, the geometric current density at 0.45 V *vs* RHE in 0.1M KOH (where no Faraday process occurs) is plotted against the scan rates of the CV. The EDLC values were determined from the slopes of the linear regression.[38] A larger EDLC value of 14.71 mFcm^{-2} was obtained for the 2D α-MoO$_{3-x}$ compared to the value of 11.41 mFcm^{-2} measured for bulk α-MoO$_3$. This comparative analysis suggests that the 2D α-MoO$_{3-x}$ possesses a much higher active surface area compared to bulk α-MoO$_3$ for enhanced HER activity.
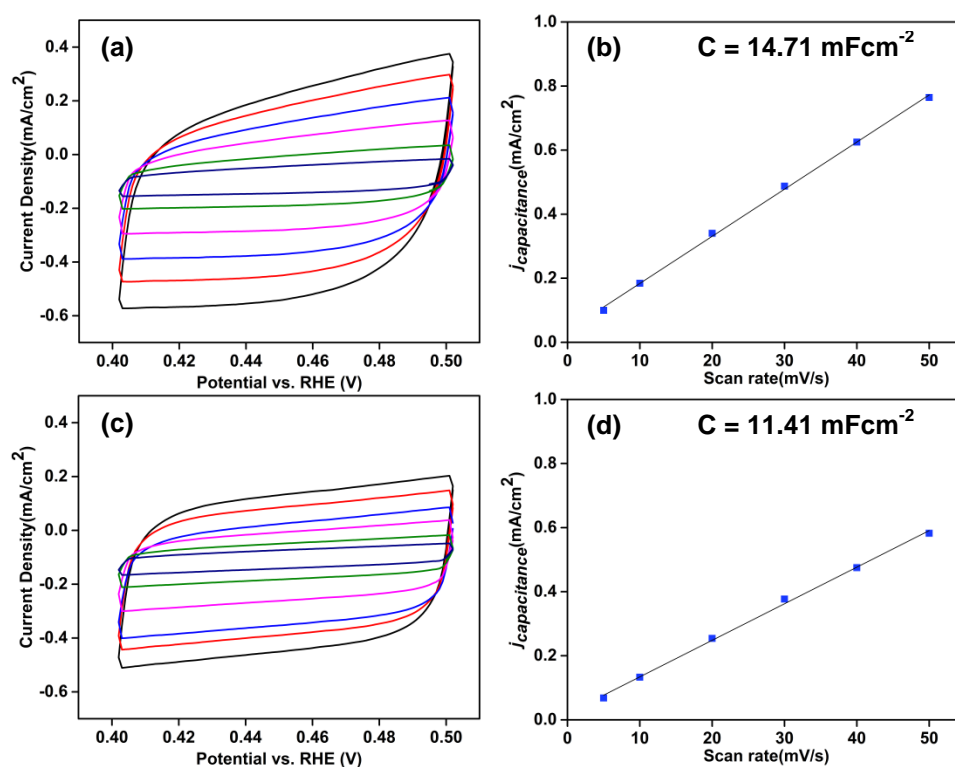
Figure 3.10. (a, b) Determination of electrochemical double-layer capacitance of 2D α-MoO$_{3-x}$ nanosheets over a range of scan rates at 0.45 V vs RHE in 0.1M KOH and (c, d) determination of electrochemical double-layer capacitance of bulk α-MoO$_3$ over a range of scan rates at 0.45 V vs RHE in 0.1M KOH.

Structural defects have been identified as an important factor to enhance the HER activity, leading to the emergence of additional active sites within the basal surface of 2D MoO_{3-x}.[3] Such structural defects were identified using HRTEM as seen in **Figure** 3.6a. Additionally, the defective edges of nanosheets (evident in the HRTEM images, **Figure** 3.6b) and steps of the basal surface also contribute to such metallic ends (steps shown in AFM characterisation, **Figure** 3.2b).[3, 4, 39] Defects such as oxygen vacancies can significantly enhance the HER performance of a catalyst, due to the formation of dangling bonds.[22] In this work, the presence of oxygen vacancies (that were revealed using EELS assessments) in the 2D nanosheets enhances the interaction between oxygen-containing species and metal oxide surfaces. The oxygen deficient 2D α-MoO_{3-x} may also favour the adsorption of hydrogen atoms (H_{ads}) and water molecules, which serve as electron acceptors.[22] This can significantly lower the HER energy barrier and promote the HER activity.[40]

Another property that plays a significant role to improve the HER activity is the 2D structure with large surface-to-volume ratios.[1, 41] The 2D α-MoO_{3-x} nanosheets provide more electrochemically active surface area compared to the bulk α-MoO_3 (see **Figure** 3.10). The ultrathin flat facet in 2D α-MoO_{3-x} nanosheets can provide large number of low coordinated active sites, which may further improve the adsorption of water molecules.[3] In addition, the oxygen deficient 2D α-MoO_{3-x} nanosheets are more likely to possess improved ion conductivity and exhibit fast charge transfer compared to the bulk α-MoO_3.[22] This is also evident from the electrochemical impedance spectroscopy (EIS) measurements, where the 2D α-MoO_{3-x} indicated a much lower charge transfer resistance (19.3 Ω) compared to the bulk α-MoO_3 (43.7 Ω) (see **Figure** 3.9b and **Table** 3.1).
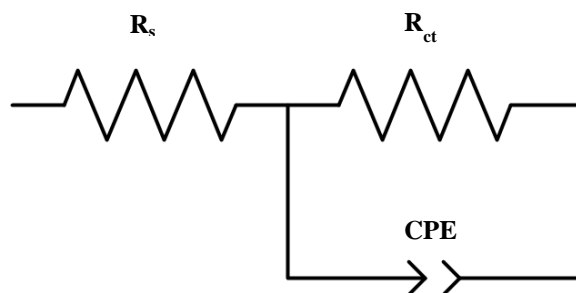
Figure 3.11. Equivalent circuit applied to obtain charge transfer resistance of the catalysts in 0.1 M KOH.

Here,

R_s: resistance of the electrolyte

R_{ct}: charge transfer resistance

CPE: constant phase element

Table 3.1. Impedance components for HER determined by fitting the experimental EIS data using the equivalent circuit shown in **Figure** 3.11.

Material	$R_s(\Omega)$	$R_{ct}(\Omega/cm^2)$
2D α-MoO₃₋ₓ	13.3	19.3
Bulk α-MoO₃	9.7	43.7

A comparison with previously reported HER activities related to molybdenum oxides, their compounds and heterostructures as well as selected reports on two dimensional molybdenum sulphides are summarized in **Figure** 3.12, which indicates the importance superiority of oxygen deficient 2D structure in HER.[22, 39, 42-45] A recent work using mesoporous MoO_{3-x}, reported a low overpotential value of 138 mV at 10 mAcm^{-2} HER current density, however, a careful analysis of the HER polarization

curves in this published work revealed that the actual value is ~148 mV (this is included in **Figure** 3.12).[46] In addition, the synthesis process of mesoporous MoO_{3-x} requires ~4 days, where the synthesis of 2D MoO_{3-x} requires only 2 hours. Preparation of surfactant, precursors, and template removal process also increase the complexity for synthesising mesoporous MoO_{3-x}. These also leave a concern regarding the purity of the MoO_{3-x} structure (due to contradictory representation of the XPS and Raman spectra in the reported work) as the effect of residues may reflect on their HER overpotential and deteriorate the stability.[46] As can also be seen, the 2D MoO_{3-x} has a lower HER overpotential voltage in comparison to 1T or highly defected 2D MoS_2,[39, 42] which presents the superiority of the oxide of molybdenum in evaluated against dichalcogenide compounds of molybdenum.
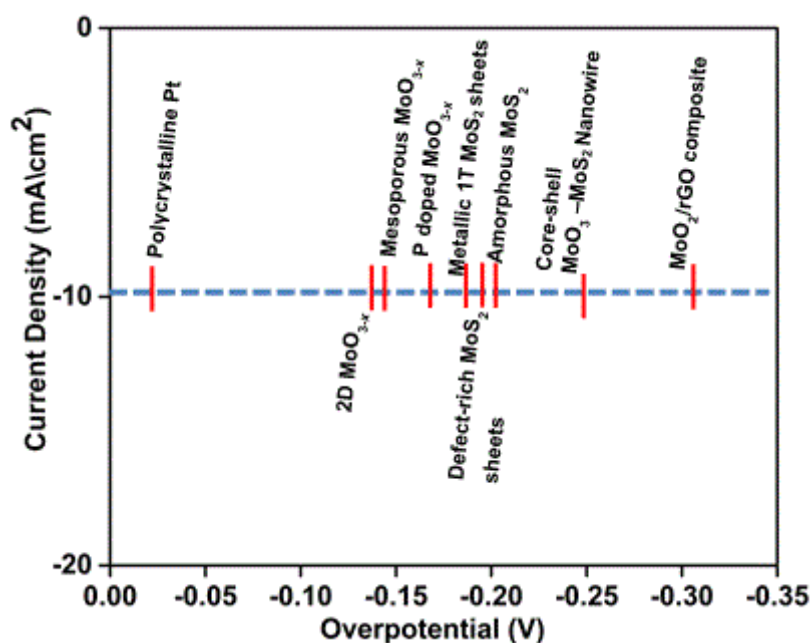
Figure 3.12. Comparison of the overpotentials of molybdenum oxides and disulphides, their compounds and heterostructures at 10 mA/cm^2 current density, including polycrystalline Pt[47], mesoporous MoO_{3-x}[46], P doped MoO_{3-x}[22], metallic 1T MoS_2 sheets[42], defect-rich MoS_2 sheets[39], amorphous MoS_2[45], core–shell MoO_3–MoS_2 nanowires[43], MoO_2/rGO composite[44].

3.4. Conclusions

In summary, the presented study illustrates a facile and reproducible strategy to synthesise oxygen deficient 2D nanosheets molybdenum oxides from stratified bulk α-MoO_3. The efficient performance of these nanosheets for electrocatalytic HER was then shown. The sheets on average made of 6 fundamental layers of molybdenum oxides and lateral dimensions of ~125 nm, leading to an aspect ratio of ~28. Elemental analysis revealed the formation of oxygen vacancies in the 2D α-MoO_{3-x} nanosheets. Structural and vibrational analyses showed highly ordered planar structure of the synthesized 2D nanosheets. In alkaline media, the 2D α-MoO_{3-x} nanosheets exhibited a considerable HER performance with the low overpotential value of 142 mV (achieved at standard 10 $mAcm^{-2}$ current density). The key factors affecting HER activity were shown to be the combination of oxygen deficient structure and large surface area of 2D feature of the synthesized nanosheets with structural defects and steps, which significantly augmented the density of catalytic sites for efficient HER.

This finding constitutes the first system in which 2D α-MoO_{3-x} nanosheets were utilized in electrocatalytic HER. The oxygen vacancies in 2D α-MoO_{3-x} nanosheets can be fine-tuned using different methods such as controlled solar or UV light irradiation, which has been demonstrated previously.[6, 19] The synthesis approach, with controlled tuning of oxygen vacancies, could be suitable for designing and the exfoliation of other layered transition metal oxides for HER or other electrochemical applications.

3.5. References

1. Wang, H. et al. Electrochemical Tuning of MoS_2 Nanoparticles on Three-Dimensional Substrate for Efficient Hydrogen Evolution. *ACS Nano* **8**, 4940-4947 (2014).

2. Pandey, M., Vojvodic, A., Thygesen, K.S. & Jacobsen, K.W. Two-Dimensional Metal Dichalcogenides and Oxides for Hydrogen Evolution: A Computational Screening Approach. *J. Phys. Chem. Lett.* **6**, 1577-1585 (2015).

3. Sun, Y., Gao, S., Lei, F. & Xie, Y. Atomically-thin two-dimensional sheets for understanding active sites in catalysis. *Chem. Soc. Rev.* **44**, 623-636 (2015).

4. Tao, H. et al. Two-dimensional nanosheets for electrocatalysis in energy generation and conversion. *J. Mater. Chem. A* **5**, 7257-7284 (2017).

5. Lim, C.S., Tan, S.M., Sofer, Z. & Pumera, M. Impact Electrochemistry of Layered Transition Metal Dichalcogenides. *ACS Nano* **9**, 8474-8483 (2015).

6. Alsaif, M.M.Y.A. et al. Tunable Plasmon Resonances in Two-Dimensional Molybdenum Oxide Nanoflakes. *Adv. Mater.* **26**, 3931-3937 (2014).

7. Ji, F. et al. $2D-MoO_3$ nanosheets for superior gas sensors. *Nanoscale* **8**, 8696-8703 (2016).

8. Alsaif, M.M.Y.A. et al. Exfoliation Solvent Dependent Plasmon Resonances in Two-Dimensional Sub-Stoichiometric Molybdenum Oxide Nanoflakes. *ACS Appl. Mater. Interfaces* **8**, 3482-3493 (2016).

9. Alsaif, M.M.Y.A. et al. High-Performance Field Effect Transistors Using Electronic Inks of 2D Molybdenum Oxide Nanoflakes. *Adv. Funct. Mater.* **26**, 91-100 (2016).

10. Huang, Q., Hu, S., Zhuang, J. & Wang, X. MoO_{3-x}-Based Hybrids with Tunable Localized Surface Plasmon Resonances: Chemical Oxidation Driving Transformation from Ultrathin Nanosheets to Nanotubes. *Chem. Eur. J.* **18**, 15283-15287 (2012).

11. Greiner, M.T., Chai, L., Helander, M.G., Tang, W.-M. & Lu, Z.-H. Transition Metal Oxide Work Functions: The Influence of Cation Oxidation State and Oxygen Vacancies. *Adv. Funct. Mater.* **22**, 4557-4568 (2012).

12. Ding, J., Zhou, Y., Li, Y., Guo, S. & Huang, X. MoS_2 Nanosheet Assembling Superstructure with a Three-Dimensional Ion Accessible Site: A New Class of Bifunctional Materials for Batteries and Electrocatalysis. *Chem. Mater.* **28**, 2074-2080 (2016).

13. Miao, R. et al. Mesoporous Iron Sulfide for Highly Efficient Electrocatalytic Hydrogen Evolution. *J. Am. Chem. Soc.* **139**, 13604-13607 (2017).

14. Zhou, Z. et al. CoP nanoparticles embedded in P and N co-doped carbon as efficient bifunctional electrocatalyst for water splitting. *J. Energy Chem.* (2017).

15. Hanlon, D. et al. Production of Molybdenum Trioxide Nanosheets by Liquid Exfoliation and Their Application in High-Performance Supercapacitors. *Chem. Mater.* **26**, 1751-1763 (2014).

16. Carey, B.J. et al. Two solvent grinding sonication method for the synthesis of two-dimensional tungsten disulphide flakes. *Chem. Commun.* **51**, 3770-3773 (2015).

17. Kalantar-zadeh, K. et al. Synthesis of nanometre-thick MoO_3 sheets. *Nanoscale* **2**, 429-433 (2010).

18. Mouat, A.R. et al. Reactivity of a Carbon-Supported Single-Site Molybdenum Dioxo Catalyst for Biodiesel Synthesis. *ACS Catal.* **6**, 6762-6769 (2016).

19. Lu, X. et al. Preparation of quantum dots from MoO_3 nanosheets by UV irradiation and insight into morphology changes. *J. Mater. Chem. C* **4**, 11449-11456 (2016).

20. Tan, X. et al. Plasmonic MoO_{3-x}@MoO_3 nanosheets for highly sensitive SERS detection through nanoshell-isolated electromagnetic enhancement. *Chem. Commun.* **52**, 2893-2896 (2016).

21. Balendhran, S. et al. Enhanced Charge Carrier Mobility in Two-Dimensional High Dielectric Molybdenum Oxide. *Adv. Mater.* **25**, 109-114 (2013).

22. Li, L., Zhang, T., Yan, J., Cai, X. & Liu, S. P Doped MoO_{3-x} Nanosheets as Efficient and Stable Electrocatalysts for Hydrogen Evolution. *Small* **13**, 1700441 (2017).

23. Alsaif, M.M.Y.A. et al. Substoichiometric two-dimensional molybdenum oxide flakes: a plasmonic gas sensing platform. *Nanoscale* **6**, 12780-12791 (2014).

24. Balendhran, S. et al. Two-Dimensional Molybdenum Trioxide and Dichalcogenides. *Adv. Funct. Mater.* **23**, 3952-3970 (2013).

25. Bai, H. et al. Direct growth of defect-rich MoO_{3-x} ultrathin nanobelts for efficiently catalyzed conversion of isopropyl alcohol to propylene under visible light. *J. Mater. Chem. A* **4**, 1566-1571 (2016).

26. Lajaunie, L., Boucher, F., Dessapt, R. & Moreau, P. Quantitative use of electron energy-loss spectroscopy Mo-M2,3 edges for the study of molybdenum oxides. *Ultramicroscopy* **149**, 1-8 (2015).

27. Hanson, E.D. et al. Systematic Study of Oxygen Vacancy Tunable Transport Properties of Few-Layer MoO_{3-x} Enabled by Vapor-Based Synthesis. *Adv. Funct. Mater.* **27**, 1605380 (2017).

28. Kim, H.-S. et al. Oxygen vacancies enhance pseudocapacitive charge storage properties of MoO_{3-x}. *Nat. Mater.* **16**, 454-460 (2017).

29. Dieterle, M., Weinberg, G. & Mestl, G. Raman spectroscopy of molybdenum oxides Part I. Structural characterization of oxygen defects in MoO_{3-x} by DR UV/VIS, Raman spectroscopy and X-ray diffraction. *Phys. Chem. Chem. Phys.* **4**, 812-821 (2002).

30.   Mestl, G., Ruiz, P., Delmon, B. & Knozinger, H. Oxygen-Exchange Properties of MoO$_3$: An in situ Raman Spectroscopy Study. *J. Phys. Chem.* **98**, 11269-11275 (1994).

31.   Spevack, P.A. & McIntyre, N.S. A Raman and XPS investigation of supported molybdenum oxide thin films. 1. Calcination and reduction studies. *J. Phys. Chem.* **97**, 11020-11030 (1993).

32.   Dadze, T.P., Kashirtseva, G.A., Novikov, M.P. & Plyasunov, A.V. Solubility of MoO$_3$ in acid solutions and vapor-liquid distribution of molybdic acid. *FFE* **440**, 64-76 (2017).

33.   Cannon, P. The solubility of molybdenum trioxide in various mineral acids. *J. Inorg. Nucl. Chem.* **11**, 124-127 (1959).

34.   van Drunen, J. et al. Electrochemically Active Nickel Foams as Support Materials for Nanoscopic Platinum Electrocatalysts. *ACS Appl. Mater. Interfaces* **6**, 12046-12061 (2014).

35.   Shinagawa, T., Garcia-Esparza, A.T. & Takanabe, K. Insight on Tafel slopes from a microkinetic analysis of aqueous electrocatalysis for energy conversion. *Sci. Rep.* **5**, 13801 (2015).

36.   Morales-Guio, C.G., Stern, L.-A. & Hu, X. Nanostructured hydrotreating catalysts for electrochemical hydrogen evolution. *Chem. Soc. Rev.* **43**, 6555-6569 (2014).

37.   Wu, R., Zhang, J., Shi, Y., Liu, D. & Zhang, B. Metallic WO$_2$–Carbon Mesoporous Nanowires as Highly Efficient Electrocatalysts for Hydrogen Evolution Reaction. *J. Am. Chem. Soc.* **137**, 6983-6986 (2015).

38.   Li, C.W., Ciston, J. & Kanan, M.W. Electroreduction of carbon monoxide to liquid fuel on oxide-derived nanocrystalline copper. *Nature* **508**, 504-507 (2014).

39.	Xie, J. et al. Defect-Rich MoS_2 Ultrathin Nanosheets with Additional Active Edge Sites for Enhanced Electrocatalytic Hydrogen Evolution. *Adv. Mater.* **25**, 5807-5813 (2013).

40.	de Castro, I.A. et al. Molybdenum Oxides – From Fundamentals to Functionality. *Adv. Mater.*, 1701619 (2017).

41.	Voiry, D. et al. Enhanced catalytic activity in strained chemically exfoliated WS_2 nanosheets for hydrogen evolution. *Nat. Mater.* **12**, 850-855 (2013).

42.	Lukowski, M.A. et al. Enhanced Hydrogen Evolution Catalysis from Chemically Exfoliated Metallic MoS_2 Nanosheets. *J. Am. Chem. Soc.* **135**, 10274-10277 (2013).

43.	Chen, Z. et al. Core–shell MoO_3–MoS_2 Nanowires for Hydrogen Evolution: A Functional Design for Electrocatalytic Materials. *Nano Lett.* **11**, 4168-4175 (2011).

44.	Wu, L., Wang, X., Sun, Y., Liu, Y. & Li, J. Flawed MoO_2 belts transformed from MoO_3 on a graphene template for the hydrogen evolution reaction. *Nanoscale* **7**, 7040-7044 (2015).

45.	Benck, J.D., Chen, Z., Kuritzky, L.Y., Forman, A.J. & Jaramillo, T.F. Amorphous Molybdenum Sulfide Catalysts for Electrochemical Hydrogen Production: Insights into the Origin of their Catalytic Activity. *ACS Catal.* **2**, 1916-1923 (2012).

46.	Luo, Z. et al. Mesoporous MoO_{3-x} Material as an Efficient Electrocatalyst for Hydrogen Evolution Reactions. *Adv. Energy Mater.* **6**, 1600528 (2016).

47.	Benck, J.D., Hellstern, T.R., Kibsgaard, J., Chakthranont, P. & Jaramillo, T.F. Catalyzing the Hydrogen Evolution Reaction (HER) with Molybdenum Sulfide Nanomaterials. *ACS Catal.* **4**, 3957-3971 (2014).

Chapter 4

Two dimensional PbMoO₄: a photocatalytic material derived from a naturally non-layered crystal

4.1. Introduction

Metal molybdates, with relatively large bivalent cations (Ba, Pb, Sr and Ca with ionic radius >0.99 Å), are typically found in the scheelite-type structures of non-layered body centred tetragonal nature.[1] These materials offer chemical and physical properties suitable for different applications.[2-13] Amongst the family of metal molybdates, lead molybdate (PbMoO₄) has shown to offer high stability and interesting photophysical and photocatalytic properties,[1, 8, 14-21] due to its favourable band edge positions.[12, 22-25] Different liquid and gas/vacuum phase synthesis methods have been used for establishing low dimensional PbMoO₄ crystals.[8, 12, 21, 24, 26-31] However, none of these methods favours the growth of nanosheets with two dimensional (2D) morphologies, as PbMoO₄ is not a naturally stratified crystal (**Figure** 4.1a).

Layered materials of van der Waals nature are traditional sources for synthesizing 2D nanosheets due to their weakly stacked layers.[32-37] A range of methods have been adopted to exfoliate layered materials, however, liquid phase exfoliation techniques are the most widely explored methods for high throughput applications.[33, 34] Nevertheless, these techniques

cannot be used for exfoliating metal molybdates such as $PbMoO_4$. These materials only exist in non-stratified crystal structures, and therefore, direct exfoliation into 2D nanosheets is not achievable.

Herein, a novel two-step room-temperature synthesis process to transform defect rich 2D α-MoO_{3-x} nanosheets into 2D $PbMoO_4$ nanosheets using aqueous $PbCl_2$ was utilized, which overcome the lack of access to $PbMoO_4$ crystals directly. In this work, a comprehensive analyses of the as synthesized and transformed 2D nanosheets is provided and carefully assessment of their 2D structural features, crystal and electronic properties are presented. The 2D sheets of $PbMoO_4$ are found to be rich in trap states and stable under simulated sun light. This work presents a strong dye degradation performance of the synthesized 2D $PbMoO_4$ nanosheets compared to other morphologies and characterize the electronic structure of the material, describing the enhanced photocatalytic activity.

4.2.   Methods

4.2.1.   Synthesis of 2D Nanosheets

Liquid phase exfoliation was utilized to synthesize 2D molybdenum oxide nanosheets. The method was adopted from previously described works with slight modifications.[38-40] Molybdenum oxide powder, 3 g (99% purity, from US Research Nanomaterials, Inc.), was ground with 600 µl ethanol for 20 mins. The ground powder was then mixed into 45 ml of ethanol solution, which was then probe-sonicated (Ultrasonic Processor GEX500) for 60 mins at 100 W. Afterwards, the probe-sonicated solution was centrifuged at 2500 rcf for 30 mins and finally, the supernatant (yellow/blue colour) containing 2D molybdenum oxide nanosheets was collected.

4.2.2. Synthesis of 2D PbMoO₄ Nanosheets Using Lead (Pb) Ions

In this work, 1 mM of $PbCl_2$ solution was prepared separately, in Milli-Q water. Transformation of 2D nanosheets into 2D $PbMoO_4$ was achieved by mixing 2D molybdenum oxide nanosheets suspension (dispersed in Milli-Q water) with a small amount of $PbCl_2$ solution (1 ml of as prepared $PbCl_2$ solution in 8 ml of 2D molybdenum oxide suspension). From this mixture, the excess $PbCl_2$ was removed following high speed centrifugation process and 2D $PbMoO_4$ nanosheets were collected.

4.2.3. Apparatus

Atomic force microscopy (AFM) was carried out using a Bruker Dimension Icon AFM. X-ray photoelectron spectroscopy (XPS) was conducted on a Thermo scientific K-Alpha instrument equipped with monochromated aluminium K- α source (1486.7 eV). Raman spectroscopy was performed using 532 nm laser on a LabRAM HR Evolution Raman spectrometer (Horiba Scientific). X-ray diffraction (XRD) patterns of the 2D nanosheets were collected using a Bruker D4 ENDEAVOR with monochromatic Cu Kα as radiation source (λ= 0.154 nm). The solutions containing 2D nanosheets were drop casted onto Cu grids for high resolution transmission electron microscopy (HRTEM - JEOL 2100F) characterizations. Transmission electron microscopy (TEM) was conducted using JEOL 1010. The amount of weight variation of the material, as a function of increasing temperature and time, were evaluated by thermogravimetric analysis (TGA) using Perkin Elmer Pyris 1 in an atmosphere of nitrogen gas, providing a measure of the 2D MoO_3 concentration. Absorbance pattern measurements were recorded using an Agilent Cary 60 Ultraviolet-Visible (UV-Vis) Spectrophotometer and Lambda 1050 UV/Vis/NIR Spectrometer (Perkin Elmer) equipped with a 150 mm InGaAs integrating sphere. Zeta potentials of the 2D nanosheets were determined using a Zetasizer Nano ZS equipment (Malvern Instruments, Worcestershire,

UK). The photoemission spectroscopy in air (PESA) was performed using a Riken Keiki AC-2, photoelectron spectrometer. Inductively coupled plasma mass spectrometry (ICP-MS) was conducted using Agilent Technologies HP4500 series 300, Shield Torch ICP-MS. The working solution was mixed with 2% nitric acid before conducting the measurements.

4.2.4. *Evaluation of Photocatalytic Activity*

Photocatalytic activities of the as-synthesized samples were evaluated by the degradation of rhodamine B (RhB) in aqueous solution. In this work, 1 mL of the 10 µM dye solution was added into ~75 µg (dispersed in 4 mL of Milli-Q water) of the photocatalysts. The solutions were allowed to stabilize for 30 min in the dark prior to any experiment. The photocatalytic degradation of RhB was performed using a Sol3A class AAA solar simulator IEC/JIS/ASTM equipped with a 450 W Xenon lamp. A silicon reference cell (accredited by NIST to the ISO-17025 standard) was utilized to adjust the power of the illuminated solar light to precisely 1 sun (AM1.5).

4.3.   Results and discussion

The 2D molybdenum oxide nanosheets were synthesized using a procedure that was previously developed (described in the Methods section and chapter 3 of this thesis).[40] In brief, 2D molybdenum oxide suspensions were first obtained from the bulk α-MoO_3 powder following a grinding-assisted mechanical liquid phase exfoliation method. The suspension has a yellow/blue colour (**Figure** 4.1). The yield of the 2D molybdenum oxide nanosheets was measured as ~18.5 µg/mL, following a previously reported method using TGA.[39] Here, ethanol enhanced the exfoliation process due to its favourable synergy with the surface

energy of α-MoO$_3$.[39] In addition, the suitable properties of ethanol and surface energy of α-MoO$_3$ facilitate a stable colloidal suspension after exfoliation.[39, 41, 42]

For a Pb containing salt in an aqueous solution the dominant species are Pb^{2+} or Pb(OH)$^+$.[43] As the zeta potential shows negative surface charge MoO$_3$, it is expected that Pb^{2+} or Pb(OH)$^+$ are electrostatically attracted to the surface of this material. The favourable band and crystal structure of MoO$_3$ allows the efficient intercalation of Pb^{2+} or Pb(OH)$^+$ species into layered α-MoO$_3$. Here, Pb^{2+} cations acts as electron pair acceptors (Lewis acids), where the electron pair donors (Lewis bases) are MoO$_2^{4-}$ anions which are electron pair donor units.[1] However, this intercalation is topotactic, which result in the structural changes and the formation of scheelite-type PbMoO$_4$.

Here, the formation of 2D PbMoO$_4$ nanosheets was achieved by stirring of the 2D α-molybdenum oxide suspension (dispersed in Milli-Q water) with the aqueous PbCl$_2$ solution (see Experimental Methods). Excess salt was removed using a centrifugation based workup protocol and the obtained 2D PbMoO$_4$ nanosheets were finally dispersed in Milli-Q water. The crystal structures of both of the materials (**Figure** 4.1a) and a schematic describing the step-by-step synthesis process from bulk α-MoO$_3$ to 2D molybdenum oxide and 2D PbMoO$_4$ nanosheets are presented in **Figure** 4.1b.

A series of characterizations were applied to assess the 2D structural features and crystal properties of both 2D molybdenum oxide and 2D PbMoO$_4$ nanosheets. Furthermore, these nanosheets were then incorporated for photocatalytic reactions to evaluate their potentials in degradation of organic pollutants under solar light irradiation as presented in detail in the Experimental Methods section.
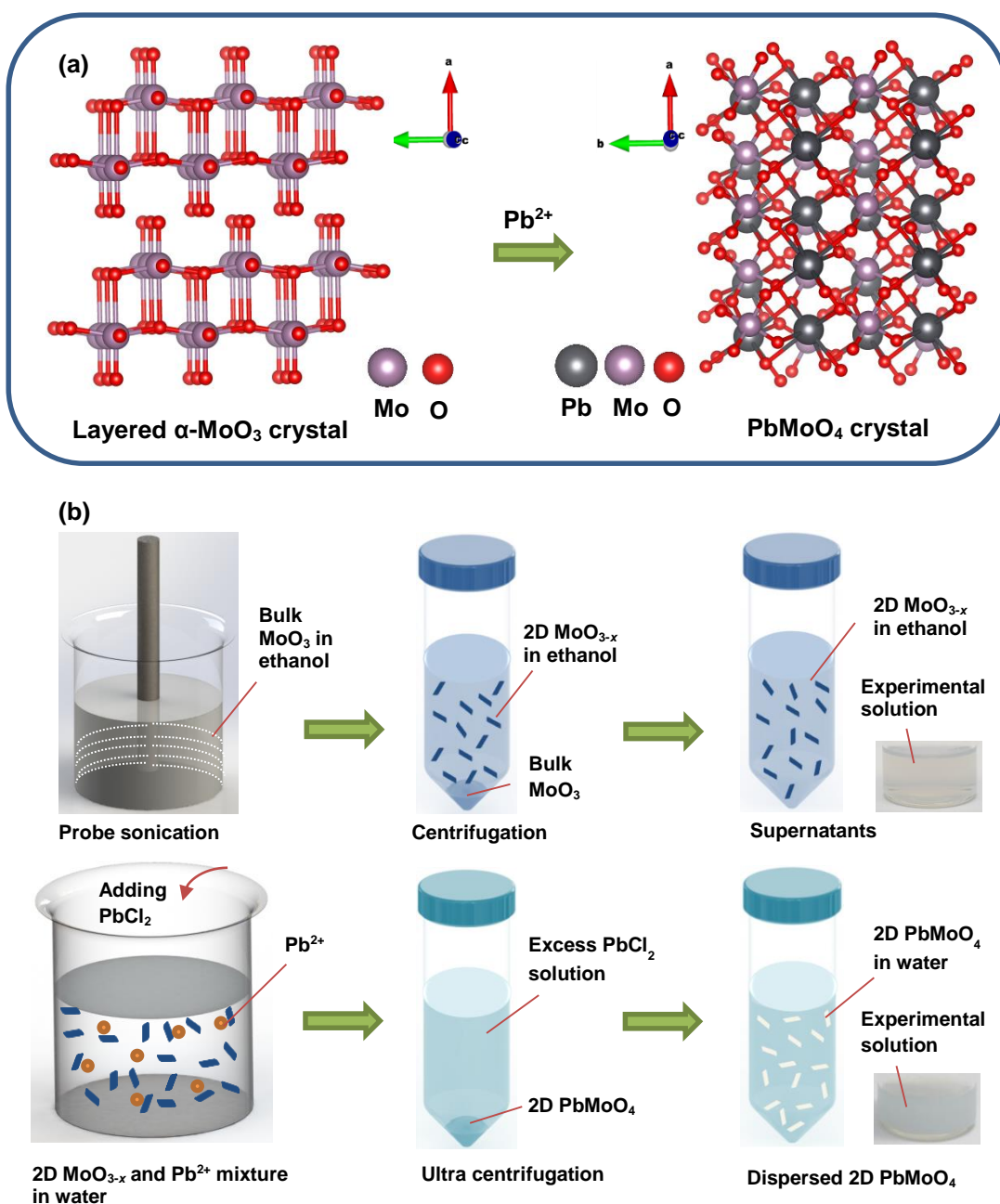
Figure 4.1. (a) Crystal structures of orthorhombic α-MoO$_3$ and scheelite-type PbMoO$_4$ and (b) schematic diagram describing the step-by-step synthesis process from bulk MoO$_3$ to 2D PbMoO$_4$ nanosheets.

The thicknesses and lateral dimensions of the 2D nanosheets were investigated using AFM. As can be seen, the thickness of pristine exfoliated 2D molybdenum oxide nanosheets has the

average thickness ($T_{average}$) of ~4.5 nm (**Figure** 4.2a), which corresponds to ~6 fundamental layers of α-MoO$_3$ (monolayer thickness is 0.7 nm).[44] AFM analysis of the 2D PbMoO$_4$ nanosheets revealed that their thickness on average increased by 0.6 nm compared to the 2D molybdenum oxide nanosheets (see **Figure** 4.2d). This increase in the thickness of the nanosheets occurred due to the Pb^{2+} uptake in the sheets and crystal structure transformation. AFM also revealed that the pristine 2D molybdenum oxide and 2D PbMoO$_4$ nanosheets have average lateral sizes ($L_{average}$) of approximately 125 and 120 nm, respectively (**Figure** 4.2c, f). The difference is within the measurement error, which signifies that the lateral dimensions of the nanosheets have not changed after the formation of 2D PbMoO$_4$ nanosheets. The $T_{average}$ and $L_{average}$ values obtained for both 2D molybdenum oxide and 2D PbMoO$_4$ nanosheets also lead to aspect ratios ($L_{average}$ / $T_{average}$) of ~28 and ~25, respectively, which is in agreement with the previously reported values obtained for the exfoliated 2D molybdenum oxide nanosheets using the adopted method.[39] Interestingly, the AFM characterisations also revealed that both of the 2D nanosheets contain step-rich basal surfaces (**Figure** 4.2b, e), which should enhance the dangling bonds and reaction active sites.[40]
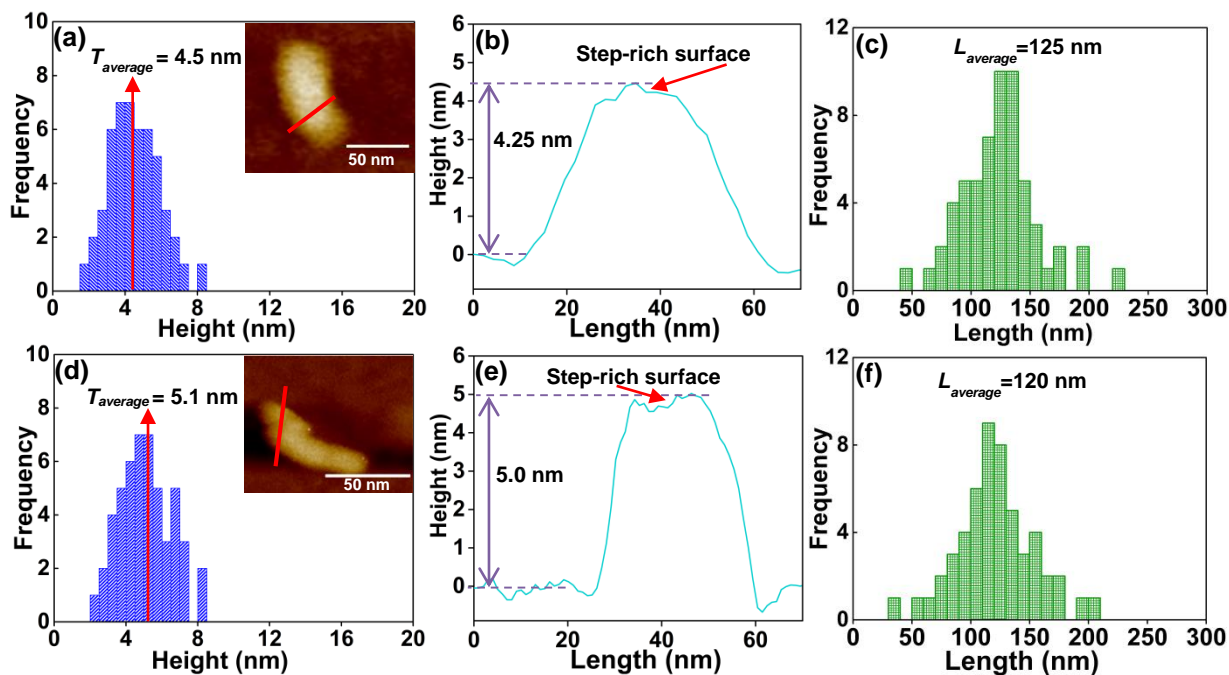
Figure 4.2. AFM characterization of 2D nanosheets (a, b, c) frequency histogram of the observed thickness and AFM image of the nanosheet (inset), corresponding thickness profile, frequency histogram of the observed lateral sizes of the 2D molybdenum oxide nanosheets and (d, e, f) frequency histogram of the observed thickness and AFM image of the nanosheet (inset), corresponding thickness profile, frequency histogram of the observed lateral sizes of the 2D PbMoO$_4$ nanosheets.

The XPS was utilized to investigate the changes to the chemical environment and binding energies of the 2D molybdenum oxide due to the formation of 2D PbMoO$_4$ nanosheets. The XPS spectra of the Mo $3d$ region are presented **Figure** 4.3. The Mo $3d_{3/2}$ and Mo $3d_{5/2}$ peaks are observed in the expected region for the pristine exfoliated 2D MoO$_3$ nanosheets.[38] Due to the formation of 2D nanosheets, two new peaks at the lower binding energies of 235.9 and 232.8 eV were observed, which correspond to the Mo^{5+} oxidation state (see **Figure** 4.3a).[39, 45] The emergence of Mo^{5+} oxidation state indicates the presence of oxygen vacancies in the 2D

nanosheets and thus, the material represents reduced 2D α-MoO$_{3-x}$ structure,[46] rather than stoichiometric α-MoO$_3$. Upon the Pb^{2+} uptake, a shift to lower binding energies was observed for both peaks, confirming the aforementioned charge transfer.[47] In **Figure** 4.3b, Mo $3d_{5/2}$ peak at 232.6 eV and Mo $3d_{3/2}$ peak at 235.6 eV represent Mo^{6+} oxidation state in 2D PbMoO$_4$.[22, 48, 49] These values were found to be in agreement with the previously reported literature with binding energy difference of the $3d$ doublets as 3 eV for PbMoO$_4$, in comparison to α-MoO$_3$ that shows a difference of 3.1 eV.[38, 48, 49] The shift to lower binding energies and slight change in the energy difference of the two peaks indicate the change in the environment around Mo atoms due to Pb^{2+} uptake.[47] In addition, the binding energy of O $1s$ increased from 531.4 to 532.2 eV for the 2D PbMoO$_4$ compared to 2D α-MoO$_{3-x}$ (see **Figure** 4.3c, d), which shows the possible change in the chemical state of O.[22] From the Pb $4f$ XPS spectrum of the 2D PbMoO$_4$ presented in **Figure** 4.3e, it is observed that doublet peaks appear at 138.3 and 143.4 eV, which are assigned to Pb $4f_{7/2}$ and Pb $4f_{5/2}$, respectively.[50, 51] These peaks represent the Pb-O bond, which emerges from Pb^{2+} ions of PbMoO$_4$.[23, 51]
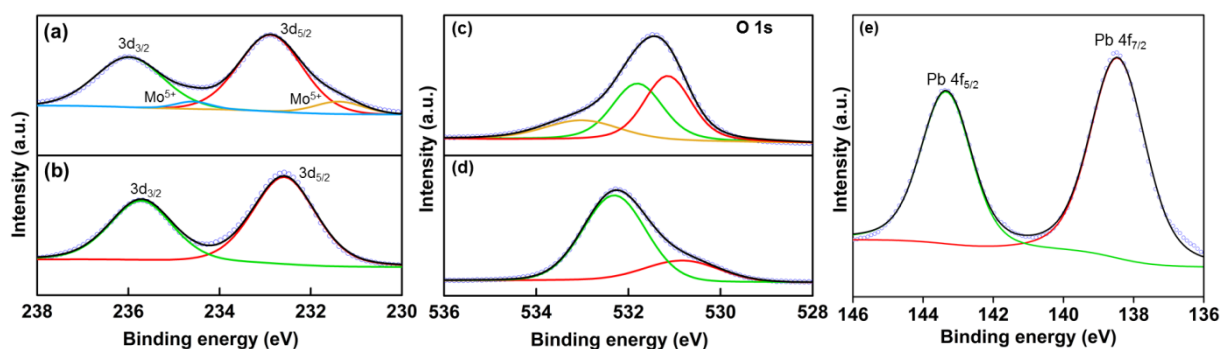
Figure 4.3. (a, b) Mo 3d XPS spectra of 2D α-MoO$_{3-x}$ and 2D PbMoO$_4$, (c, d) O 1s XPS spectra of 2D α-MoO$_{3-x}$ and 2D PbMoO$_4$, (e) Pb 4f XPS spectra of 2D PbMoO$_4$. Dotted rings represent the original data.

The samples were then characterized using Raman spectroscopy to evaluate their vibrational changes before and after the formation of 2D PbMoO$_4$. The measurements were conducted at 532 nm excitation (with 0.9 mW laser power) and samples were tested on gold coated substrates. Raman spectrum of 2D α-MoO$_{3-x}$ exhibits strong peaks at the 282, 664, 818, and 995 cm^{-1}, which are all in agreement with the previously reported peak positions of slightly reduced orthorhombic molybdenum oxide (see **Figure** 4.4a).[38, 52] The 282 cm^{-1} peak correspond to the bending mode for the double bond (Mo=O) vibration and the peak at 664 cm^{-1} is related to the tri-coordinated oxygen (Mo$_3$–O) stretching mode.[53] The 818 cm^{-1} peak can be assigned to the bi-coordinated oxygen (Mo$_2$–O) stretching mode, while the 995 cm^{-1} peak is attributed to the terminal oxygen (Mo^{6+}=O) stretching mode.[39] The Raman peaks at lower wavenumbers of 375 and 336 cm^{-1} represent the Mo=O and Mo$_3$–O bending modes, respectively.[53] Additionally, the 489 and 890 cm^{-1} peaks represent the oxygen vacancies in 2D α-MoO$_{3-x}$ nanosheets, which can be ascribed to Mo=O and Mo$_2$–O stretching modes of α-MoO$_{3-x}$, respectively.[40, 54] Interestingly, several new intense peaks appeared (while all the conventional α-MoO$_3$ peaks disappeared) upon Pb^{2+} uptake (see **Figure** 4.4b), which may be due to structural changes induced by the insertion of Pb^{2+} into 2D α-MoO$_{3-x}$ nanosheets. The Raman peak at 868 cm^{-1} corresponds to the symmetric stretching of [MoO$_4$] clusters in the PbMoO$_4$ crystal.[55] The peaks at 742 and 768 cm^{-1} can be assigned to the anti-symmetric vibration and stretching modes, respectively.[55] The modes at 317 and 348 cm^{-1} represent the asymmetric and symmetric bending of MoO$_4$ tetrahedrons, respectively.[56] These results are in agreement with the scheelite-type PbMoO$_4$ structure,[57, 58] suggesting a complete transformation of 2D α-MoO$_{3-x}$ crystals into 2D PbMoO$_4$.
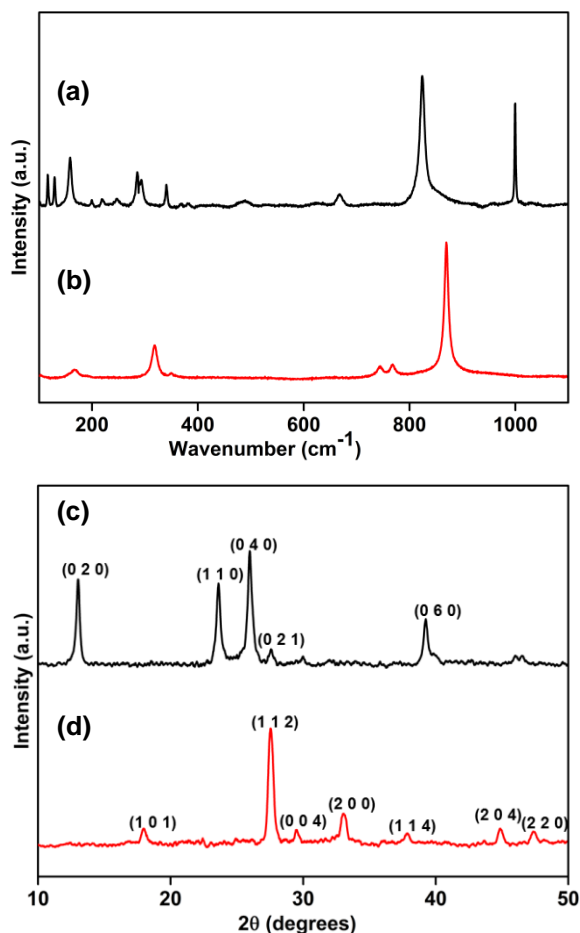
Figure 4.4. Raman spectra of (a) 2D α-MoO$_{3-x}$ and (b) 2D PbMoO$_4$ and XRD patterns of (c) 2D α-MoO$_{3-x}$ and (d) 2D PbMoO$_4$.

XRD patterns of both the materials deposited on glass substrates were analyzed in order to understand any changes in the crystal structure of the 2D α-MoO$_{3-x}$ after the reaction with Pb^{2+} ions. Peaks of 2D α-MoO$_{3-x}$ are indexed to orthorhombic molybdenum oxide crystal structure with lattice parameters of a = 3.962 Å, b = 13.858 Å, c = 3.697 Å (JCPDS 05-0508). The most intense diffraction peaks correspond to the (0 2 0), (1 1 0), (0 4 0), (0 2 1) and (0 6 0) planes of 2D α-MoO$_{3-x}$, respectively (see **Figure** 4.4c).[39, 53] In the 2D PbMoO$_4$ sample, several new intense peaks were found to appear at 17.8°, 27.5°, 29.3°, 32.9°, 37.9°, 44.9°, and 47.3°, while the conventional α-MoO$_3$ peaks disappeared. The XRD patterns in the

2D PbMoO$_4$ sample are in agreement with diffraction patterns observed for the body-centered tetragonal structure (scheelite-type) of PbMoO$_4$ crystals (JCPDS card no. 44–1486), indicating the transition from orthorhombic molybdenum oxide to PbMoO$_4$ crystal.[52, 59] The most intense diffraction peaks can be assigned to the (1 0 1), (1 1 2), (0 0 4), (2 0 0), (1 1 4), (2 0 4), and (2 2 0) planes of 2D PbMoO$_4$ nanosheets, respectively (see **Figure** 4.4d).[1, 52] The XRD signatures, together with the findings of Raman spectroscopy, are strong identifications that significant and complete crystal transformation from 2D α-MoO$_{3-x}$ to 2D PbMoO$_4$ crystals has taken place.

The atomic scale crystal changes in the 2D sheets were further investigated using the HRTEM analysis. Here the lattice fringes of the 2D α-MoO$_{3-x}$ nanosheets exhibit a spacing of 0.39 nm (see **Figure** 4.5a), which is associated to the (1 0 0) plane of α-MoO$_{3-x}$.[38, 40] The corresponding fast Fourier transform (FFT) patterns also revealed (1 0 0) plane (inset of **Figure** 4.5b), which is associated to the orthorhombic crystal structure of α-MoO$_{3-x}$.[40] **Figure** 4.5b shows the TEM images of as synthesized 2D α-MoO$_{3-x}$ nanosheets, which are in accordance with the AFM analysis presented in this paper. Significant changes in the lattice fringes of 2D nanosheets occurred due to the formation of 2D PbMoO$_4$. New lattice arrangements were found with a spacing of 0.22 nm (**Figure** 4.5c), which is consistent with the (1 0 5) plane of scheelite–PbMoO$_4$.[53] This plane is also in accordance with the corresponding FFT patterns (inset of **Figure** 4.5d). **Figure** 4.5d presents the obtained 2D PbMoO$_4$ nanosheets, which is also in agreement with the AFM study. These observations confirm that the Pb^{2+} ions induced a structural transition from highly crystalline orthorhombic α-MoO$_{3-x}$ to highly crystalline scheelite PbMoO$_4$ nanosheets.
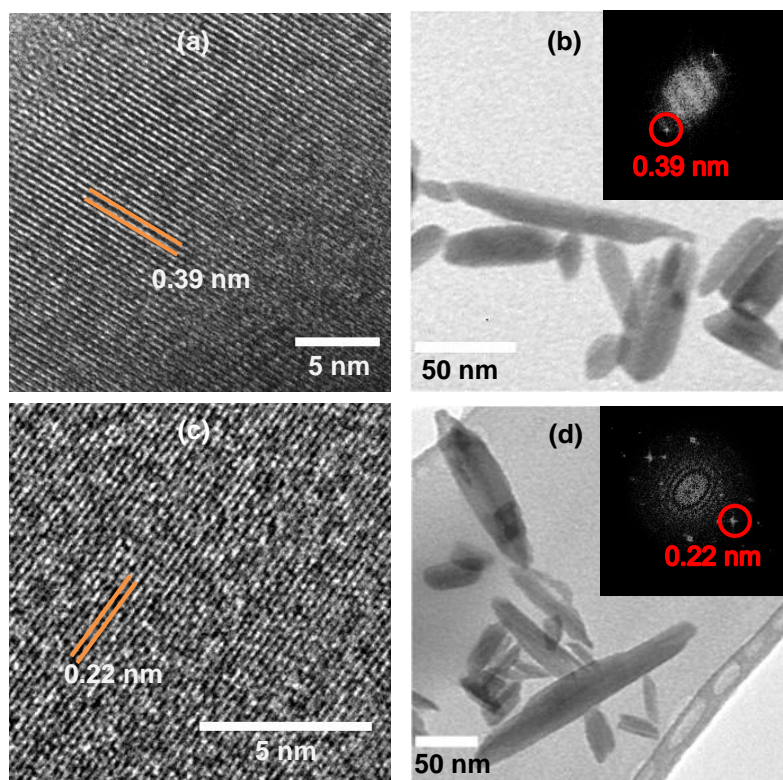
Figure 4.5. HRTEM images with corresponding FFT patterns (insets) and large area TEM images of (a, b) 2D α-MoO$_{3-x}$ and (c, d) 2D PbMoO$_4$.

For a comprehensive evaluation of the semiconducting properties of 2D α-MoO$_{3-x}$ and 2D PbMoO$_4$ nanosheets, the electronic band structure of the nanosheets were determined using Tauc plots from UV-Vis measurements, together with XPS valence band (VB) spectra and PESA analysis.

In order to determine the bandgap of both the 2D nanosheets, integrating sphere supported UV-Vis spectroscopy was conducted. The 2D α-MoO$_{3-x}$ suspension spectrum has an absorbance appearing from 420 nm extending to lower wavelengths (see inset of **Figure** 4.9a) and in agreement with previously reported literature.[60] Here the bandgap of the exfoliated material is ~3.1 eV (see **Figure** 4.6a). For the 2D PbMoO$_4$ nanosheet suspension, absorbance starts from a lower wavelength region at 380 nm (see inset of **Figure** 4.8a) due to its wider

bandgap.[61, 62] Here the molybdate, which has been suggested to have a direct band structure[23], has the bandgap value of ~3.40 eV (see **Figure** 4.6b).

The VB XPS spectrum determines the difference between valence band maximum (VBM) and the Fermi level.[63, 64] Here, the XPS VB spectra revealed that the VBM position for 2D α-MoO$_{3-x}$ resides at 3.0 eV below the Fermi level (see **Figure** 4.6c), where the value was found to be 2.8 eV for the 2D PbMoO$_4$ nanosheets (see **Figure** 4.6d). Interestingly, the XPS VB spectra of both the 2D nanosheets exhibit the presence of trap states within the VB and Fermi levels in both cases (see **Figure** 4.6c, d). In 2D metal oxide nanosheets, the trap states arise from the oxygen or metal ion vacancies.[63, 65] As the initial 2D α-MoO$_{3-x}$ contains oxygen vacancy type defects in its structure (see **Figure** 4.3a and 4.4a), the synthesized 2D PbMoO$_4$ also likely to display similar defects. The presence of trap states within the bandgap can effectively shift the photo-response towards the visible range and therefore, 2D PbMoO$_4$ become available for the efficient absorption of solar light.

The PESA signal measured for the metal oxides are often associated with the Fermi level of the material.[63, 65] Here, the Fermi level of 2D α-MoO$_{3-x}$ was found to be at -5.50 eV with respect to vacuum (vac), where the level was at -5.0 eV for the 2D PbMoO$_4$ nanosheets, indicating the shift in band structure (see **Figure** 4.6). The calculated CB positions for the 2D α-MoO$_{3-x}$ and 2D PbMoO$_4$ nanosheets are found at 5.4 eV and 4.4 eV, respectively, which are in accordance with the previously reported values.[13, 66] The estimated electronic band structures of 2D α-MoO$_{3-x}$ and 2D PbMoO$_4$ based on Tauc plot, XPS VB spectra and PESA are presented in **Figure** 4.7. The CB edge of 2D PbMoO$_4$ nanosheets is found to be well positioned to facilitate the degradation of organic pollutants. In addition, the trap states observed in the XPS VB spectra also have been incorporated in the band diagram to provide a better insight regarding the band structures.
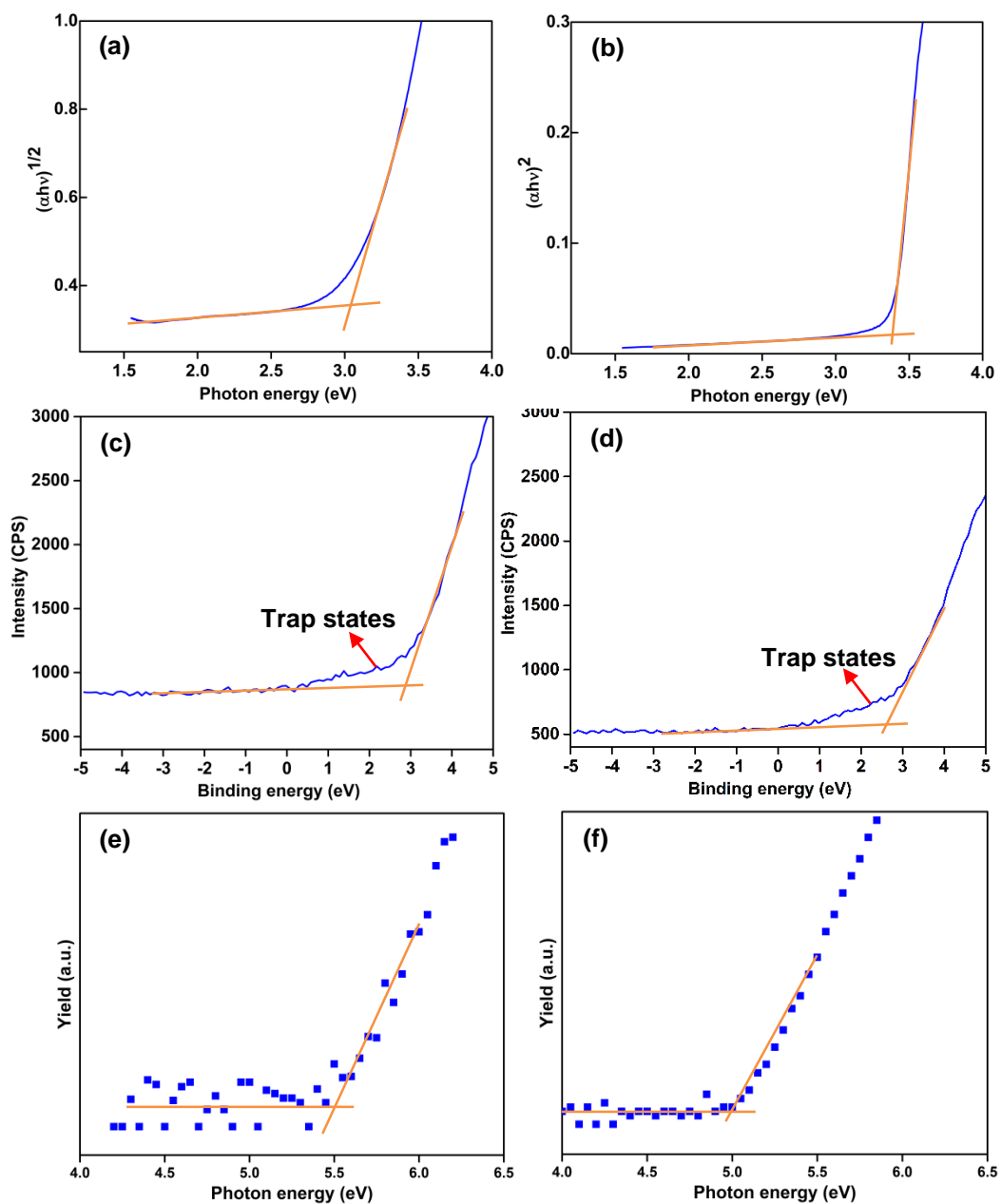
Figure 4.6. The Tauc-plots of (a) 2D α-MoO$_{3\text{-}x}$ and (b) 2D PbMoO$_4$, XPS valence graphs of (c) 2D α-MoO$_{3\text{-}x}$ and (d) 2D PbMoO$_4$ nanosheets and PESA patterns of (e) 2D α-MoO$_{3\text{-}x}$ and (f) 2D PbMoO$_4$.
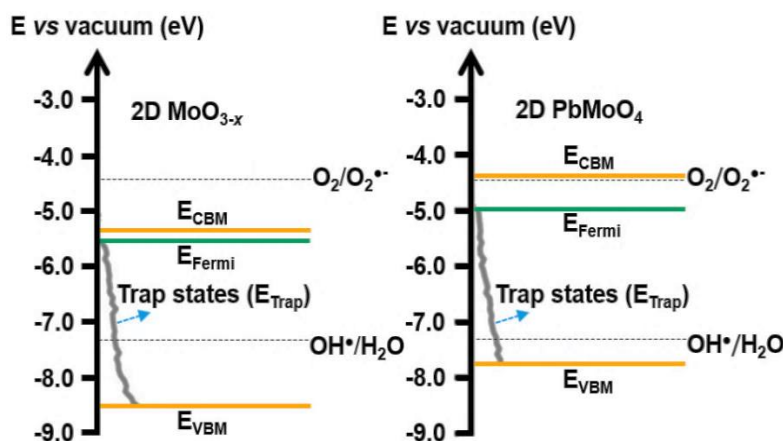
Figure 4.7. Energy level diagrams of 2D α-MoO$_{3-x}$ and 2D PbMoO$_4$ with the estimated conduction band minimum (E$_{CBM}$), valence band maximum (E$_{VBM}$) and Fermi level (E$_{Fermi}$).

In order to evaluate the surface activity of both the 2D nanosheets, photocatalytic performances were assessed *via* the decomposition of an organic pollutant. RhB compound was chosen as a standard dye due to its extensive usage in previous works on investigating photocatalytic activities.[22, 63] The gradual degradation of the characteristic absorbance spectrum for RhB dye with the aid of photocatalysts (2D nanosheets) under solar light irradiation was investigated to evaluate their photocatalytic performances. Photocatalytic degradation of RhB was carried out for 120 mins and in regular intervals (30 mins) the absorbance of each mixture was measured to evaluate the photodegradation rate in the presence of photocatalysts.

The absorbance spectra of the reaction mixtures containing RhB and suspended 2D nanosheets, before and during photocatalysis process, are presented in **Figure** 4.8a and **Figure** 4.9a. The characteristic absorption peak of RhB (centred at 554 nm) degrades significantly and nearly disappears within 120 mins in the presence of 2D PbMoO$_4$ nanosheets (**Figure** 4.8a). This also indicates the breakdown of chromophoric configuration of RhB dye. **Figure** 4.8b represents the relative absorbance change (*A$_t$/A$_0$*) and dye

degradation percentage of RhB in the presence of 2D PbMoO₄ nanosheets. In the presence of

2D PbMoO₄ nanosheets and under solar light, it is observed that 72% of RhB is eliminated

after 2 hours (**Figure** 4.8b).
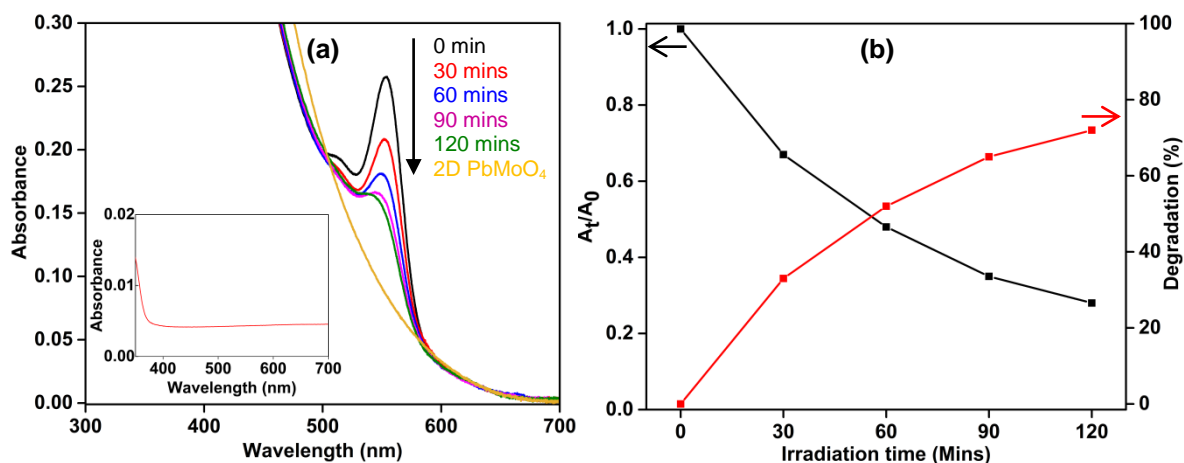
Figure 4.8.   (a) The UV-Vis absorption spectrum of RhB in the presence of the 2D

PbMoO₄ catalyst of simulated solar light irradiation with the inset showing the UV-Vis

absorption spectrum of 2D PbMoO₄ measured using an integrating sphere employed UV-Vis

equipment and (b) photo degradation of RhB in the presence of the 2D PbMoO₄ catalyst

under solar light irradiation.

In contrast, 2D α-MoO$_{3-x}$ exhibited inferior performance as a photocatlytic, where only 40%

of RhB is eliminated after 2 hours of illumination under solar light (**Figure** 4.9b). The

inferior photocatalytic performance of molybdenum oxides is often reported in the previous

literatures.[67-69] Unfortunately, 2D α-MoO$_{3-x}$ significantly reduces under solar or UV light

irradiation *via* the creation of further oxygen vacancies,[38, 39] and hence becomes unstable in

photocatalytic experiments. In addition, metal oxides tend to functionalize with carboxylic

linked organic components (such as RhB) and therefore, adsorbs strongly onto their

surface.[70, 71] This is also evident in the UV-Vis graphs, where significant change in the absorbance of lower wavelength region was observed from **Figure** 4.9a, which is likely associated with the adsorption or aggregation of dye molecules onto the surface of 2D α-MoO$_{3-x}$ nanosheets.
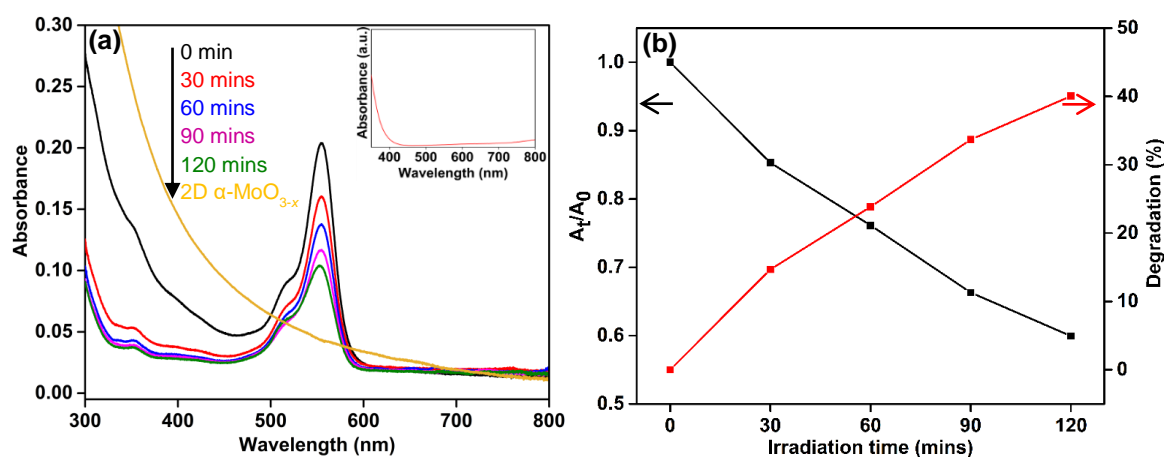
Figure 4.9. (a) UV-vis absorption spectra of RhB in the presence of the 2D α-MoO$_{3-x}$ catalyst of simulated solar light irradiation with the inset showing the UV-vis absorption spectrum of 2D α-MoO$_{3-x}$ measured using integrating sphere employed UV-vis equipment and (b) photo degradation of RhB under solar light irradiation.

The adsorption of RhB onto 2D α-MoO$_{3-x}$ nanosheets surface can also be seen in the zeta potential graph measured after the photocatalytic process. Initially, the zeta potential values for both the 2D nanosheets were measured to be negative, in which 2D molybdenum oxide showed -49.1 mV, while the 2D PbMoO$_4$ nanosheets exhibited a value of -34.5 mV (see **Figure**. 4.10a, b). The relatively large absolute zeta potential values for both the materials indicate good electrostatic stability of the colloidal dispersions.[39] This means high electrostatic repulsion is present between the adjacent 2D nanosheets, which prevents the aggregation. In order to investigate the mid-term stability of the colloidal dispersions, both

the samples were assessed after 7 days. Only 1.4 and 1 mV drop was observed for the 2D molybdenum oxide and 2D PbMoO$_4$ nanosheets, respectively (see **Figure** 4.11). These values are still in the range of good stability that signify their stable colloidal dispersions.[39] However, a significant drop of ~25 mV was observed compared to the initial 2D MoO$_{3-x}$ nanosheets due to the absorption of RhB molecules, which suggests that the materials are highly aggregated (see **Figure** 4.10c). In contrast, only ~3 mV drop was observed for the 2D PbMoO$_4$ nanosheets (see **Figure** 4.10d), which signifies the stability of 2D PbMoO$_4$ nanosheets for the photocatlytic degradation of RhB molecules.
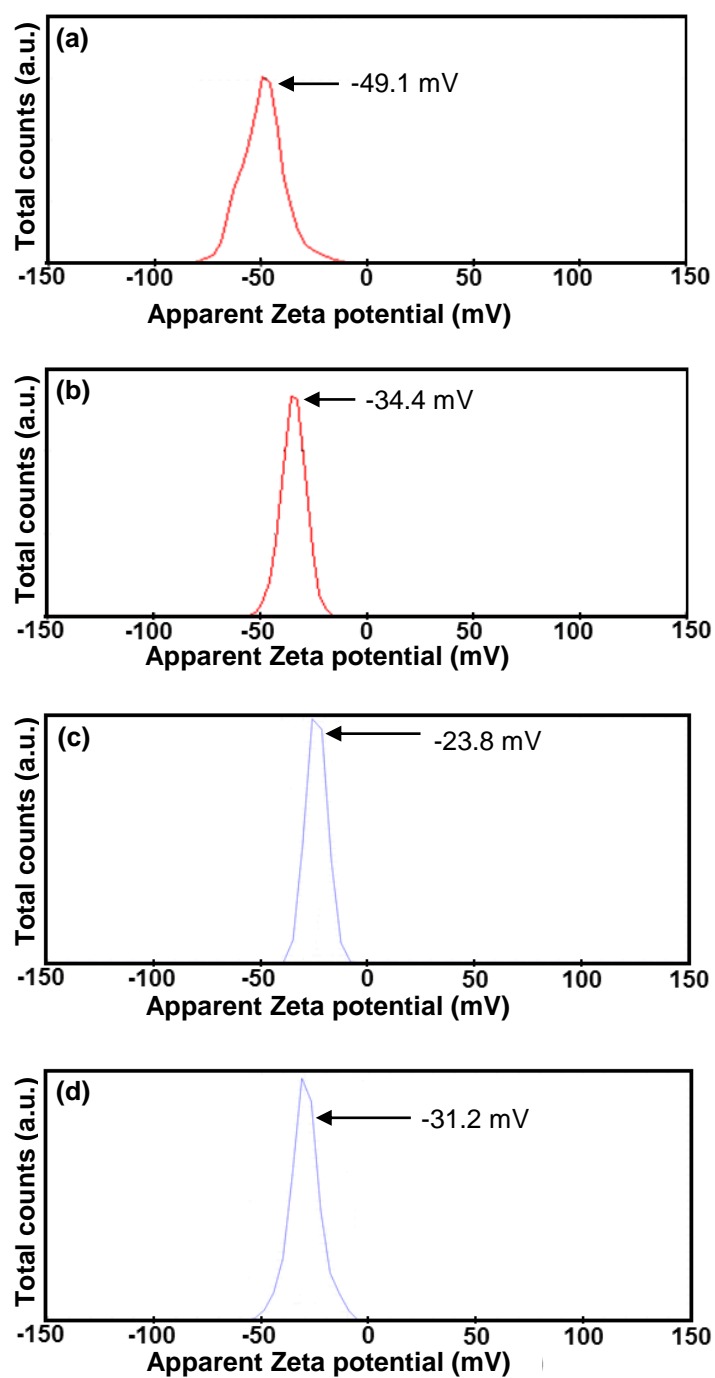
Figure 4.10. Zeta potential graphs of (a) initial 2D α-MoO$_{3-x}$ and (b) 2D PbMoO$_4$, and (c) 2D α-MoO$_{3-x}$ and (d) 2D PbMoO$_4$ after RhB degradation.
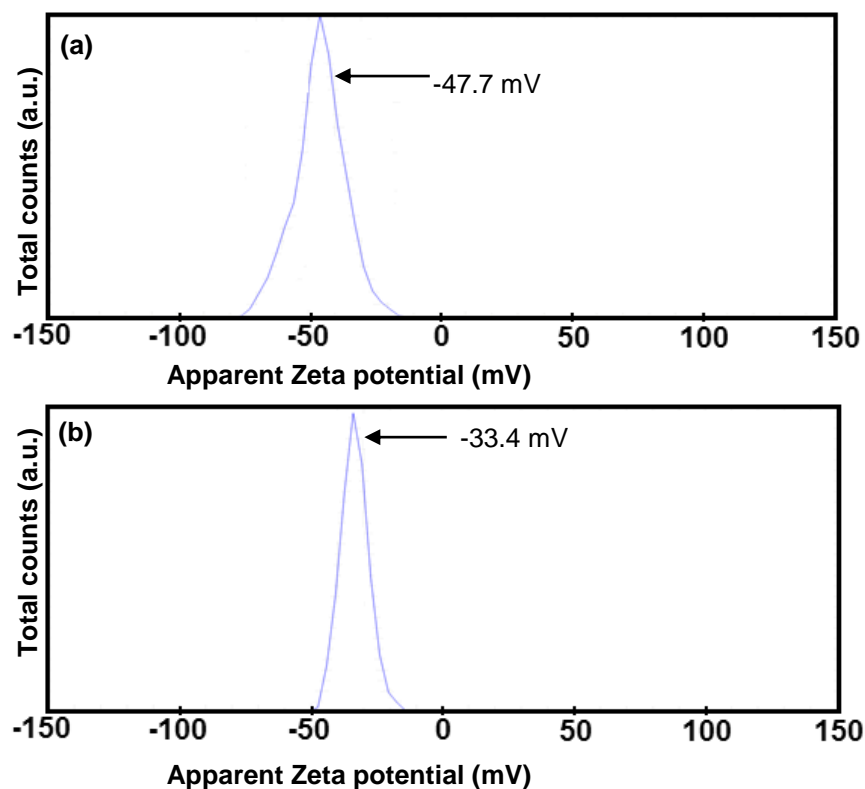
Figure 4.11. Zeta potential graphs of (a) 2D α-MoO$_{3-x}$ and (b) 2D PbMoO$_4$ after 7 days.

In addition, blank experiments were conducted without any solar light illumination to assess the adsorption effect of dye molecules onto the surface of the catalysts. Overall, the observation of the dark experiment signifies the effective degradation of organic molecules by the 2D PbMoO$_4$ as only ~7% RhB degraded without the solar light illumination after 120 mins (**Figure** 4.12a). However, the blank experiment conducted using 2D MoO$_{3-x}$ revealed a significant adsorption effect of the RhB molecules to the surface as predicted. This control experiment confirmed that ~24% decrease in the intensity of RhB peak occurred during the experimental timeframe of 120 mins (**Figure** 4.12b), confirming the adsorption of RhB onto aggregated 2D α-MoO$_{3-x}$ nanosheets. **Figure** 4.13 represents the optical images of this experiment, which signify the adsorption effects of RhB molecules on 2D α-MoO$_{3-x}$ nanosheets.
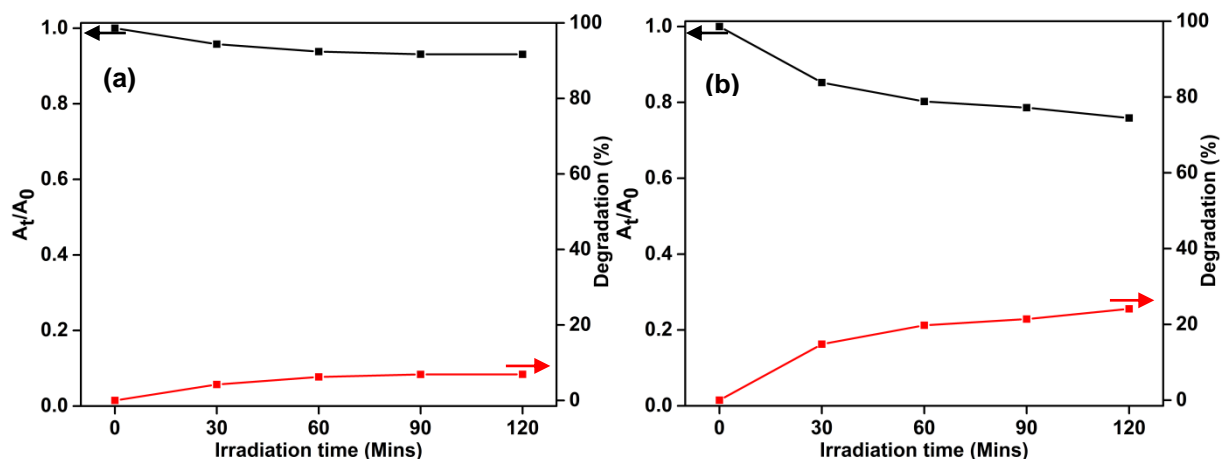
Figure 4.12. The photo degradation of RhB in the presence of (a) 2D PbMoO$_4$ catalyst and (b) 2D MoO$_{3-x}$ catalyst without solar light irradiation.
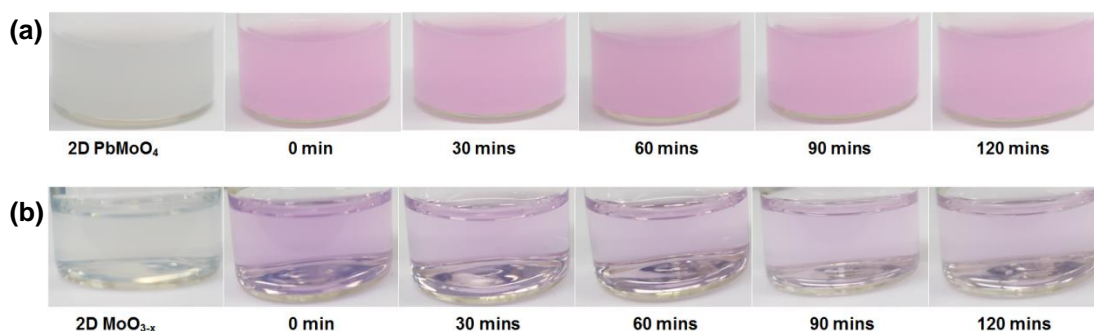
Figure 4.13. Optical images of the photo degradation of RhB in the presence of (a) 2D PbMoO$_4$ catalyst and (b) 2D MoO$_{3-x}$ catalyst without solar light irradiation.

A comparison between the dye degradation performance of 2D PbMoO$_4$ nanosheets observed in this work and a selection of previous reports on lead molybdates and tungstates with different morphologies are summarized in Table 1. As can be seen in Table 1, most of the

reports utilized high power UV illumination, which do not comply with the experimental conditions applicable for the real life applications.[63] Additionally, the usage of high power UV illumination results in exaggerated dye-degradation rates in wide bandgap semiconductors.[63] In contrast, the experimental procedure adopted in this work employs a custom designed solar simulator that illuminates calibrated solar light with a spectrum that nearly represents natural solar irradiation. Despite being investigated only under the simulated sun light and not the UV light, the photocatalytic performance of 2D $PbMoO_4$ nanosheets outperforms all previous reports presented in **Table** 4.1, which indicates the superiority and importance of 2D $PbMoO_4$ nanosheets in photocatalytic degradation of organic pollutants, in comparison to other nano morphologies of this crystal.

Table 4.1. Summary of RhB degradation performances of lead molybdates and tungstates.

Material	Morphology	Dimension / Thickness	Surface area m^2/g	Light source	Dye concentration (g/L)	Degradation rate (%μmolg^{-1}h^{-1})	Ref
$PbMoO_4$	Spherical nanoparticles	~50 nm/-	1.1	UV lamp	0.005	0.25	[24]
$PbMoO_4$ (in pH 4)	Spherical nanoparticles	~50 nm/-	1.1	UV lamp	0.005	1.1	[24]
$PbMoO_4$	Oval shape particles	~250 nm/-	2.52	UV lamp	0.005	7	[12]
Eu^{3+} doped $PbWO_4$	Dendritic nanostructures	12 μm/-	-	Mercury lamp	-	5.7	[65]
$PbWO_4$	Micro-leaves	~6 μm/-	2	Visible light	0.005	3.25	[72]
$PbMoO_4$	Two-dimensional nanosheets	120 nm/ 5.1 nm	45.23	Solar lamp	0.005	69.3	This work

The rate constant of the dye degradation was also determined using the Langmuir Hinchelwood model. The Langmuir–Hinshelwood expression identifies the kinetics of photocatalytic processes and it is given below[73]:

$$r = \frac{k_r KC}{1 + KC}$$

Here, r represents the rate of reaction that changes with time t, k_r is the reaction rate constant (slope of ln(C/C_0) vs Time plot), K is the adsorption coefficient of the dye, C is the dye concentration at any time t.

For the 2D $PbMoO_4$ and 2D MoO_{3-x} photocatalysts, the calculated values of rate of reaction (r) are 90 μgL^{-1}min^{-1} and 38 μgL^{-1}min^{-1}, respectively, which signifies the importance of 2D $PbMoO_4$ in dye degradation.

The presence of trap states effectively reduces the bandgap of 2D $PbMoO_4$, making it feasible for the solar light driven photocatalytic experiment. The suitable band position of $PbMoO_4$ for dye degradation also plays a significant role that increases the photocatalytic performance

of 2D PbMoO$_4$.[22, 23] This is also evident in the band structure diagram presented in **Figure** 4.7. The estimated CBM position of 2D PbMoO$_4$ nanosheets suggests that the minimal driving force is required to produce superoxide (O$_2^{-\bullet}$) radicals. Eventually, these radicals play a significant role for decomposing the organic dye RhB. The CBM and VBM of 2D PbMoO$_4$ nanosheets are determined by the d^0/p^2 electron orbit of Mo^{6+}/Pb^{2+} and the O$_{2p}$ electron orbital, respectively.[23] After solar light illumination, the strong polarization of Pb^{2+} and Mo^{6+} trigger the charge transfer between O^{2-} ions and Mo^{6+}/Pb^{2+} ions and facilitates the photocatalytic dye degradation process.[23] The significant improvement in photocatalytic activity of the 2D PbMoO$_4$ nanosheets can also be attributed to its 2D features. The ultrathin facets of 2D nanosheets which provides high surface area and is also rich in dangling bonds facilitate reaction active sites.[40] Steps of the basal surface (steps presented in AFM characterisation, **Figure** 4.2e) also contribute to the enhanced active sites. In order to determine the specific surface area of the 2D PbMoO$_4$ nanosheets, the samples were tested using N$_2$ adsorption–desorption isotherms by the Brunauer–Emmett–Teller (BET) method. The surface area of the prepared 2D PbMoO$_4$ was found to be 45.23 m^2/g, based on the isotherm displayed in **Figure** 4.14. This value is higher compared to the previously reported surface areas of PbMoO$_4$ of various morphologies. The comparative analysis is summarized in Table 1.
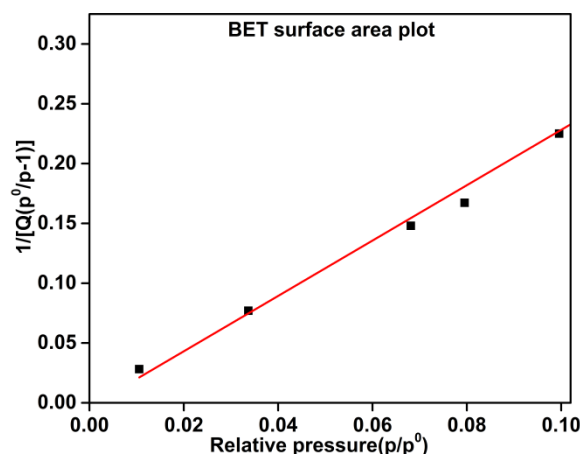
Figure 4.14. BET surface area plot of 2D PbMoO$_4$ nanosheets.

In order to ensure the safety of using a material with Pb in its structure, ICP-MS was conducted. The synthesized 2D PbMoO$_4$ nanosheets was further filtered and separated using high speed centrifugation and the solvent (Milli-Q water) was analyzed using the ICP-MS. Only 0.3 ppb concentration of Pb was found in the solvent, which is well-below the standard levels of wastewater discharge and also below the standard limits set by WHO for drinking water.[12, 47] The stability of the 2D PbMoO$_4$ nanosheets in photocatalytic test was further investigated using Raman spectroscopy. **Figure** 4.15a, b compares the Raman spectra obtained before and after the photocatalytic experiment, which shows no structural change occurred in 2D PbMoO$_4$ nanosheets after the degradation of RhB molecules. These results indicate the high stability, safety and promise of 2D PbMoO$_4$ nanosheets in photocatalytic degradation of organic pollutants. In contrast, a newly appeared broad peak centred at 953 cm^{-1} was observed for the 2D α-MoO$_{3-x}$ nanosheets after the photocatalysis process (see **Figure** 4.15c, d), which signifies the possible vibrational change on the surface of this material and shows its instability in the photocatalytic process.
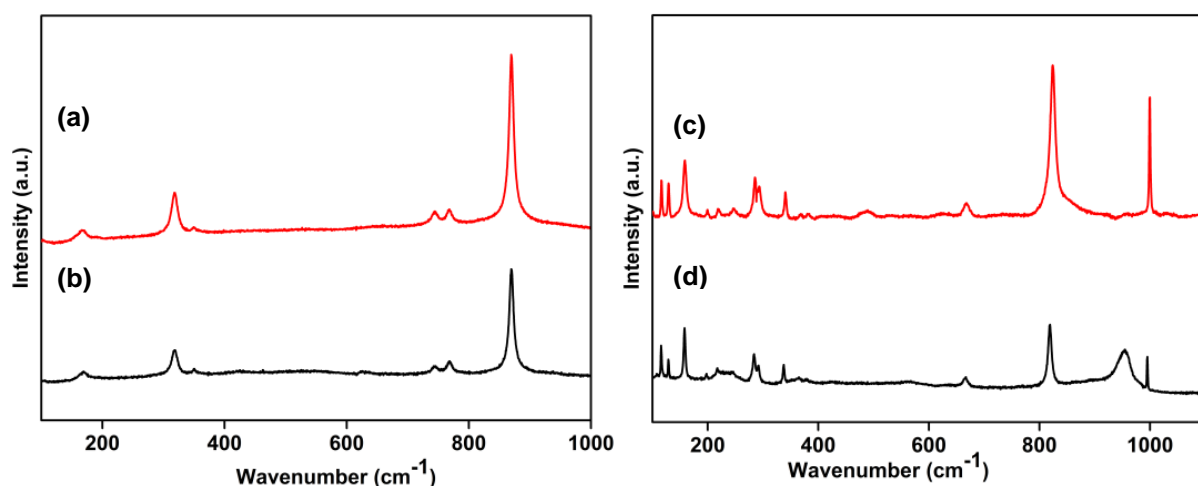
Figure 4.15. Raman spectra of 2D $PbMoO_4$ (a) before and (b) after RhB degradation, and Raman spectra of 2D MoO_{3-x} (c) before and (d) after RhB degradation.

4.4. Conclusion

Despite the fundamental restriction that non-stratified metal molybdates do not have a natural inclination to form 2D morphologies, here an approach for synthesizing of 2D $PbMoO_4$ nanosheets is demonstrated. A facile and room temperature two-step method is applied to synthesize 2D $PbMoO_4$ from 2D α-MoO_{3-x} nanosheets *via* structural transformation by infusing Pb^{2+} ions in an aqueous solution. The 2D nanosheets are on average ~5.1 nm thick with lateral dimensions of ~120 nm, leading to an aspect ratio of ~25. Morphological and structural characterizations confirm that the synthesized 2D nanosheets were scheelite type $PbMoO_4$ crystals that adopted the 2D morphologies of 2D α-MoO_{3-x}. The electronic band structure revealed that the 2D $PbMoO_4$ nanosheets were shown to belong to the wide bandgap semiconductor family with the value of 3.4 eV and favourable band positions for photocatalysis. However, the presence of trap states within the bandgap made it available for solar light absorption. 2D $PbMoO_4$ is further employed for photocatalytic degradation of an organic dye, where this 2D material outperformed the previously reported morphologies of

$PbMoO_4$ due to the high area of the 2D nanosheets and the presence of trap states. This suggests the high potential of the synthesized 2D metal molybdate nanosheets in various photocatalytic applications.

This finding constitutes the first system in which a non-stratified scheelite-type metal molybdate was synthesized into 2D nanosheets. ICP-MS measurement confirmed the environmental safety of this synthesis material. Thus, it is believed that the demonstrated approach could be suitable for synthesizing a range of metal molybdates into 2D form. This work should lead to the possibility of incorporating metal molybdates in a number of future applications.

4.5. References

1. Bomio, M.R.D. et al. Toward Understanding the Photocatalytic Activity of $PbMoO_4$ Powders with Predominant (111), (100), (011), and (110) Facets. A Combined Experimental and Theoretical Study. *J. Phys. Chem. C* **117**, 21382-21395 (2013).

2. Mai, L.-Q. et al. Hierarchical $MnMoO_4$/$CoMoO_4$ Heterostructured Nanowires with Enhanced Supercapacitor Performance. *Nat. Commun.* **2**, 381 (2011).

3. Zhang, Z. et al. Facile Hydrothermal Synthesis of $NiMoO_4$@$CoMoO_4$ Hierarchical Nanospheres for Supercapacitor Applications. *Phys. Chem. Chem. Phys.* **17**, 20795-20804 (2015).

4. Xiao, W., Chen, J.S., Li, C.M., Xu, R. & Lou, X.W. Synthesis, Characterization, and Lithium Storage Capability of $AMoO_4$ (A = Ni, Co) Nanorods. *Chem. Mater.* **22**, 746-754 (2010).

5. Mikhailik, V.B. & Kraus, H. Performance of Scintillation Materials at Cryogenic Temperatures. *Phys. Status Solidi B* **247**, 1583-1599 (2010).

6.   Mikhailik, V.B. et al. Structure, Luminescence and Scintillation Properties of the MgWO$_4$–MgMoO$_4$ System. *J. Phys. Condens. Matter* **20**, 365219 (2008).

7.   Zhen, L. et al. High Photocatalytic Activity and Photoluminescence Property of Hollow CdMoO$_4$ Microspheres. *Scr. Mater.* **58**, 461-464 (2008).

8.   Sczancoski, J.C. et al. Morphology and Blue Photoluminescence Emission of PbMoO$_4$ Processed in Conventional Hydrothermal. *J. Phys. Chem. C* **113**, 5812-5822 (2009).

9.   Kajitani, T. & Itoh, M. Time-Resolved Composite Nature of the Self-Trapped Exciton Luminescence in PbMoO$_4$. *Phys. Status Solidi C* **8**, 108-111 (2011).

10.   Sundaram, R. & Nagaraja, K.S. Solid State Electrical Conductivity and Humidity Sensing Studies on Metal Molybdate–Molybdenum Trioxide Composites (M = Ni^{2+}, Cu^{2+} and Pb^{2+}). *Sens. Actuator B-Chem.* **101**, 353-360 (2004).

11.   Yan, X. et al. Converting CoMoO$_4$ into CoO/MoO$_x$ for Overall Water Splitting by Hydrogenation. *ACS Sustain. Chem. Eng.* **4**, 3743-3749 (2016).

12.   Hernández-Uresti, D.B., Martínez-de la Cruz, A. & Aguilar-Garib, J.A. Photocatalytic Activity of PbMoO$_4$ Molybdate Synthesized by Microwave Method. *Catal. Today* **212**, 70-74 (2013).

13.   Kwolek, P. et al. Lead Molybdate - a Promising Material for Optoelectronics and Photocatalysis. *J. Mater. Chem. C* **3**, 2614-2623 (2015).

14.   Kato, H., Matsudo, N. & Kudo, A. Photophysical and Photocatalytic Properties of Molybdates and Tungstates with a Scheelite Structure. *Chem. Lett.* **33**, 1216-1217 (2004).

15.   Zhang, Y., Holzwarth, N.A.W. & Williams, R.T. Electronic Band Structures of the Scheelite Materials CaMoO$_4$, CaWO$_4$, PbMoO$_4$, and PbWO$_4$. *Phys. Rev. B* **57**, 12738-12750 (1998).

16. Groenink, J.A. & Blasse, G. Some New Observations on the Luminescence of PbMoO$_4$ and PbWO$_4$. *J. Solid State Chem.* **32**, 9-20 (1980).

17. Senguttuvan, N., Babu, S.M. & Subramanian, C. Synthesis, Crystal Growth and Mechanical Properties of Lead Molybdate. *Mater. Sci. Eng., B* **47**, 269-273 (1997).

18. Errandonea, D., Santamaria-Perez, D., Grover, V., Achary, S.N. & Tyagi, A.K. High-Pressure X-Ray Diffraction Study of Bulk and Nanocrystalline PbMoO$_4$. *J. Appl. Phys.* **108**, 073518 (2010).

19. Kudo, A. et al. Photoactivity of Ternary Lead-Group IV B Oxides for Hydrogen and Oxygen Evolution. *Catal. Lett.* **5**, 61-66 (1990).

20. Spassky, D.A. et al. Optical and Luminescent Properties of the Lead and Barium Molybdates. *Radiat. Meas.* **38**, 607-610 (2004).

21. Kunkel, K., Milke, E. & Binnewies, M. Formation of Ternary Lead-Molybdenum Oxides PbMoO$_4$, PbMo$_2$O$_7$, Pb$_2$MoO$_5$ and PbMo$_3$O$_{10}$ in the Gas Phase: A Mass Spectrometric and Quantum Chemical Investigation. *Int. J. Mass spectrom.* **374**, 12-19 (2014).

22. Dai, K. et al. Enhancing the Photocatalytic Activity of Lead Molybdate by Modifying with Fullerene. *J. Mol. Catal. A: Chem.* **374-375**, 111-117 (2013).

23. Du, W. et al. Black Lead Molybdate Nanoparticles: Facile Synthesis and Photocatalytic Properties Responding to Visible Light. *Appl. Surf. Sci.* **328**, 428-435 (2015).

24. Hernández-Uresti, D.B., Martínez-de la Cruz, A. & Torres-Martínez, L.M. Photocatalytic Properties of PbMoO$_4$ Synthesized by Co-Precipitation Method: Organic Dyes Degradation Under UV Irradiation. *Res. Chem. Intermed.* **38**, 817-828 (2012).

25.   Martínez-de la Cruz, A., Hernández-Uresti, D.B., Torres-Martínez, L.M. & Lee, S.W. Photocatalytic Properties of PbMoO$_4$ synthesized by a Hydrothermal Reaction. *React. Kinet. Mech. Cat.* **107**, 467-475 (2012).

26.   Zeng, H.C. Synthesis of Stoichiometric Lead Molybdate PbMoO$_4$: An X-Ray Diffraction, Fourier Transform Infrared Spectroscopy, and Differential Thermal Analysis Study. *J. Mater. Res.* **11**, 703-715 (2011).

27.   Xing, G.-J. et al. Photoluminescence and Photocatalytic Properties of Uniform PbMoO$_4$ Polyhedral Crystals Synthesized by Microemulsion-Based Solvothermal Method. *Ceram. Int.* **37**, 2951-2956 (2011).

28.   Zeng, H.C. Rectangular Vacancy Island Formation and Self-Depletion in Czochralski-Grown PbMoO$_4$ Single Crystal During Heat Treatment. *J. Cryst. Growth* **160**, 119-128 (1996).

29.   Kim, T.-H. et al. Synthesis of TiO$_{2-x}$N$_y$/Ag–PbMoO$_4$ Nanocomposites: An Effective Approach for Photoinactivation of Green Tide Under Simulated Solar Light. *Mater. Lett.* **101**, 99-102 (2013).

30.   Wang, L., Tang, H. & Tian, Y. Carbon-Shell-Decorated p-Semiconductor PbMoO$_4$ Nanocrystals for Efficient and Stable Photocathode of Photoelectrochemical Water Reduction. *J. Power Sources* **319**, 210-218 (2016).

31.   Phuruangrat, A., Thongtem, T. & Thongtem, S. Synthesis of Lead Molybdate and Lead Tungstate *via* Microwave Irradiation Method. *J. Cryst. Growth* **311**, 4076-4081 (2009).

32.   de Castro, I.A. et al. Molybdenum Oxides – From Fundamentals to Functionality. *Adv. Mater.*, 1701619 (2017).

33.   Nicolosi, V., Chhowalla, M., Kanatzidis, M.G., Strano, M.S. & Coleman, J.N. Liquid Exfoliation of Layered Materials. *Science* **340** (2013).

34. Coleman, J.N. et al. Two-Dimensional Nanosheets Produced by Liquid Exfoliation of Layered Materials. *Science* **331**, 568 (2011).

35. Balendhran, S. et al. Two-Dimensional Molybdenum Trioxide and Dichalcogenides. *Adv. Funct. Mater.* **23**, 3952-3970 (2013).

36. Mayorga-Martinez, C.C., Sofer, Z. & Pumera, M. Layered Black Phosphorus as a Selective Vapor Sensor. *Angew. Chem. Int. Ed.* **54**, 14317-14320 (2015).

37. Mayorga-Martinez, C.C., Ambrosi, A., Eng, A.Y.S., Sofer, Z. & Pumera, M. Metallic 1T-WS2 for Selective Impedimetric Vapor Sensing. *Adv. Funct. Mater.* **25**, 5611-5616 (2015).

38. Alsaif, M.M.Y.A. et al. Tunable Plasmon Resonances in Two-Dimensional Molybdenum Oxide Nanoflakes. *Adv. Mater.* **26**, 3931-3937 (2014).

39. Alsaif, M.M.Y.A. et al. High-Performance Field Effect Transistors Using Electronic Inks of 2D Molybdenum Oxide Nanoflakes. *Adv. Funct. Mater.* **26**, 91-100 (2016).

40. Datta, R.S. et al. Highly Active Two Dimensional □-MoO_{3-x} for the Electrocatalytic Hydrogen Evolution Reaction. *J. Mater. Chem. A*, 10.1039/C7TA07705J (2017).

41. Hanlon, D. et al. Production of Molybdenum Trioxide Nanosheets by Liquid Exfoliation and Their Application in High-Performance Supercapacitors. *Chem. Mater.* **26**, 1751-1763 (2014).

42. Carey, B.J. et al. Two Solvent Grinding Sonication Method for the Synthesis of Two-Dimensional Tungsten Disulphide Flakes. *Chem. Commun.* **51**, 3770-3773 (2015).

43. Huang, J. et al. Pb (II) Removal from Aqueous Media by EDTA-Modified Mesoporous Silica SBA-15. *J. Colloid Interface Sci.* **385**, 137-146 (2012).

44. Kalantar-zadeh, K. et al. Synthesis of nanometre-thick MoO_3 sheets. *Nanoscale* **2**, 429-433 (2010).

45. Luo, Z. et al. Mesoporous MoO_{3-x} Material as an Efficient Electrocatalyst for Hydrogen Evolution Reactions. *Adv. Energy Mater.* **6**, 1600528 (2016).

46. Tan, X. et al. Plasmonic MoO_{3-x}@MoO_3 nanosheets for highly sensitive SERS detection through nanoshell-isolated electromagnetic enhancement. *Chem. Commun.* **52**, 2893-2896 (2016).

47. Wu, Y. et al. High Efficient and Selective Removal of Pb^{2+} Through Formation of Lead Molybdate on α-MoO_3 Porous Nanosheets Array. *J. Colloid Interface Sci.* **491**, 80-88 (2017).

48. Chu, H. et al. Inorganic Hierarchical Nanostructures Induced by Concentration Difference and Gradient. *Nano Res.* **1**, 213-220 (2008).

49. Gyawali, G., Joshi, B. & Lee, S.W. Sonochemical Synthesis, Characterization, and Photocatalytic Activities of $PbMoO_4$ Photocatalyst. *J. Ceram. Process Res.* **17**, 235-239 (2016).

50. Pederson, L.R. Two-Dimensional Chemical-State Plot for Lead Using XPS. *J. Electron Spectrosc. Relat. Phenom.* **28**, 203-209 (1982).

51. Kim, K.S., O'Leary, T.J. & Winograd, N. X-Ray Photoelectron Spectra of Lead Oxides. *Anal. Chem.* **45**, 2214-2218 (1973).

52. Li, J.-S. et al. Coupled Molybdenum Carbide and Reduced Graphene Oxide Electrocatalysts for Efficient Hydrogen Evolution. *Nat. Commun.* **7**, 11204 (2016).

53. Walck, S.D., Donley, M.S., Zabinski, J.S. & Dyhouse, V.J. Characterization of Pulsed Laser Deposited PbO/MoS_2 by Transmission Electron Microscopy. *J. Mater. Res.* **9**, 236-245 (2011).

54. Mestl, G., Ruiz, P., Delmon, B. & Knozinger, H. Oxygen-Exchange Properties of MoO_3: An in Situ Raman Spectroscopy Study. *J. Phys. Chem.* **98**, 11269-11275 (1994).

55. Zhang, L., Bai, D., Zhou, M. & Pan, C. Surfactant-Free Hydrothermal Synthesis, Growth Mechanism and Photocatalytic Properties of $PbMoO_4$ Polyhedron Microcrystals. *J. Saudi Chem. Soc.* **21**, S275-S282 (2017).

56. R. Vilaplana, O.G., F. J. Manjón, P. Rodríguez-Hernández, A. Muñoz, D. Errandonea, S. N. Achary, and A. K. Tyagi. Raman Scattering Study of Bulk and Nanocrystalline $PbMoO_4$ at High Pressures. *J. Appl. Phys.* **112**, 103510 (2012).

57. Bomio, M.R.D. et al. Structural Refinement, Growth Mechanism, Infrared/Raman Spectroscopies and Photoluminescence Properties of $PbMoO_4$ Crystals. *Polyhedron* **50**, 532-545 (2013).

58. Khanna, R.K. & Lippincott, E.R. Infrared Spectra of Some Scheelite Structures. *Spectrochim. Acta A* **24**, 905-908 (1968).

59. Gyawali, G. et al. Sonochemical Synthesis of Solar-Light-Driven $A\mathring{g}$-$PbMoO_4$ Photocatalyst. *J. Hazard. Mater.* **263, Part 1**, 45-51 (2013).

60. Alsaif, M.M.Y.A. et al. Two Dimensional α-MoO_3 Nanoflakes Obtained Using Solvent-Assisted Grinding and Sonication Method: Application for H_2 Gas Sensing. *Sens Actuator B Chem* **192**, 196-204 (2014).

61. Shen, M., Zhang, Q., Chen, H. & Peng, T. Hydrothermal Fabrication of $PbMoO_4$ Microcrystals with Exposed (001) Facets and its Enhanced Photocatalytic Properties. *CrystEngComm.* **13**, 2785-2791 (2011).

62. Shen, M., Zhang, X., Dai, K., Chen, H. & Peng, T. Hierarchical $PbMoO_4$ Microspheres: Hydrothermal Synthesis, Formation Mechanism and Photocatalytic Properties. *CrystEngComm.* **15**, 1146-1152 (2013).

63. Syed, N. et al. Sonication-Assisted Synthesis of Gallium Oxide Suspensions Featuring Trap State Absorption: Test of Photochemistry. *Adv. Funct. Mater.* **27**, 1702295-n/a (2017).

64. Hu, Z., Xu, M., Shen, Z. & Yu, J.C. A Nanostructured Chromium(Iii) Oxide/Tungsten(Vi) Oxide p-n Junction Photoanode Toward Enhanced Efficiency for Water Oxidation. *J. Mater. Chem. A* **3**, 14046-14053 (2015).

65. Yue, D. et al. Enhanced Photocatalytic Performance and Morphology Evolvement of PbWO$_4$ Dendritic Nanostructures Through Eu^{3+} Doping. *RSC Adv.* **6**, 81447-81453 (2016).

66. Wang, X. et al. Tandem Colloidal Quantum Dot Solar Cells Employing a Graded Recombination Layer. *Nat. Photonics* **5**, 480 (2011).

67. Jin, Y. et al. Highly Efficient Degradation of Dye Pollutants by Ce-Doped MoO$_3$ Catalyst at Room Temperature. *Dalton Trans.* **43**, 12860-12870 (2014).

68. Navgire, M.E. & Lande, M.K. Effect of Nanocrystalline Composite Fullerene-Doped MoO$_3$-TiO$_2$ Material on Photoassisted Degradation of Alizarin Red S Dye. *Inorg. Nano-Met. Chem.* **47**, 320-327 (2017).

69. Chithambararaj, A., Sanjini, N.S., Velmathi, S. & Chandra Bose, A. Preparation of h-MoO$_3$ and □-MoO$_3$ Nanocrystals: Comparative Study on Photocatalytic Degradation of Methylene Blue Under Visible Light Irradiation. *Phys. Chem. Chem. Phys.* **15**, 14761-14769 (2013).

70. Cherian, S. & Wamser, C.C. Adsorption and Photoactivity of Tetra(4-carboxyphenyl)porphyrin (TCPP) on Nanoparticulate TiO$_2$. *J. Phys. Chem. B* **104**, 3624-3629 (2000).

71. Kalantar-zadeh, K. et al. Two Dimensional and Layered Transition Metal Oxides. *Appl. Mater. Today* **5**, 73-89 (2016).

72. Saraf, R., Shivakumara, C., Behera, S., Nagabhushana, H. & Dhananjaya, N. Facile Synthesis of PbWO$_4$: Applications in Photoluminescence and Photocatalytic

Degradation of Organic Dyes Under Visible Light. *Spectrochim. Acta A* **136**, 348-355 (2015).

73. Loghambal, S., Agvinos Catherine, A. J., Velu Subash, S. Analysis of Langmuir-Hinshelwood Kinetics Model for Photocatalytic Degradation of Aqueous Direct Blue 71 Through Analytical Expression. *Int. J. Math. And Appl.*, **6(1–E),** 903–913, (2018).

Chapter 5

Liquid metal derived ultrathin, highly flexible and large area printable two-dimensional ITO

5.1. Introduction

Transparent conductive oxides (TCOs) are a class of materials that gained tremendous economic importance due to their unique electronic band structure that enables high conductivity, while simultaneously rendering the material transparent in the visible range.[1-3] The high transparency of TCOs originates from a pronounced Moss-Burstein shift that leads to optical bandgaps substantially wider than the electronic gap.[1] TCOs are mostly used as transparent electrodes in display technologies.[2] These materials have also shown remarkable performance in other applications such as low emission windows,[3-5] a variety of optoelectronic devices,[6] solar cells,[1, 3, 7] plasmonics[8-10] and lab-on-a-chip biosensing.[11]

Tin doped indium oxide (ITO) is one of the most important TCOs due to its excellent performance and the substantial developed knowledge base associated with its industrial use over several decades.[12] Physical vapour-based depositions are the commonly practiced techniques to deposit ITO, which rely on vacuum technology and batch processing.[2, 3, 13-15] This increases the production costs and also adds complexity to the entire process. In

addition, the typical film thickness of the deposited ITO is in the range of 50 to 500 nm, which is still not suitable to overcome the brittle nature of this material and thus incompatible with flexible electronics.[16]

In response to these challenges, this chapter focuses on developing a scalable, low cost and low temperature printable synthesis method that allows creating ultrathin two dimensional (2D) ITO nanosheets with a thickness of only a few atoms at wafer scales. Reducing the thickness of a ceramic material to only a few atoms is known to substantially increase the material's flexibility,[17] allowing to overcome one of the most limiting properties of ITO. The developed ITO nanosheets are highly conductive and flexible, while absorbing significantly less light than graphene in the visible spectrum.

5.2. Materials and Methods

5.2.1. Materials

Indium (In, 99.98%) and tin (Sn, 99.8%) were purchased from Roto Metals. All other chemicals were purchased from Sigma Aldrich. All materials were used as received.

5.2.2. Synthesis of large area ultrathin 2D ITO using the squeeze-printing process

The In-Sn alloys were synthesized using various Sn concentrations (between 0 and 20 at%). All alloys were prepared by melting the precursor metals inside a glass vial on a hot plate at 200°C for 30 min. Homogeneous alloys without any solid tin inclusions were obtained for all compositions.

During the printing process, a liquid droplet of the synthesized alloy (size ~1 to ~5 mm) was placed on a desired substrate (*e.g.* glass, quartz, SiO_2/Si wafers, polyimide film) using a glass Pasteur pipette, with the substrate and alloy droplet being heated to 200°C, which is above

the melting point of all alloys (**Figure** 5.1a). A second substrate (pre-heated to 200°C) was used to press onto the centre of the droplet to spread the liquid alloy homogeneously between the two substrates (**Figure** 5.1b). The synthesis was conducted in ambient air and the squeezing process would be conducted within 2 minutes after placing the droplet onto the bottom substrate. An excessive pressure during the squeezing step can break or laterally slide the substrate, which is detrimental to obtain large homogeneous 2D nanosheet. After the squeezing step, the top substrate is vertically lifted and separated in a fast but deliberate motion, avoiding any lateral slip. Using this technique, homogeneous ultra-thin ITO sheets could be exfoliated onto both substrates. The strong van der Waals bond between the liquid metal's oxide skin and the substrate facilitates the delamination of the oxide. Metal inclusions attached to the exfoliated sheets could be removed using a solvent assisted cleaning method explained below. Using this method, large area 2D ITO sheets, exceeding several centimetres in lateral dimension could be efficiently prepared.

5.2.3. *Mechanical cleaning procedure*

A facile mechanical washing process using ethanol was used to eliminate any liquid metal inclusions left on the surface of the ITO samples that were printed onto SiO_2/Si wafers. During the cleaning procedure, a beaker was filled with ethanol and heated to boiling. The samples on SiO_2/Si were submerged in the hot ethanol with the aid of tweezers. After 1 min, the metal inclusions in the exfoliated 2D ITO sheet could be completely eliminated by gently rubbing the submerged SiO_2/Si wafer with a soft, lint-free wiping tool (*i.e.* lint-free cotton bud). The ITO sheets were found to be firmly attached to the silicon oxide surface due to strong van der Waals adhesion between ITO sheets and the substrate and remained intact throughout the cleaning procedure.

The van der Waals adhesion of the 2D ITO sheets was found to be comparatively weak when polymer substrates such as polyimide were used. Therefore, the above mentioned procedure

was slightly modified to remove the metal inclusions for these samples. The soft wiping tool was dipped inside the hot ethanol and then delicately wiped across the surface of the exfoliated 2D sheets. Due to considerably weaker attachment of the metal particles to the polyimide sheet, the metal inclusions could be easily removed without damaging the 2D ITO sheets.

5.2.4. Chemical cleaning procedure

Substrates such as glass and quartz were found to show weaker van der Waals adhesion of the 2D ITO when compared to the SiO_2/Si wafers. Therefore, a chemical cleaning process was applied to remove the metal inclusions. An iodide/triiodide solution (I^-/I^{3-}; containing 100 mmol L^{-1} LiI and 5 mmol L^{-1} I_2) was prepared in ethanol and heated to 50°C on a hotplate. The substrates coated with 2D ITO were submerged into the heated I^-/I^{3-} solution and kept overnight to completely remove any metal inclusions. The samples were then washed in deionised water to remove any residual etchant.

5.2.5. Characterizations

XPS analysis was conducted on samples synthesized on SiO_2/Si substrates. A Thermo Scientific K-alpha XPS spectrometer equipped with a monochromatic Al Kα source (hν = ~1486.6 eV) was utilized for this measurement. A concentric hemispherical analyser (CHA) was utilized to evaluate the chemical composition of the synthesized 2D ITO sheets with varying Sn at% concentrations. The core-level spectra were recorded by applying a pass energy of 100 eV, while a pass energy of 50 eV was used to record the valance band spectrum. Surface charging effects were eliminated by using a low-energy electron flood gun during the measurement. The optical spectra of samples deposited on quartz substrates were recorded using an Agilent Cary 60 Ultraviolet-Visible (UV–Vis) Spectrophotometer. For the transparency measurements, a blank quartz substrate was recorded for comparison. A Bruker Dimension Icon AFM was used to obtain the surface topography and thickness profile of the

2D ITO sheets exfoliated on SiO_2/Si substrate using "Scanasyst-air" AFM tips. Gwyddion 2.36 was utilized for AFM image processing and analysis. The low-resolution TEM measurements were performed using a JEOL 2100F microscope operated at an acceleration voltage of 200 kV. Dark field imaging and high-resolution TEM imaging was conducted using a Philips CM200 field emission TEM with an acceleration voltage of 200 kV. TEM image analysis was performed using the Gatan Microscopy Suite 1.8.4. software package. Thermally and mechanically robust carbon type B on Mesh 200 Cu, 25 TEM (purchased from Ted Pella, Inc.) membranes were used to directly print the 2D ITO sheets onto TEM grids. The printing process for the TEM samples entailed briefly and gently touching the liquid metal interface. The TEM grids were not found to require pre-heating.

5.2.6. *Four-point probe measurement*

Four-point probe measurements were utilized to obtain the sheet resistance data of the synthesized 2D ITO sheets on SiO_2/Si substrates. Four equally spaced (200 μm space between each) chromium / gold (10 nm Cr, 100 nm Au) probes were deposited through a shadow mask onto the 2D ITO sheets using a PVD75-Kurt J. Lesker electron-beam evaporator deposition system. A Keysight source meter measuring unit was used to supply a low current (1-5 µA) through the outer probes and the voltage was recorded from the inner probes, in order to determine the sheet resistances of the synthesized 2D ITO sheets of varying Sn at% concentrations.

5.2.7. *Fabrication of LED circuit*

In order to showcase the conductivity of the transparent 2D ITO sheets exfoliated onto glass substrates, a simple circuit was designed and fabricated using a shadow mask and e-beam deposition of chromium / gold electrodes (10 nm Cr, 100 nm Au) (see **Figure** 5.1d). A large area 2D ITO sheet was exfoliated onto a glass substrate using the squeeze-printing process followed by the above described chemical cleaning process. The electrode pattern was

designed and deposited onto the 2D ITO sheets in such a way that the transparent 2D sheets close the LED circuit. An appropriate potential (5 V) was applied to turn on the LED.

5.2.8. *Fabrication of flexible device*

2D ITO was deposited onto polyimide sheets using the method described above. Two chromium / gold contacts (5 nm Cr, 50 nm Au) were placed at 1 mm distance onto the 2D ITO sheets. The device was then subjected to mechanically bending to a radius 3 mm, 2.5 mm, and 2 mm, respectively, for 1000 bending cycles. The changes in resistances were recorded after set numbers of bending cycles using a FLUKE 116 multimeter.

5.2.9. *Fabrication of touch screen device and touch screen characterization*

The capacitive touch screen device was fabricated using two large area (~3 cm) printed ITO sheets that were deposited onto two sides of a single glass substrate (1 mm thick) (**Figure** 5.12). Care was taken to ensure that both ITO sheets occupied opposing sides of the substrate, ensuring good overlap. Four chromium / gold (10 nm Cr, 100 nm Au) electrodes were deposited in a 1 by 1 cm square arrangement on the front side of the touch screen, while a single electrode was deposited to the back side using electron-beam evaporation. The entire front side of the device was then covered using a thin PET film that was physically adhered to the surface. An AC signal was then applied between one of the front electrodes and the back electrode using a network analyser (HP4195A). The capacitive change (ΔC) was recorded once a conductive object such as a finger or a metal pin is brought into close vicinity of the front side of the device. A 3 x 3 pixel test pattern was followed and the response for each pixel was recorded for each of the four front electrodes.

5.3. Results and discussions

The developed process utilizes low melting indium-tin alloys that can be applied in a liquid metal printing process, depositing 2D ITO on wafer scales.[18-21] Liquid metals have been recently introduced as a reaction medium that facilitates the formation of large area 2D oxides.[18-23] Low melting point post transition metals such as Ga, In and Sn undergo self-limiting Cabrera-Mott oxidation in air, leading to the formation of nanometre thin surface oxides.[23] If the metal is in its liquid state, adhesion of the surface oxide to the parent metal is minimal, allowing to apply van der Waals transfer techniques for transferring the grown oxide sheet onto desired substrates.[18, 20, 22, 23] When alloys are used, the surface oxide is dominated by the oxide that provides the greatest reduction in free energy.[22] In most cases this leads to the surface oxide of low melting liquid alloys being dominated by a binary oxide. This has been exploited for creating a variety of high quality 2D metal oxides that could be grown on the surface of complex low melting alloys which effectively function as a reaction solvent.[22] Indium-tin alloys constitute an exception, since their surface oxide has been shown to be a ternary compound that contains both indium and tin, with an indium-tin ratio that resembles ITO.[24] The high solubility of tin ions in indium oxide likely allows for the formation of a ternary oxide on the surface of these alloys, leading to ITO being thermodynamically favoured over pure In_2O_3 and SnO_2.[24, 25]

The employed process entails placing a small droplet of the liquid alloy onto a desired substrate, followed by squeezing a second substrate from the top, spreading the droplet to cover the entire desired area (**Figure** 5.1a-c).[20] The rapid nature of the Cabrera-Mott oxidation process in ambient air ensures the formation of a homogenous surface oxide as the metal expands, while the liquid nature of the parent metal allows the surface oxide to achieve conformal contact with the surface, leading to van der Waals attachment. When the two substrates are separated, the liquid droplet reverts into spherical shaped droplets due to the

high surface tension of liquid metal.[20, 23] Any remaining metal inclusions could be removed with a developed cleaning process (refer to Methods), revealing highly transparent oxide sheets on a variety of substrates such as glasses, wafers and polymers. The deposited transparent oxide sheets were found to be conductive, being capable to bridge a gap in a circuit, switching on a light emitting diode (**Figure** 5.1d).
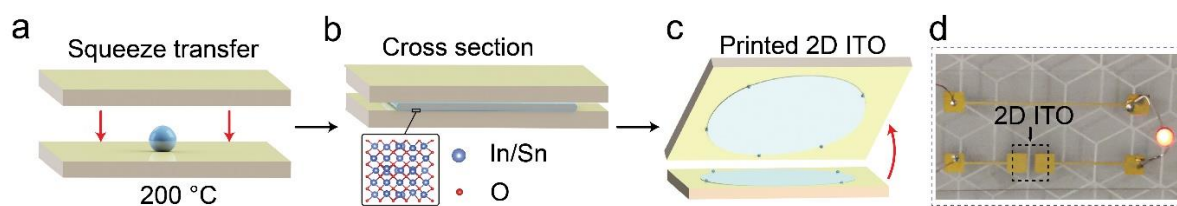
Figure 5.1.   (a) An indium-tin alloy droplet is placed onto a suitable substrate which is heated to 200°C. A second pre-heated substrate is gently pressed from the top. (b) Cross sectional view of the squeezed alloy placed between the two substrates. The liquid metal is pressed into a thin metallic film, with the interfacial surface oxide in conformal contact with the substrates. The crystal structure of ITO is provided in the inset. (c) When the top substrate is lifted, the liquid metal reverts to small spherical droplets due to its high surface tension, revealing large area ITO. (d) Light emitting diode (LED) demonstration circuit utilizing the printed 2D ITO to bridge a gap in the LED power circuit. The 2D ITO is visibly transparent and sufficiently conductive to allow for the LED to be switched on.

A number of different alloy compositions with varying contents of tin were investigated and the sheet resistance was determined using four-point probe measurements. The sheet resistance of the deposited film was observed to first decrease with increasing the tin content, followed by an increasing sheet resistance after a tin concentration of 5 at% is exceeded

(**Figure** 5.2a). X-ray photoelectron spectroscopy (XPS) analysis of the samples revealed that the tin concentration in the oxide is slightly higher than in the parent alloy, likely due to the high solubility of Sn^{4+} ions in In_2O_3, reaching a Sn^{4+} concentration of 7.4 at% (excluding oxygen) for the oxide with the lowest sheet resistance (**Figure** 5.2c, d and **Figure** 5.3a, b). Interestingly, the observed tin-indium ratio in the optimized oxide is comparable to commercial ITO.[25] Furthermore, the XPS spectra confirm the oxidation states of Sn and In as Sn^{4+} and In^{3+}, without the presence of residual metallic (zero valent) inclusions, highlighting that the devised cleaning procedure effectively removed any remaining liquid metal (**Figure** 5.2c, d).[24]
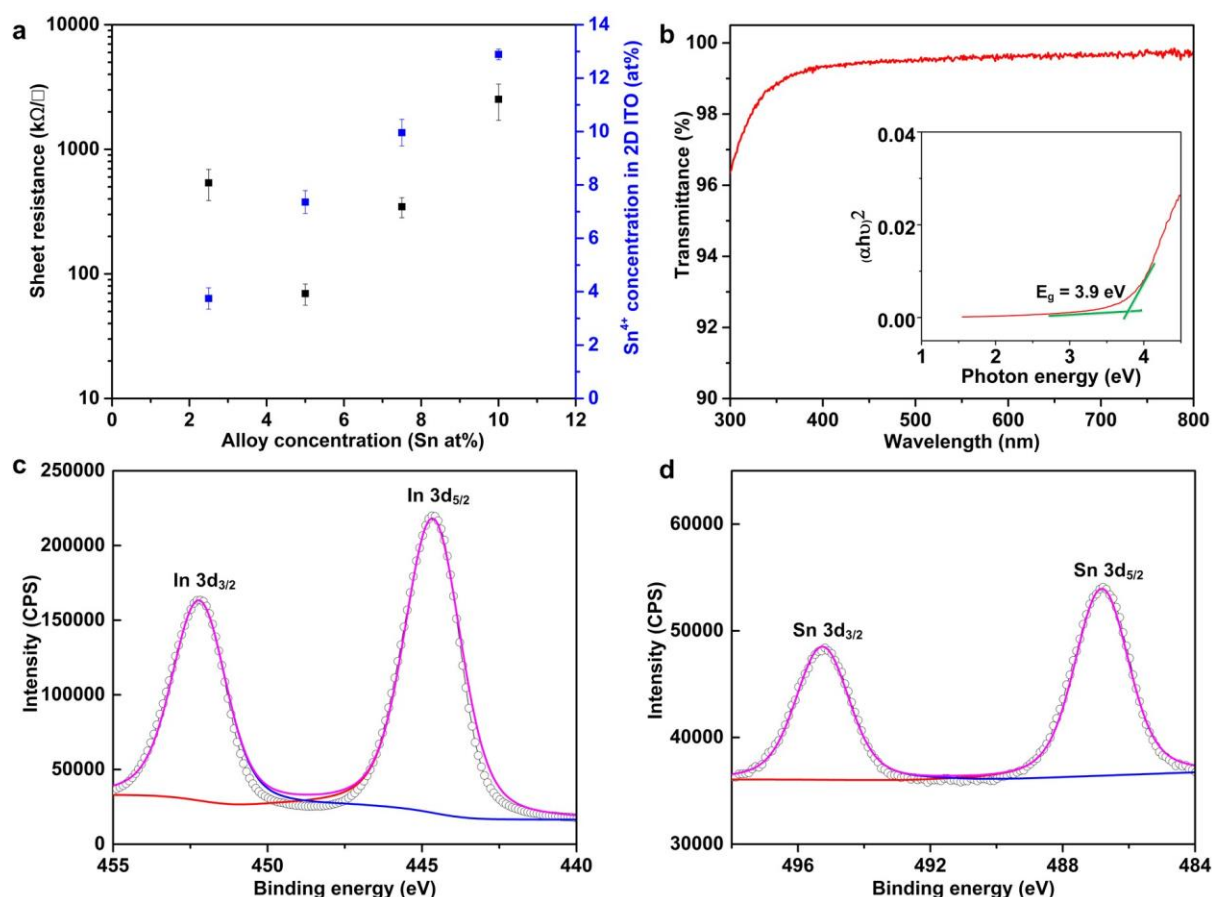
Figure 5.2. (a) Sheet resistance of 2D ITO nanosheets and tin concentration within the oxide layer for different initial alloy compositions. The Sn^{4+} concentration was measured using XPS. In accordance with the wider literature, the calculated at% refers to the cations only and the O^{2-} ions are not included in the composition calculation. (b) UV-vis spectra of 2D ITO deposited onto a quartz substrate. The inset shows the Tauc plot for the ITO sheet. (c) and (d) show the XPS spectra for the optimized ITO nanosheets, showing a single oxidation state for both In and Sn, corresponding well to literature reports of In^{3+} (444.6 eV) and Sn^{4+} (486.7 eV) found in ITO.[24, 26] No elemental In (~443.8 eV) and Sn (~484.9 eV) were detected,[24] highlighting that the synthesis procedure and subsequent workup procedure effectively remove any metallic residues.
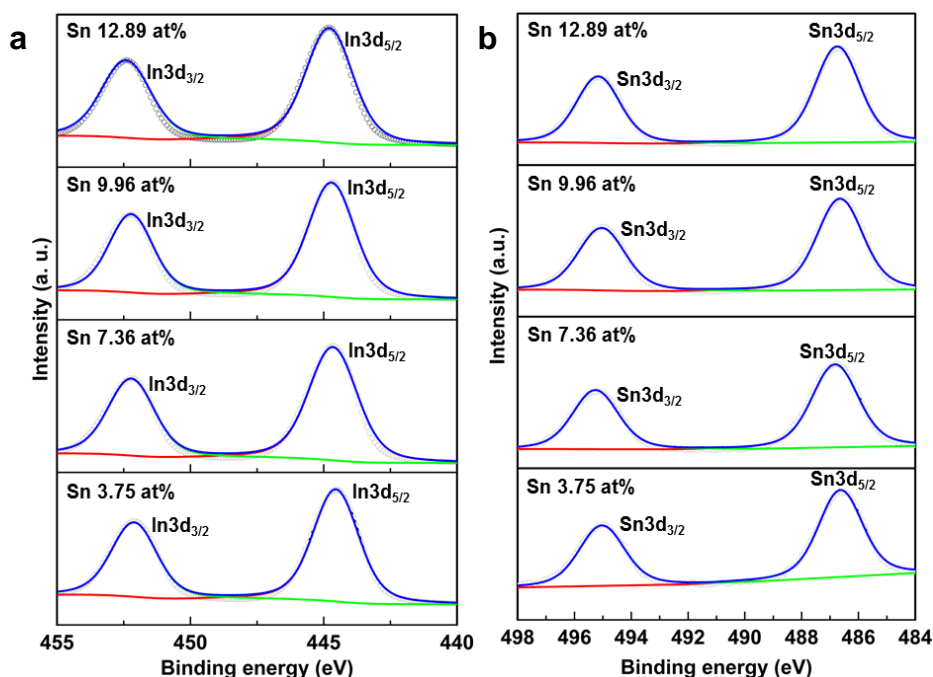
Figure 5.3. (a) In 3d XPS spectra of various Sn doped 2D ITO nanosheets synthesized using squeeze-printing process. The given tin concentration (at%) has been calculated from the XPS spectra of the Sn and In regions and refers to the cations only (oxygen is not included). From top to bottom, the parent alloys contained 10, 7.5, 5 and 2.5% tin in indium and (b) Sn 3d XPS spectra of various Sn doped 2D ITO nanosheets synthesized using squeeze-printing process. The given tin concentration (at%) has been calculated from the XPS spectra of the Sn and In regions and refers to the cations only (oxygen is not included). From top to bottom, the parent alloys contained 10, 7.5, 5 and 2.5% tin in indium.

Optical characterization of a printed 2D sheet on a quartz substrate revealed that the 2D ITO featured minimal absorption across the visible spectrum, leading to a transmittance loss of only ~0.4% for 2D ITO coated substrates (**Figure** 5.2b). Tauc analysis revealed an optical band gap of 3.9 eV, while XPS valance band analysis revealed a closed electronic band gap, which would be expected for a degenerately doped TCO (**Figure** 5.4). As such, the developed 2D ITO is 5.75 times more transparent than state-of-the-art monolayer graphene,[27]

while being roughly 2 orders of magnitude more resistive than state of the art monolayer graphene,[27] rendering the developed 2D ITO a promising alternative when transparency is more critical than having lower sheet resistance. Combining the developed 2D ITO with transparent conductive nanowire networks may reduce the resistance further, while maintaining superior transparency and a continuous conductive interface which is critical for optoelectronic applications in light emitting devices and photovoltaics.[27]
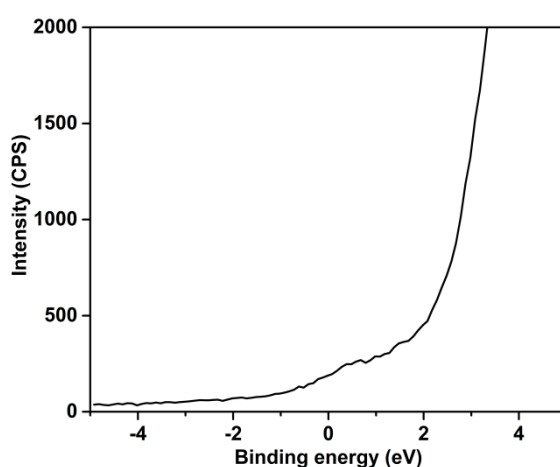
Figure 5.4. XPS valence band spectra of the Sn 7.36 at% doped 2D ITO nanosheets.

Atomic force microscopy (AFM) revealed the thickness of the deposited ITO layer as ~1.1 nm, corresponding to one In_2O_3 unit cell (**Figure** 5.5a).[25] Transmission electron microscopy (TEM) was utilized to investigate the crystallographic properties of 2D ITO. **Figure** 5.5b shows a low magnification image of a typical nanosheet. The sheets were found to be laterally large, continuous, and also remarkably pinhole and crack free with minimal apparent metal inclusions. The translucent appearance of the sheet highlights that the 2D ITO sheets are ultrathin. High resolution TEM (HRTEM) imaging and dark field HRTEM (**Figure** 5.5c, d) were conducted in order to investigate the crystalline properties of 2D ITO further. Nanosheets grown from alloys that contained the optimized tin concentration, leading to the

lowest sheet resistance, featured highly crystalline domains with typical lateral sizes of 25 nm. The colour-enhanced HRTEM image, together with the dark field TEM image highlight that the individual crystals feature varying orientations, with growth along the (110) and (211) facets being dominant. A sample prepared using alloys that contained excessive amounts of tin (20%, **Figure** 5.5d) which is well above the concentration that gave rise to the lowest sheet resistance, was found to be poorly crystalline, featuring small crystalline domains embedded within an amorphous matrix. This is consistent with the XPS elemental analysis, which indicated that the tin content exceeded the solubility limit of Sn in In_2O_3.[24, 25] The excess Sn is then expected to be located at the grain boundaries in the form of tin rich phases which is detrimental to the electronic properties of 2D ITO sheets derived from alloys containing high Sn concentrations (i.e. >5%).[25]
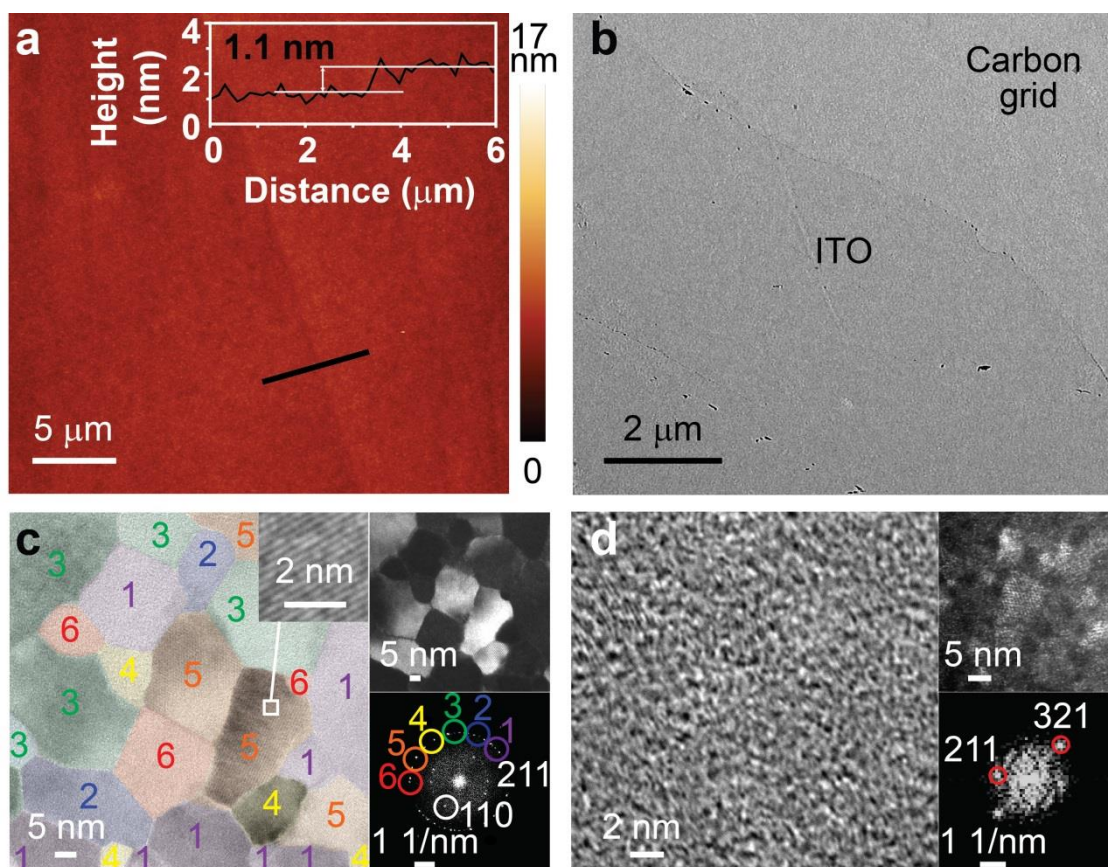
Figure 5.5. (a) AFM image of the 2D nanosheet. The inset shows a height profile recorded at the location indicated by the black line. (b) Low resolution TEM image of an ITO nanosheet printed onto a TEM grid. The sheet is highly translucent in appearance and contained few metallic inclusions. These inclusions are expected to have been removed for samples used for device fabrication and other characterizations during the sample work up procedures described within the Methods section. (c) HRTEM image of the optimized 2D ITO nanosheet. The colour code highlights the crystal orientation based on the fast Fourier transform (FFT) image shown in the lower right inset. The upper left inset shows a magnified view of the lattice pattern and the upper right image shows a dark field image of the region of interest. (d) HRTEM image for an exfoliated 2D sheet containing excessive Sn, showing an amorphous structure with occasional crystalline sections. The upper right inset shows a dark field image of the region of interest, while the lower right inset shows the FFT image.

Due to the low melting point of the liquid alloy, the deposition process was found to be compatible with high temperature resistant polymers such as polyimide. Two terminal resistive devices were fabricated and subjected to repeated mechanical bending to radii of 3, 2.5 and 2.0 mm (**Figure** 5.6). A total of 1000 bending cycles for each radius were applied to a device, and the 2D ITO sheet was subjected to a total of 3000 mechanical bending cycles. Reassuringly, the resistance of the ITO layer only increased by less than 3.5% after 3000 cycles. The small radius of curvature and the robust electronic properties highlight that the developed 2D ITO sheets hold promise for applications in flexible optoelectronic devices and are expected to be compatible with roll-to-roll processing.
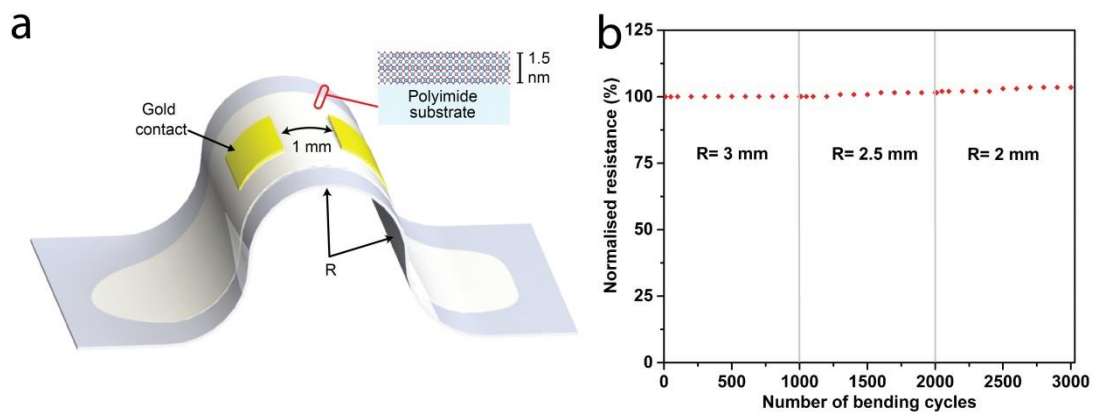
Figure 5.6. (a) Schematic of the developed two terminal resistive test device, with the inset showing the ITO – polymer interface and (b) observed change of the device resistance after repeated bending to the indicated radii. The device was initially bend to the larger radius of curvature for 1000 cycles, followed by subsequently repeating the test after reducing the radius of curvature.

A prototype transparent capacitive touch screen was developed using two centimetre sized printed monolayer ITO sheets that were deposited onto the two sides of a single glass

substrate (**Figure** 5.7). Four gold electrodes were deposited in a square arrangement on the front side of the touch screen, while a single electrode was affixed to the back side. The entire front side of the device was then protected using a thin PET film that was physically adhered to the surface. **Figure** 5.7a shows a photograph and schematic of the device. The PET film acted as both a protective coating and insulator. When an AC signal was applied between one of the front electrodes and the back electrode, the two ITO sheets acted as a plate capacitor, with the glass substrate acting as the dielectric. When a conductive object such as a finger or a metal pin is brought into close vicinity of the front side of the device, the capacitance of the device changed, allowing for efficient touch detection. Here the magnitude of the change in capacitance is dependent on the distance of the touched location from the front electrode (**Figure** 5.7a and c). Measuring the observed change in capacitance for all four electrodes then allows triangulating the position, enabling touch detection with X-Y resolution. **Figure** 5.7c shows the capacitive response maps for each front electrode that were recorded when touching the surface of the PET coated side with a metal pin, following the defined test pattern shown in **Figure** 5.7b. Here, four different measurements were conducted for each configuration (based on front electrode positions) shown in Figure 5.7c, where the bottom electrode was constant at each measurement. The observed capacitance change was found to be highly sensitive to the location where the screen was touched, enabling fully functional X-Y touch screen operation. Similar results were obtained when the device was touched by a human finger (see **Figure** 5.8).
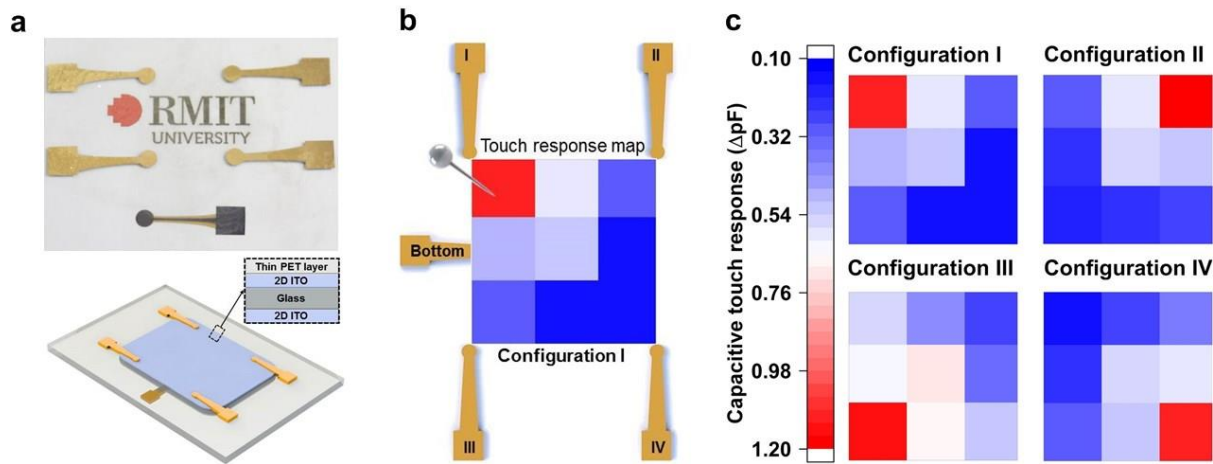
Figure 5.7.   (a) photograph and schematic of the developed device, (b) Test pattern that was utilized to characterize the touch screen. The surface area between the 4 front electrodes was divided into a 3x3 pixel test array. The surface was then gently touched with a metal pin in the centre of each pixel. The measured change in capacitance was determined for each pixel and for each of the four front electrodes, leading to the capacitive touch response maps shown in c) and (c) Capacitive touch response maps for each configuration indicating measurements between the common back electrode and the indicated front electrode. The thickness of glass substrate is 1 mm.
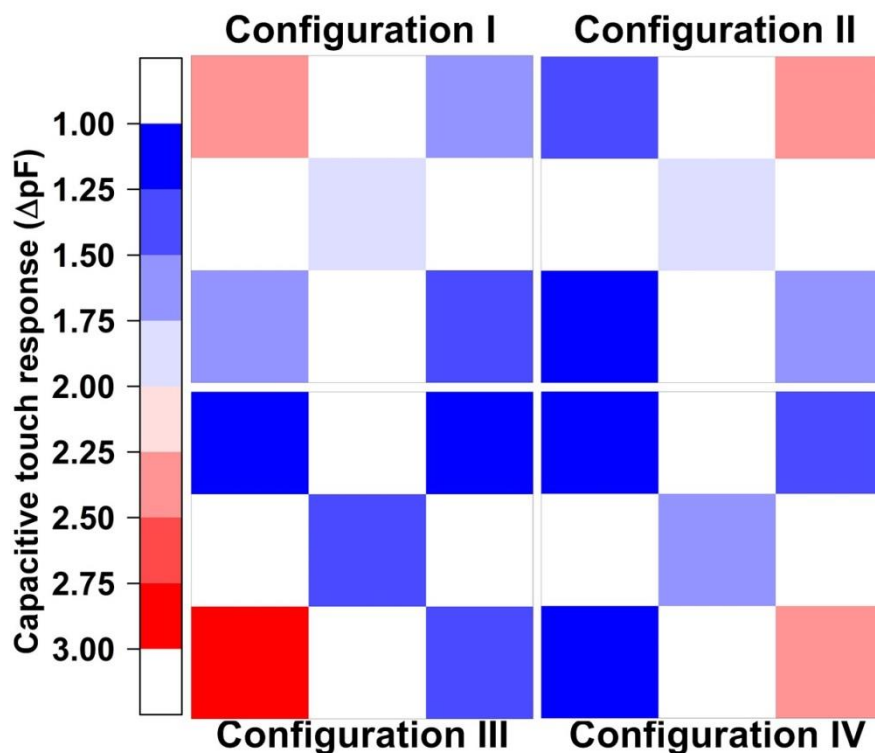
Figure 5.8. Capacitive touch response of the 2D ITO based touch screen to a human finger. Note that a 5 pixel test pattern was used and that the white areas are left blank and were not tested.

5.4. Conclusions

In conclusion, this work describes a novel method that allows printing ultrathin ITO sheets onto desired substrates such as glass, quartz or polymers. The process exploits Cabrera-Mott oxidation that occurs on low melting indium-tin alloys, leading to the self-limiting growth of 2D surface oxides that can be transferred onto solid substrates through van der Waals adhesion. The composition of the parent alloy was found to be crucial, leading to highly crystalline, conductive 2D ITO with a Sn^{4+} concentration of 7.36 at% for the optimized alloy. The developed process leads to centimetre sized 2D nanosheets and may likely be adapted into a continuous printing processes that allows low temperature printing of large area 2D ITO. The process does not require vacuum technology, which is advantageous when

compared with current industrial sputtering techniques and has been demonstrated to be suitable for the fabrication of fully functional capacitive touch screens.

The deposited ITO was found to be ultra-transparent, absorbing less than 0.004% across the visible spectrum, while being electrically conductive. The deposited sheets were only one unit cell thick (~1.1 nm) rendering the ITO to be highly flexible, leading to minimal conductivity loss after 1000 cycles of bending to a radius of 2 mm. This allows overcoming inherent manufacturing challenges that are associated with the brittleness of thicker commercial ITO, holding promise for future roll-to-roll fabrication of optoelectronic devices and the design of ITO based flexible electronics.

The high transparency of 2D ITO exceeds that of graphene by two orders of magnitude, making 2D ITO an attractive choice when high transparency is of greater importance than a low sheet resistance. One such application is capacitive touch screens for handheld devices, where any parasitic light absorption within the transparent conductor directly increases the device's energy consumption and enhances display quality. Ultimately composite structures containing 2D ITO and networks of metal nanowires may be created in order to maintain high transparency and pinhole free conductivity while reducing the sheet resistance even further. Other future applications of 2D ITO include the creation of van der Waals heterostructures where it may replace graphene as a conductor with superior transparency and printability that are highly desirable for future products.

5.5. References

1. Dixon, S.C., Scanlon, D.O., Carmalt, C.J. & Parkin, I.P. n-Type doped transparent conducting binary oxides: an overview. *J. Mater. Chem. C* **4**, 6946-6961 (2016).

2. Zheng, Q. & Kim, J.-K. in Graphene for Transparent Conductors: Synthesis, Properties and Applications (eds. Zheng, Q. & Kim, J.-K.) 1-27 (Springer New York, New York, NY, 2015).

3. Ellmer, K. Past achievements and future challenges in the development of optically transparent electrodes. *Nat. Photonics* **6**, 809 (2012).

4. Lampert, C.M. Heat mirror coatings for energy conserving windows. *Sol. Energy Mater.* **6**, 1-41 (1981).

5. Lewis, B.G. & Paine, D.C. Applications and Processing of Transparent Conducting Oxides. *MRS Bull.* **25**, 22-27 (2000).

6. Greenham, N.C., Moratti, S.C., Bradley, D.D.C., Friend, R.H. & Holmes, A.B. Efficient light-emitting diodes based on polymers with high electron affinities. *Nature* **365**, 628 (1993).

7. Yu, Z. et al. Indium tin oxide as a semiconductor material in efficient p-type dye-sensitized solar cells. *NPG Asia Mater.* **8**, e305 (2016).

8. Guo, P., Schaller, R.D., Ketterson, J.B. & Chang, R.P.H. Ultrafast switching of tunable infrared plasmons in indium tin oxide nanorod arrays with large absolute amplitude. *Nat. Photonics* **10**, 267 (2016).

9. Naik, G.V., Shalaev, V.M. & Boltasseva, A. Alternative Plasmonic Materials: Beyond Gold and Silver. *Adv. Mater.* **25**, 3264-3294 (2013).

10. Alam, M.Z., De Leon, I. & Boyd, R.W. Large optical nonlinearity of indium tin oxide in its epsilon-near-zero region. *Science* **352**, 795 (2016).

11. Srinivasan, V., Pamula, V.K. & Fair, R.B. An integrated digital microfluidic lab-on-a-chip for clinical diagnostics on human physiological fluids. *Lab Chip* **4**, 310-315 (2004).

12. Kumar, A. & Zhou, C. The Race To Replace Tin-Doped Indium Oxide: Which Material Will Win? *ACS Nano* **4**, 11-14 (2010).

13. Shigesato, Y., Takaki, S. & Haranou, T. Crystallinity and electrical properties of tin-doped indium oxide films deposited by DC magnetron sputtering. *Appl. Surf. Sci.* **48-49**, 269-275 (1991).

14. Tahar, R.B.H., Ban, T., Ohya, Y. & Takahashi, Y. Tin doped indium oxide thin films: Electrical properties. *J. Appl. Phys.* **83**, 2631-2645 (1998).

15. Wen, L., Sahu, B.B. & Han, J.G. Development and utility of a new 3-D magnetron source for high rate deposition of highly conductive ITO thin films near room temperature. *Phys. Chem. Chem. Phys.* **20**, 4818-4830 (2018).

16. Cairns, D.R. et al. Strain-dependent electrical resistance of tin-doped indium oxide on polymer substrates. *Appl. Phys. Lett.* **76**, 1425-1427 (2000).

17. Charalampos, A., Kaihao, Z., Matthew, R. & Sameh, T. Tailoring the mechanical properties of 2D materials and heterostructures. *2D Mater.* **5**, 032005 (2018).

18. Daeneke, T. et al. Wafer-Scale Synthesis of Semiconducting SnO Monolayers from Interfacial Oxide Layers of Metallic Liquid Tin. *ACS Nano* **11**, 10974-10983 (2017).

19. Carey, B.J. et al. Wafer-scale two-dimensional semiconductors from printed oxide skin of liquid metals. *Nat. Commun.* **8**, 14482 (2017).

20. Syed, N. et al. Wafer-Sized Ultrathin Gallium and Indium Nitride Nanosheets through the Ammonolysis of Liquid Metal Derived Oxides. *J. Am. Chem. Soc.* (2018).

21. Syed, N. et al. Printing two-dimensional gallium phosphate out of liquid metal. *Nat. Commun.* **9**, 3618 (2018).

22. Zavabeti, A. et al. A liquid metal reaction environment for the room-temperature synthesis of atomically thin metal oxides. *Science* **358**, 332-335 (2017).

23. Daeneke, T. et al. Liquid metals: fundamentals and applications in chemistry. *Chem. Soc. Rev.* **47**, 4073-4111 (2018).

24. Preuß, A., Adolphi, B. & Wegener, T. The kinetic of the oxidation of InSn48. *Fresenius' J. Anal. Chem.* **353**, 399-402 (1995).

25. Nadaud, N., Lequeux, N., Nanot, M., Jové, J. & Roisnel, T. Structural Studies of Tin-Doped Indium Oxide (ITO) and $In_4Sn_3O_{12}$. *J. Solid State Chem.* **135**, 140-148 (1998).

26. Thøgersen, A., Rein, M., Monakhov, E., Mayandi, J. & Diplas, S. Elemental distribution and oxygen deficiency of magnetron sputtered indium tin oxide films. *Journal of Applied Physics* **109**, 113532 (2011).

27. Bae, S. et al. Roll-to-roll production of 30-inch graphene films for transparent electrodes. *Nat. Nanotechnol.* **5**, 574 (2010).Dixon, S. C., Scanlon, D. O., Carmalt, C. J. & Parkin, I. P. n-Type doped transparent conducting binary oxides: an overview. *J. Mater. Chem. C* **4**, 6946-6961, doi:10.1039/C6TC01881E (2016).

Chapter 6

Conclusions and Future Work

6.1. Conclusions

The primary objectives of this PhD research, as outlined at the beginning of this thesis, were to explore the synthesis of atomically thin 2D metal oxides of layered and non-layered crystals and their applications in catalysis and electronics. The contents of this thesis have contributed to the knowledge regarding investigation of electrocatalytic properties of reduced 2D molybdenum oxides in hydrogen evolution reactions (HER) for hydrogen production. A subsequent work features the novel synthetic route to produce non-layered 2D metal molybdates such as 2D PbMoO4 and investigate its photocatalytic properties under visible light irradiation. The final work also explores the large area synthesis of non-layered transparent conductive oxides (TCOs) such ITO in 2D form, where the liquid metal precursor was utilized to facilitate the synthesis process. Detailed discussions regarding the outcomes of developed materials and their applications are presented in three separate stages as follows:

6.1.1. Stage 1

The presented research work demonstrates a facile and stable method to synthesise reduced 2D α-MoO$_{3-x}$ from layered bulk α-MoO$_3$. The as synthesized 2D nanosheets contain ~6 fundamental layers of orthorhombic molybdenum oxides on average with an average lateral

dimensions of ~125 nm. The XPS studies revealed the presence of oxygen vacancies in the 2D α-MoO$_{3-x}$ nanosheets. Crystalline and vibrational analyses demonstrated the highly ordered planar structure of the synthesized 2D nanosheets.

Furthermore, both the 2D and bulk materials were incorporated in electrocatalytic HER in order to understand and compare their performances as electrocatalysts. The reduced 2D nanosheets were found to exhibit superior performance not only compared to its bulk counterparts but also compared to the previously reported works based on molybdenum oxides, their compounds and heterostructures as well as selected reports on 2D molybdenum sulphides.

In alkaline media, the 2D α-MoO$_{3-x}$ nanosheets were found to require only 142 mV overpotential to achieve the standard 10 mAcm^{-2} current density, while the bulk materials showed a much higher required overpotential. The influential factors in achieving high HER activity were found to be the combination of oxygen deficient structure and large surface area of the 2D nanosheets with structural defects and steps. These properties significantly intensified the density of catalytic sites for highly active HER performance. The future prospects of the developed work will be discussed in the later section.

6.1.2. Stage 2

A subsequent work of the previous project leads to the novel synthetic route to produce 2D nanosheets of a non-layered crystal using the 2D molybdenum oxides. Due to the non-stratified crystal structures that metal molybdates contains, these materials lack the natural inclination to form 2D morphologies using conventional techniques. In this work, a novel approach for synthesizing 2D metal molybdates such as PbMoO$_4$ nanosheets was established. A two-step method was applied to synthesize 2D PbMoO$_4$ from 2D α-MoO$_{3-x}$ nanosheets.

The structural transformation of the synthesized 2D α-MoO$_{3-x}$ nanosheets were achieved by infusing Pb^{2+} ions in an aqueous solution that contains the 2D α-MoO$_{3-x}$ suspensions. Morphological and structural characterizations confirmed that the transformed 2D nanosheets are scheelite type PbMoO$_4$ crystals that adopted the 2D morphologies of 2D α-MoO$_{3-x}$.

The electronic band structure of both the materials were determined using the information obtained through Tauc plots, XPS valence bands and PESA measurements. The 2D PbMoO$_4$ nanosheets showed a wide bandgap value of 3.4 eV and featured a conduction band edge position suitable for the oxidation of dye components. Interestingly, the presence of trap states within the bandgap made the material available for solar light absorption *via* reducing the effective bandgap of the material. Later the synthesized 2D nanosheets were investigated for photocatalytic degradation of an organic dye, where this 2D material exhibited superior performance compared to the previously reported nano morphologies of lead molybdates and tungstates. The key factors behind the exciting performance are the high surface area of the 2D nanosheets and the presence of trap states. This suggests the high potential of the synthesized 2D metal molybdate nanosheets in various photocatalytic applications.

In summary, the presented work provides a novel synthetic route to synthesize 2D nanosheets of a non-stratified metal molybdate. ICP-MS measurements were also utilized to ensure the environmental safety of this synthesis material for water remediation applications. Thus, it is believed that the demonstrated approach could be suitable for synthesizing a range of metal molybdates into 2D form which may feature exciting catalytic performance.

6.1.3. Stage 3

The final part of this thesis deals with the 2D synthesis of non-layered TCOs such as ITO. This work demonstrates a novel printing process to deposit ultrathin 2D ITO sheets onto

range of substrates such as glass, quartz and polymers. The low melting liquid alloys undergo Cabrera-Mott oxidation that creates self-limiting 2D surface oxides on top of a liquid alloy droplet. This 2D skin can be transferred onto solid substrates *via* exploiting van der Waals adhesion.

In this work, various compositions of indium tin alloys were exploited to obtain the desired 2D ITO nanosheet that exhibits the high conductivity. The optimum alloy concentration delivered 7.36 at% of Sn^{4+} in the synthesized 2D ITO nanosheets. Centimetre sized 2D nanosheets were obtained by using the developed process, which creates the possibilities for continuous printing processes that allows low temperature printing of large area 2D ITO.

The synthesized 2D ITO displayed high transparency across the visible spectrum, while being electrically conductive. The ultrathin feature of the 2D ITO (~1.1 nm thick) leads to highly flexible nature which displayed a minimal conductivity loss after 1000 cycles of bending to a radius of 2 mm. This offers a solution to design ITO based flexible electronics, which is currently hindered by the brittle nature of the thicker commercial ITO. The developed process also provides an alternative to the currently practiced vacuum technology and presented its suitability for the fabrication of fully functional capacitive touch screens.

6.2. Future outlook

The research presented in this thesis has contributed significant to progress in the field, evidenced by the publication of several peer-reviewed journal articles. As research interest in the field of 2D materials based on layered and non-layered metal oxides continues to grow, this thesis provides a basis for several new branches of future investigations.

6.2.1. *Prospects of 2D layered metal oxides in electrocatalytic HER*

The initial study exploring the electrocatalytic properties of 2D MoO_{3-x} in HER highlights the importance of substoichiometric molybdenum oxides in this field. In the future, fine tuning of the stoichiometry may lead to improved catalytic efficiency and more promising results. This finding also signifies the potential of other 2D layered metal oxide compounds to be investigated in HER with optimum tuning of their stoichiometries providing an important approach towards maximizing the catalytic activity. The presence of oxygen vacancies in layered metal oxides reduces the charge transfer resistance when employed in an electrocatalytic HER system and accelerates the reaction kinetics.

A further exciting scope constitutes incorporating these reduced 2D layered metal oxides in heterostructures, possibly enabling more stable HER electrocatalysts due to the capability to use separate materials with one being responsible for enabling high catalytic activity, with a second material providing structural integrity. Heterostructures may also be utilized to obtain even lower overpotentials, taking advantage of synergistic effects that occur when creating electronic heterostructures and Janus sheets. Ultimately this may lead to an economically sustainable HER system, with catalytic activity that approaches that of noble metal catalysts while utilizing comparatively abundant materials for future hydrogen generation.

6.2.2. *Possibilities of creating 2D nanosheets of non-layered metal molybdates*

Metal molybdates are renowned for their superior activities in catalysis. In addition, these materials have been vastly used as anode or cathode materials in aqueous capacitors exploiting various morphologies and heterostructures. The presented method to obtain 2D nanosheets of these non-layered crystals opens the door for their usage in a broad range of

such applications. Due to their nanometre thickness with high surface area, nearly all of the metal atoms can interact with electrolytes and potentially take part in redox reactions, likely enabling to acheive pseudocapacitances that approach the theoretical values. A range of metal molybdates and tungstates can likely be synthesized into 2D form using the developed synthesis protocol. The synthesis of these materials should be explored and their properties should be investigated, with the specific target applications in energy storage as well as catalysis. This may lead to their incorporation in many exciting electrochemical and photocatalytic applications.

6.2.3. 2D ITO in future electronic and optoelectronic devices

The high transparency of 2D ITO outperforms graphene by two orders of magnitude, making 2D ITO a promising alternative when high transparency is favored over a low sheet resistance. An example of such applications is capacitive touch screens for handheld devices, where the high transparency can effectively reduce the device's energy consumption and enhance display quality. Furthermore, the sheet resistance of the ultrathin 2D ITO can likely be reduced by deploying networks of metal nanowires together with 2D ITO, leading to transparent conductive coatings which maintain pinhole free conductivity with high transparency while reducing the sheet resistance even further. Such composites may find application in optoelectronic devices such as light emitting diodes and solar cells, where a low sheet resistance as well as pinhole free conductance is crucial. Other prospective applications of 2D ITO involve the creation of van der Waals heterostructures where it may substitute graphene as a conductor with higher transparency and printability that are highly sought after for future electronics.

6.3. List of publications

1. **Highly active two dimensional α-MoO$_{3-x}$ for the electrocatalytic hydrogen evolution reaction**

   R. S. Datta, F. Haque, M. Mohiuddin, B. J. Carey, N. Syed, A. Zavabeti, B. Zhang, H. Khan, K. J. Berean, J. Z. Ou, N. Mahmood, T. Daeneke, K. Kalantar-zadeh

   J. Mater. Chem. A, 2017, volume 5, issue 46, pp. 24223-24231, DOI: 10.1039/C7TA07705J.

2. **Two dimensional PbMoO$_4$: A photocatalytic material derived from a naturally non-layered crystal**

   R. S. Datta, J. Z. Ou, M. Mohiuddin, B. J. Carey, B. Y. Zhang, H. Khan, N. Syed, A. Zavabeti, F. Haque, T. Daeneke, K. Kalantar-zadeh

   Nano Energy, 2018, Volume 49, Pages 237-246, DOI: https://doi.org/10.1016/j.nanoen.2018.04.041.

3. **Liquid metal derived ultrathin, highly flexible and large area printable two-dimensional ITO**

   R. S. Datta, N. Syed, A. Zavabeti, A. Jannat, M. Mohiuddin, M. Rokunuzzaman, B. Y. Zhang, M. A. Rahman, P. Atkin, K. A. Messalea, M. B. Ghasemian, D. Esrafilzadeh, K. Kalantar-zadeh, T. Daeneke

   Under review at Nat. Electron.

4. **Molybdenum Oxides – From Fundamentals to Functionality**

   I.A. de Castro, **R. S. Datta**, J.Z. Ou, A. Castellanos-Gomez, S. Sriram, T. Daeneke, K. Kalantar-zadeh

   Adv. Mater., 2017, volume 29, issue 40, pp.1701619, DOI: 10.1002/adma.201701619.

5. **Ordered intracrystalline pores in planar molybdenum oxide for enhanced alkaline hydrogen evolution**

F. Haque, A. Zavabeti, B. Y. Zhang, **R. S. Datta**, Y. Yin, Z. Yi, Y. Wang, N. Mahmood, N. Pillai, N. Syed, A. Jannat, H. Khan, N. Wang, N. Medhekar, K. Kalantar-zadeh, J. Z. Ou

J. Mater. Chem. A, 2019, volume 7, issue 1, pp. 257-268, DOI: 10.1039/C8TA08330D.

6. **Sonication-Assisted Synthesis of Gallium Oxide Suspensions Featuring Trap State Absorption: Test of Photochemistry**

N. Syed, A. Zavabeti, M. Mohiuddin, B. Zhang, Y. Wang, **R. S. Datta**, P. Atkin, B. J. Carey, C. Tan, J. van Embden, A. S. R. Chesman, J. Z. Ou, T. Daeneke and K. Kalantar-zadeh

Adv. Funct. Mater., 2017, volume 27, issue 43, pp. 1702295, DOI: https://doi.org/10.1002/adfm.201702295.

7. **Degenerately Hydrogen Doped Molybdenum Oxide Nanodisks for Ultrasensitive Plasmonic Biosensing**

B.Y. Zhang, A. Zavabeti, A.F. Chrimes, F. Haque, L.A. O'Dell, H. Khan, N. Syed, **R. S. Datta**, Y. Wang, A.S.R. Chesman, T. Daeneke, K. Kalantar-zadeh, J. Z. Ou

Adv. Funct. Mater., 2018, volume 28, issue 11, pp. 1706006, DOI: https://doi.org/10.1002/adfm.201706006.

8. **Liquid Phase Acoustic Wave Exfoliation of Layered MoS2: Critical Impact of Electric Field in Efficiency**

M. Mohiuddin, Y. Wang, A. Zavabeti, N. Syed, **R. S. Datta**, H. Ahmed, T. Daeneke, S. P. Russo, A. R. Rezk, L. Y Yeo, K. Kalantar-zadeh

Chem. Mater., 2018, 30 (16), pp. 5593-5601, DOI: 10.1021/acs.chemmater.8b01506

9. **Printing two-dimensional gallium phosphate out of liquid metal**

   N. Syed, A. Zavabeti, J. Z. Ou, M. Mohiuddin, N. Pillai, B. J. Carey, B. Y. Zhang, **R. S. Datta**, A. Jannat, F. Haque, K. A. Messalea, C. Xu, S. P. Russo, C. F. McConville, T. Daeneke & K. Kalantar-zadeh

   Nat. Commun., 2018, volume 9, no. 1, pp. 1-10. DOI: 10.1038/s41467-018-06124-1.

10. **Green Synthesis of Low-Dimensional Aluminum Oxide Hydroxide and Oxide Using Liquid Metal Reaction Media: Ultrahigh Flux Membranes**

    A. Zavabeti, B. Y. Zhang, I. A. de Castro, J. Z. Ou, B. J. Carey, M. Mohiuddin, **R. S. Datta**, C. Xu, A. P. Mouritz, C. F. McConville, A. P. O'Mullane, T. Daeneke, K. Kalantar-Zadeh

    Adv. Funct. Mater., 2018, volume 28, issue 44, p. 1804057. DOI: https://doi.org/10.1002/adfm.201804057.

11. **Exfoliation Behavior of van der Waals Strings: Case Study of Bi$_2$S$_3$**

    N. Dhar, N. Syed, M. Mohiuddin, A. Jannat, A. Zavabeti, B. Y. Zhang, **R. S. Datta**, P. Atkin, N. Mahmood, D. Esrafilzadeh, T. Daeneke, and K. Kalantar-zadeh

    ACS Appl. Mater. Interfaces., 2018, DOI: 10.1021/acsami.8b14702.

12. **Exploring electric field assisted van der Waals weakening of stratified crystals**

    M. Mohiuddin, N. Pillai, A. Zavabeti, N. Mahmood, N. Syed, **R. S. Datta**, D. Jampaiah, T. Daeneke, J. Z. Ou, K. Kalantar-zadeh

Appl. Mater. Today., 2018, Volume 12, pp. 359-365. DOI: https://doi.org/10.1016/j.apmt.2018.05.005.

13. **An Ultrasensitive Silicon Photonic Ion Sensor Enabled by 2D Plasmonic Molybdenum Oxide**

   G. Ren, B. Y. Zhang, Q. Yao, A. Zavabeti, C. S Huertas, R. Brkljača, M. W. Khan, H. Nili, **R. S. Datta**, H. Khan, A. Jannat, S. Walia, F. Haque, L. A. O'Dell, Y. Wang, L. Zhu, A. Mitchell, J. Z. Ou

   Small, 2019, p1805251. DOI: https://doi.org/10.1002/smll.201805251.